Self-modulation of photoemitted bunches at the picosecond timescale

Dissertation
to obtain the degree of
"Doctor of Natural Sciences"
submitted to the
Department of Physics, Mathematics and Computer Science
of Johannes Gutenberg-Universität of Mainz

M.Sc. Nahid Scahill
Born in Tehran

Mainz, 18 November 2021

Date of defense: 18.02.2022

To my dear family,
Michael, Michael Reza, Daniel Azuir, Andrew Amir, Joshua Emad,
and
in loving memory of my dear mother, Behjat Hejazi

Abstract

Photoemission sources are essential for operation of high-power accelerators. The successful operation of such electron accelerators demands the appropriate choice of photocathode material that can produce low emittance electron beams with high brilliance and high quantum efficiency. The time response of the cathode is also an important factor for the accelerator applications, and the pulse response must be within the longitudinal acceptance of the accelerator. Any part of the electron bunch not contained in the longitudinal acceptance of the accelerator contributes to a longitudinal halo which must be strictly minimized. The losses associated with longitudinal halo result in induced accelerator component radioactivity and can create background which masks the physics processes in the detectors. In the case of the MESA accelerator, the maximum accepted pulse length is 200 ps. Therefore, photocathodes capable of producing fast responses are desirable.

In addition, many accelerator systems require spin-polarized beams. In MESA, beams of high spin-polarization are required for the precision measurements of the electroweak mixing angle (P2). Generating the spin-polarized electron beam can be achieved with GaAs-based photocathodes in negative electron affinity state. The strained superlattices, in particular, increase the strain-induced splitting which makes them superior sources of polarized electrons.

The present work is composed of two parts. First, investigating pulse responses of the bulk GaAs as the quantum efficiency decays. The dependency of the pulse shape on quantum efficiency over many orders of magnitude was observed. The results showed that as the quantum efficiency dropped, the general trend was such that the intensity of the halo decreased. At very low quantum efficiency ($< 10^{-4}$ %), when high-intensity illumination was needed, a surface photovoltage developed and limited the extracted current due to space charge. The surface photovoltage effect at the picosecond timescale was investigated in photoemission for the first time. This characteristic can be approximated to a continuous pump-probe in which self-modulation of the electron pulses at picosecond timescale is reached.

Second, the time response and polarization of the strained GaAs/GaAsP superlattice was investigated in a time-resolved manner. In order to conduct the polarization measurements, a Wien filter spin-rotator was built and commissioned. The investigation delivered a pulse with a longitudinal halo in the order of 3×10^{-4} of the peak intensity. The results indicated that GaAs/GaAsP, when compared to other superlattices, can be considered a better choice of cathode for investigations in accelerator systems, in particular, for experiments with spin-polarized electron beams such as the P2 experiment in MESA.

Contents

1 Motivation and introduction

I want to know how God created this world. I am not interested in this or that phenomenon, I want to know God's thoughts, the rest are mere details.

— *Albert Einstein*

For decades, electron beams have been valuable tools for discovery science in atomic, molecular, nuclear, and particle physics. In particular, electron beams are an absolute necessity for all cutting-edge applications of electron accelerators. One such example is the use of electron scattering to investigate the structure of nucleons and atomic nuclei.

Electrons are elementary particles of the Standard Model. Through electromagnetic interaction with nuclei, electron beams can extract information about the internal structure of the target with high precision. Furthermore, electron, in addition to the typical intrinsic properties of charge and mass, carries spin. The fascinating fact that electron spin, bound by nature, is quantized in two distinct values that cannot occur simultaneously makes electrons an important tool in a variety of fields of research. Spin has played a very significant role in nuclear and high-energy physics, shedding a new light on understanding matter and fundamental interactions. In particular, beams of polarized electrons have been used to perform parity-violating experiments and measurements of nucleon spin structure.

Future high-power accelerators such as EIC[1], LHeC[2], and MESA[3] are novel tools which use electron scattering to discover physics beyond the Standard Model and unlock the secrets of the matter in the universe. The high-energy EIC will explore one of the four currently known fundamental forces of nature, the strong nuclear force. The EIC will use polarized beams of electrons and ions to explore the inner structure of the nucleus and obtain insight into the proton spin. LHeC will be devoted to high-precision deep inelastic electron-proton and electron-ion scattering measurements to study the substructure of the proton and the nuclei. MESA, which is currently under construction at the Institute for Nuclear Physics in Mainz [55], will use electron scattering for experiments such as the parity-violating P2 experiment [19] and search for dark matter through the Mainz gas Internal target eXperiment (MAGIX) [36].

[1]Electron-Ion Collider, Brookhaven National Lab, USA
[2]Large Hadron electron Collider, CERN, Switzerland
[3]Mainz Energy-recovering Superconducting Accelerator, Germany

1.1 Motivation

Development of the mentioned discovery investigations demand electron beams with high luminosities. Luminosity is a physical quantity characterizing the performance of a particle accelerator, defined as the ratio of the number of interactions (N) in a certain time to the cross section of the interaction (σ) [52]:

$$\mathcal{L} = \frac{1}{\sigma}\frac{\mathrm{d}N}{\mathrm{d}t} \tag{1.1}$$

Luminosity describes the ability of an accelerator to produce the required number of interactions. For a fixed target, the luminosity can be written as

$$\mathcal{L} = \Phi \rho \, l \tag{1.2}$$

where Φ denotes the flux of the electron beam, and ρ and l are the density and the length of the target, respectively.

The projected luminosity values for the P2 and MAGIX experiments in MESA are approximately $10^{39}\,\mathrm{cm}^{-2}\,\mathrm{s}^{-1}$ [19] and $10^{35}\,\mathrm{cm}^{-2}\,\mathrm{s}^{-1}$ [106] , respectively. Achieving such high luminosities requires an appropriate choice of photocathode material. The P2 experiment demands a highly spin-polarized electron beam, while MAGIX requires an unpolarized beam of high current up to 10 mA.

In addition, the time response of the cathode is an important factor for accelerator applications. The pulse response of the cathode must be within the longitudinal acceptance of the accelerator, which is typically a few picoseconds long. Any part of the electron bunch not contained in the longitudinal acceptance of the accelerator contributes to a longitudinal halo, referred to as an unwanted beam. Longitudinal halo is a significant limiting factor in the performance of accelerators. The longitudinal halo leads to degradation of the cathode lifetime. More importantly, electrons confined in the longitudinal halo can collide with the vacuum tube and cause damage to the machine and to the surroundings, by activation of the accelerator components. Furthermore, longitudinal halo can cause detector background in the physics experiments to which the beam is delivered. Minimizing longitudinal halo is particularly important in high-energy, high-intensity linear accelerators, since the halo generated in the injector section propagates downstream and can present tremendous harm.

In the case of MESA accelerator, the maximum accepted pulse length is FWHM = 200 ps. Photoelectrons which are emitted from the crystal after 200 ps are wasted and contribute to longitudinal halo. Therefore, photocathodes capable of producing fast responses are desirable.

For high-current experiments like MAGIX, semiconductor photocathodes are preferred to metallic cathodes since they have better optical absorption, resulting in significantly higher quantum efficiency values. The GaAs photocathodes possess a large bandgap, allowing creating a large negative electron affinity level[4] which

[4] A negative electron affinity state is obtained when the vacuum level lies below the conduction band minimum. A more detailed description follows in Chapter 2.

makes them highly effective photoemitters. Electron beams with currents above 10 mA can be produced with GaAs photocathodes if the quantum efficiency in the infrared regime remains above 1 % [42].

However, when quantum efficiency is low so that high-intensity illumination is needed, a surface photovoltage[5] develops and limits the current due to space charge, see Section 5.7.1. In the context of this work, the surface photovoltage effect at the picosecond timescale was investigated in photoemission for the first time[6]. This characteristic exhibits achieving self-modulation of the electron pulse at the picosecond scale, an effect which may have technical applications.

The surface photovoltage effect is a disadvantage of the GaAs photocathodes. Unless this effect is mitigated, other types of cathodes such as multi-alkali compounds are preferred for high-current applications.

In an investigation with InAlGaAs/GaAs superlattice, longitudinal halo in the order of 10^{-2} compared to the peak intensity was observed [45]. The unique heterostructure of strained superlattices, such as GaAs/GaAsP, allow fast emission of the photoelectrons with minimal tail. For this reason, in this study, the strained GaAs/GaAsP superlattice was investigated at an excitation wavelength of 800 nm, and for the first time, its pulse response in the tail region was measured with high resolution.

Furthermore, the orderly band structure of GaAs-based cathodes makes them an excellent source of spin-polarized beams. Introducing an axial strain, breaks the symmetry of the GaAs crystalline structure and induces valence band splitting, which results in higher polarization. More specifically, in strained GaAs/GaAsP superlattice, the periodic active layer structure naturally increases the splitting of the valence band, and thereby increases the strain-induced splitting. These distinct features make the strained GaAs/GaAsP superlattice a superior source of polarized electrons, allowing significantly higher polarization, above 85 %, compared to other cathodes [73].

1.2 MESA

An overview of the MESA accelerator and its major components is illustrated in Fig. 1.1. After the electron beam is generated, the beam is guided into the MESA Low-energy Beam Apparatus (MELBA). MELBA serves as a diagnostic and manipulating station to examine the properties of the beam and prepare the beam before it enters the 5 MeV injector station MAMBO, the Milli Ampere Booster.

MELBA consists of two Wien filters and a solenoid to rotate the spin of the electrons prior to the P2 experiment. In addition, the apparatus has a chopper/buncher system to adjust the longitudinal phase space of the electron bunch. The operat-

[5] Surface photovoltage refers to the state when excess electrons are accumulated at the surface resulting in the reduction of the escape probability and suppressing the tail of the pulse response. See the discussion in Chapter 5.

[6] To the best of our knowledge.

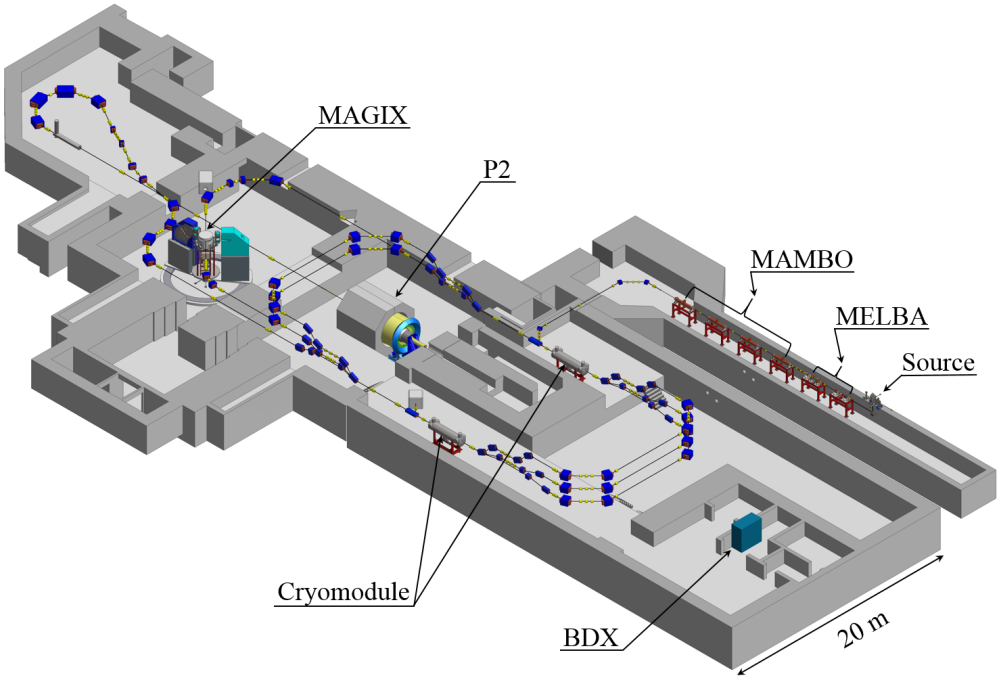

Figure 1.1: Overview of the MESA accelerator.

ing frequency of MESA is 1.3 GHz, which is equivalent to a period of 770 ps. The chopper/buncher system will chop the unwanted beam halo and further compress the bunch so that the electron bunch will fit the longitudinal acceptance of the accelerator [24, 109].

After MAMBO, electrons are guided into the main accelerator section and, according to the specific experiment, a mode of operation will be selected, and the electrons energy is adjusted. MESA will operate in two modes:

External beam mode (EB): In this mode, a longitudinally spin-polarized beam with a current of 150 µA and an energy of 155 MeV is generated and directed to the parity-violating electron scattering experiment, P2 [19]. Another experiment in the EB mode is the Beam Dump eXperiment (BDX). In BDX, the high-energy electron beam is stopped in the beam dump, and through the interaction of the electrons with a heavy nucleus, the dark photon can be produced and investigated [77].

Energy-recovery mode (ER): In this mode, MESA provides unpolarized beams of 105 MeV energy and currents of 1 mA, with a further increase to 10 mA being envisioned in a second stage. In this mode, electrons are returned to the accelerator with a phase shift of 180°, and thus most of their kinetic energy is transferred to the accelerating structure. MESA will use the ER mode for MAGIX in search of the dark photon.

The main operating parameters for each of the two modes are summarized in Table 1.1. The design parameters for the second stage of the ER-mode are shown in parentheses.

Table 1.1: The main operating parameters of the MESA for each mode.

Parameter	**External Beam (EB)**	**Energy-Recovery (ER)**
Energy	155 MeV	105 MeV
Average current	150 µA	1 mA (10 mA)
Spin polarization	$> 85\,\%$	No
Experiment	P2	MAGIX
Target	Liquid hydrogen	Gaseous hydrogen
Investigation	Weinberg angle	Multi purpose

1.2.1 The P2 experiment

The purpose of the P2 experiment is a precise determination of the electroweak mixing angle $\sin^2(\theta_{\mathrm{W}})$, known as the *Weinberg angle*, and a precision test of the Standard Model and its predictions. The proton weak charge, $Q_{\mathrm{W}}(\mathrm{p})$, is related to the Weinberg angle and is sensitive to small deviations of the Weinberg angle from its predicted value.

$$Q_{\mathrm{W}}(\mathrm{p}) = 1 - 4\sin^2(\theta_{\mathrm{W}}) \tag{1.3}$$

Since the Standard Model does not assign a specific numerical value to the electroweak mixing angle, its value can be obtained only through experimental results. The Large Electron Positron Collider, LEP [30] and Stanford Linear Accelerator Center, SLAC [1], have attempted to determine the value of the Weinberg angle. The measurements were conducted with high energy and momentum transfers in the electron-positron scattering and yielded values which differ from each other by more than three standard deviations. On the other hand, the low-momentum-transfer determination of $\sin^2(\theta_{\mathrm{W}})$ delivered values with large uncertainties due to the extremely small asymmetries.

While high-energy particle accelerators for example Conseil Européen pour la Recherche Nucléaire (CERN), have been searching for new particles [32, 33], the predicted deviations in the extensions of the Standard Model can be verified only through precision experiments. The value of the electroweak mixing angle is sensitive to the momentum transfer during the experiment. Therefore, a high-precision low-momentum-transfer experiment, such as P2, is expected to offer a determination of the electroweak mixing angle with high accuracy and precision. The results of the P2 experiment in MESA could be a decisive factor in either verifying the prediction of the Standard Model and resolving the differences between the previous measurements or leading to interesting New Physics.

In the P2 experiment, a polarized electron beam impinges on an unpolarized liquid hydrogen target. The polarization of the electron beam is changed by switching the helicity of the circularly polarized light with a frequency of 1 kHz (see Chapter 4).

The weak charge of the proton can be determined through a precision measurement of the parity-violating asymmetry in the elastic collision of the electrons and protons. Allowing $\mathrm{d}\sigma^{\pm}$ to be the differential cross sections for the elastic scattering of electrons with positive and negative helicity of protons, the asymmetry can be written as

$$A_{\mathrm{PV}} = \frac{\mathrm{d}\sigma^{+} - \mathrm{d}\sigma^{-}}{\mathrm{d}\sigma^{+} + \mathrm{d}\sigma^{-}} = \frac{-G_{\mathrm{F}}Q^2}{4\sqrt{2}\pi\alpha}[Q_{\mathrm{W}}(\mathrm{p}) - F(Q^2)] \tag{1.4}$$

where G_{F} denotes the Fermi coupling, Q^2 represents the momentum transfer, α is the electromagnetic coupling, and $F(Q^2)$ describes the form factor contribution [19]. The parity-violating asymmetry of the scattered electrons, resulting from the interference between the exchange of a photon and a Z-boson, can be calculated.

The source is expected to produce electron beams with polarization of approximately 90 % with an absolute accuracy of smaller than $\Delta P/P = 0.01$ [19]. Since extremely small asymmetries in the order of 10^{-8} are expected through the measurement [19], choosing a photocathode capable of delivering the highest polarization and minimizing any source of instrumental asymmetries resulting from the electron beam or the measurement setup of the P2 experiment is of utmost importance.

The P2 experiment is the most demanding investigation requiring 11 000 h of data taking.

1.2.2 The MAGIX experiment

The MAGIX experiment is designed for high precision electron-scattering experiments such as search for invisible decays of the dark photon and precise determination of the proton charge radius. In order to increase the needed level of precision for the measurement, electrons are scattered in a windowless thin gas-jet target. Therefore, the effects from energy loss and multiple scattering are substantially reduced compared to common fixed targets. By changing the gas flow, the target density can be adjusted. Although the density of the gas target is lower than that of a solid target, the required high luminosity for the MAGIX experiment can be obtained by using a high-intensity electron beam with a current of up to 10 mA, as it is envisioned for the second stage. These precision experiments are achieved with two high-resolution magnetic spectrometers and detectors. The spectrometers rotate around the target and are equipped to track, detect, and identify the produced particles [106].

1.3 Structure of the work

The goal of this project was to investigate the time responses of GaAs-based photocathodes with a special focus on intensity-dependent self-modulation at the picosecond timescale for the experiments at MESA. The structure of this dissertation is as follows: Chapter 2 presents the fundamental characteristics of good photoemitters. Important properties of GaAs-based crystals in photoemission and generating polarized electrons by using strained superlattices are also described in this chapter. The experimental setup and description of the most relevant elements for the time response and polarization measurements are presented in Chapter 3. In Chapter 4, the measuring principles and the preparatory measurements are described. In Chapter 5, experimental results of the bulk GaAs with a special focus on the surface photovoltage effect at high-intensity illumination are discussed. Chapter 6 focuses on the results of the investigations of the pulse response and polarization of strained GaAs/GaAsP superlattice. Finally, in Chapter 7, the results are summarized and the conclusions and outlook of this project are given.

2 Physical theory

An electron beam is not commonly thought of as a usable item in everyday life, however its impact on our lives is insurmountable. Electron beams are used in a wide variety of scientific endeavours to include: electron accelerators, medical therapy, aerospace, defense, and nuclear physics. Development of such investigations is imperative in providing a deeper understanding of the relationship between the structure and property in a wide range of materials. Performing many of these scientific research experiments requires high-brightness electron sources.

The following chapter is dedicated to serve as an overview of the main physical concepts pertaining to this research. After a brief description of different types of electron emission, characteristic qualities of a good photoemitter for use in an electron accelerator are discussed. Next, the principles of photoemission from the GaAs photocathode are explained. The final section of this chapter is devoted to describing the mechanism of generating spin-polarized electron beams, focusing on the strained GaAs/GaAsP superlattice, as polarized electron beams are an essential component of the investigations in MESA.

2.1 Photoemission

The chief principle in emitting electrons from a cathode is the ability to overcome the potential barrier, referred to as *work function*. In a semiconductor, the work function corresponds to the minimum amount of energy needed to remove an electron and is defined as the difference between the Fermi level and the vacuum level. The work function will be further discussed in Section 2.3.

In the *photoemission* process electrons are generated through absorbing photons of energies above the work function. With the advancement of laser technology and photocathode design, extracting extremely bright electron beams with low energy spread is possible while controlling the electron bunch length and the charge distribution [15]. Photoemission-based sources have many applications in a variety of research such as polarized electron beam for accelerators [4, 11], electron cooling of hadron beams [20], and light sources based on energy recovery linacs (ERL) [48].

A variety of cathodes, such as GaAs, K_2CsSb, Cs_2Te, are commonly used in many accelerator systems; however, the GaAs-based photocathodes are the standard electron emitters in many facilities to produce electron beams [11, 85, 111]. In particular, GaAs cathodes are the most useful sources of polarized electrons. The principle of the photoemission process of GaAs photocathodes, which are used in this project, and generation of polarized electrons are explained in greater detail in Sections 2.5 and 2.6.

2.2 Photoemitters

Photoemitters can be divided into two main groups, semiconductors and metals, based on the band structures. In an ideal semiconductor, the valence bands and conduction bands are separated by the forbidden gap with an energy E_{gap}, while in metals the valence bands overlap with the conduction bands. This fundamental difference plays an important role in the photoemission process, affecting the photon absorption behavior, the energy loss mechanisms during the transport of the electrons to the surface, and overcoming the surface potential barrier.

Compared to metals, semiconductors have lower work function and are able to achieve significantly higher quantum efficiency. Therefore, for high-current accelerator applications, semiconductor photocathodes are preferred to the metal cathodes, see Section 2.3.1. Since the focus of this project is on semiconductors, metals are not further discussed.

2.2.1 Effective electron affinity of semiconductors

The effective electron affinity, χ_{eff}, is defined as the energy difference between the vacuum level, E_{V}, and the conduction band minimum. If the vacuum energy level at the surface lies below the minimum conduction band energy, the corresponding χ_{eff} is negative, and the semiconductor is referred to as *negative electron affinity* (NEA) photocathode. Typically, the state of negative electron affinity is achieved through application of Cs and O_2 (or NF_3) on the p-doped surface, see Section 2.5.3. GaAs : CsO, used in this project, is a prominent example of an NEA photocathode.

If the vacuum level is above the minimum conduction band, however, the χ_{eff} assumes positive values, and the semiconductor is considered a *positive electron affinity* (PEA) photocathode. K_2CsSb (potassium cesium-antimonide) is an example of a PEA photocathode. Fig. 2.1 demonstrates the schematic energy band diagram for p-doped NEA and PEA photocathodes.

In the photoemission process, the effective electron affinity is a critical factor. If χ_{eff} is low, photoexcited electrons require less energy to overcome the potential barrier at the surface which enhances the electron yield. In an NEA photocathode, the vacuum level is lower than the conduction band minimum; therefore, the photoexcited electrons effectively overcome the potential barrier and escape to the vacuum even if they have lost all of their kinetic energy during the transport. However, in a PEA cathode, only the electrons which have an energy above the vacuum level after transporting to the surface can be emitted into the vacuum.

The NEA photocathodes have the advantage of delivering spin polarized electron beams. The use of circularly polarized light of energies slightly above the bandgap allows for the generation of spin-polarized electrons in the photoemission from NEA photocathodes, see Section 2.6 for further discussion. Presently, no alternative to NEA-based photocathodes exists if spin-polarized beams are needed in the experiment. On the other hand, the PEA photocathodes offer lower electron

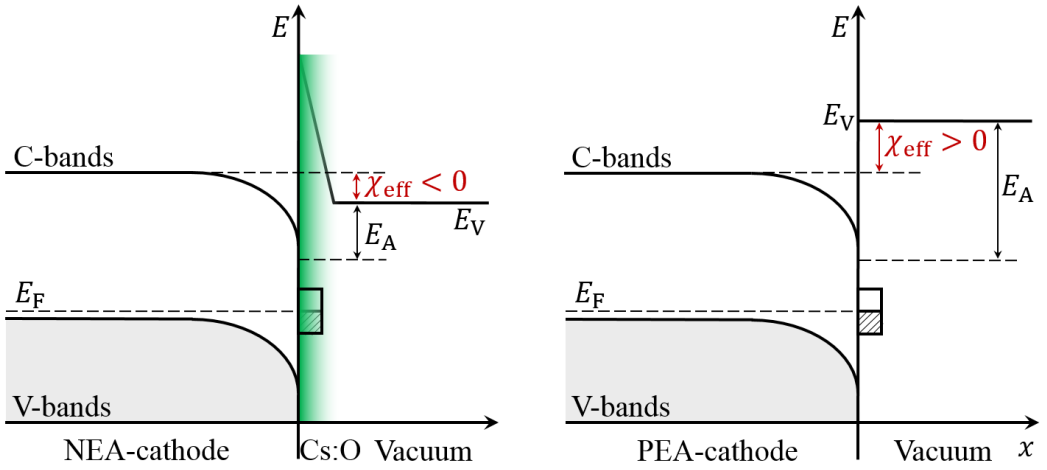

Figure 2.1: Schematic representation of energy band diagrams for a negative electron affinity cathode (on the left) and a positive electron affinity semiconductor (on the right). In the sketch, both types of cathodes are p-doped. E_{F}, E_{V}, and E_{A} represent Fermi level, vacuum energy, and electron affinity, respectively.

energy spread. Thus, for high-brightness applications, the PEA photocathodes are preferred to the NEA photocathodes.

2.3 Photocathode characteristics

In the experiments with the accelerator systems, the fundamental limiting factor in high-brightness electron beam sources is the photocathode itself. Once the electrons are emitted from the cathode, the intrinsic quality of the beam is fixed, allowing only for manipulation of the beam. Selecting the optimum type of photocathode in any area of research greatly depends on the applications and the requirements of the electron beam. In the following sections, several qualitative characteristics of photocathodes are discussed.

2.3.1 Quantum efficiency

Quantum efficiency, *QE*, determines the yield photocurrent and is defined as the number of emitted electrons, N_e, per number of the incident photons, N_γ. *QE* depends significantly on the photocathode material and the excitation wavelength of the laser. Fig. 2.2 shows *QE* variations as a function of the laser wavelength for most commonly used photocathode materials.

Figure 2.2 illustrates a prominent advantage of the GaAs photocathode, its ability to deliver high *QE* for a wide range of exciting wavelengths. Routinely, semiconductor photocathodes deliver higher *QE* values than metal cathodes due to the better

electron transport in semiconductors. *QE* can be determined experimentally by measuring the incident laser power P_L, the laser wavelength λ_L, and the emission current I, by using equation

$$QE = \frac{N_e}{N_\gamma} = \frac{hc}{e}\frac{I}{P_\mathrm{L}\lambda_\mathrm{L}} \tag{2.1}$$

where h is Planck's constant, c is the velocity of light, and e is the charge of the electron.

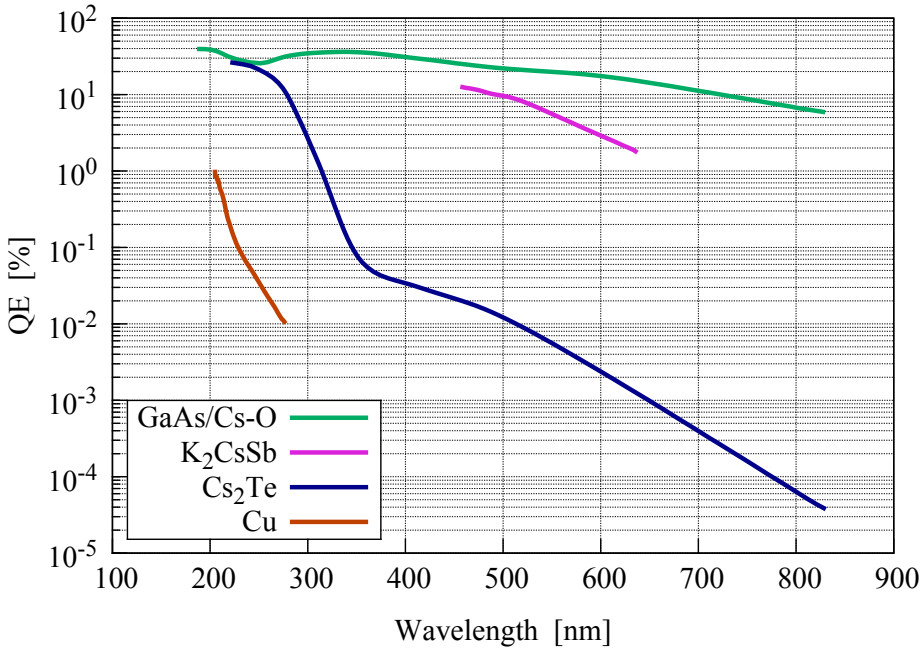

Figure 2.2: *QE* as a function of the excitation wavelength for different photocathode materials commonly used. Reproduced from [28].

QE is an important parameter representing the quality of the photocathode. *QE* investigations can reveal substantial information about different properties of the photocathode. Some examples include optical properties such as absorption length (see Section 2.3.3 for detailed explanation), transport properties like scattering mechanisms and relaxation time, and surface barrier properties such as electron affinity and band structure of the semiconductors [78]. In general, to avoid high-intensity laser drive, cathodes with *QE*s 1 % or higher are desirable [39]. In polarization measurements with polarized electrons, the measured *QE* directly impacts the quality factor, $QE \cdot P^2$, where P denotes the polarization.

It must be noted that the *QE* relationship as stated in Eq. (2.1), assumes that the photocurrent is proportional to the laser power; in other words, the emission is not limited by space charge. In Chapter 5, the effect of the space charge limit on the photocurrent is discussed. Regardless of the type of the research, a high value

of *QE* is desirable, and research has made paramount efforts in developing photocathode materials capable of delivering a high *QE*. As an example, researches have fabricated the strained superlattice (SSL) photocathodes with a thin active layer of less than 100 nm. The findings pertaining to GaAsP/GaAs strained superlattice cathodes studied in this work are presented in Chapter 6.

2.3.2 Lifetime

Yet another important factor in determining the quality of a photocathode is the *QE* lifetime. *QE* lifetime indicates the robustness of the cathode to withstand any considerable degradation in the system. The cathode lifetime is defined as the time required for the *QE* to drop to $1/e$ of its initial value. A cathode with a very high *QE* provides little benefit if the *QE* lifetime is short and ends before the experiment is complete. Therefore, to avoid operational interruptions in accelerator systems, a cathode with long operational lifetime is preferred to ensure stability of the beam without the need to revive or replace the cathode. The NEA photocathodes are very sensitive to residual gases and must be used only if there is no other alternative, e.g. when generating spin-polarization beam is required.

Photocathode lifetime can be divided into two components, namely the dark lifetime, measured when no charge is being extracted, and the operational lifetime, measuerd while the charge is being extracted. If τ_{d}, τ_{op}, and τ denote the dark, operational, and the overall lifetime respectively, and assuming a constant emission current of I during the operation, the *QE* evolution in time can be expressed as

$$QE(t) = QE_0\, e^{-\frac{t}{\tau}} \tag{2.2}$$

where

$$\frac{1}{\tau} = \frac{1}{\tau_{\mathrm{d}}} + \frac{1}{\tau_{\mathrm{op}}}. \tag{2.3}$$

One can extract τ directly from the decay of *QE* over time. The dark lifetime indicates the susceptibility of the cathode surface to chemical reactions with the residual gases in the vacuum and depends on the photocathode material and the vacuum conditions. On the other hand, the operational lifetime depends on several additional factors, mainly the presence of beam-generated ions, desorbed molecules, the laser power, and the cathode temperature. If all other processes, such as the beam loss in the vicinity of the source are suppressed sufficiently, the degradation of *QE* during beam operation can be predominantly due to ion back bombardment [65] and the desorbed gas. In ion back bombardment, residual gases in the chamber interact with the electron beam, become ionized, and are accelerated backwards toward the cathode. These ions can damage the structure of the crystal and can also sputter away the active layer used to generate the negative electron affinity surface, which in turn reduces the *QE*.

On the other hand, if the beam loss is present in the vicinity of the source, the desorbed gas from the walls will deteriorate the cathode even if no ionization of the residual gases exists. In reality, however, the effects are entangled; the desorbed

gases can also be ionized and contribute to the decay of photocathode lifetime. In operation at an accelerator with the radio frequency (RF)-synchronized beam, the losses near the source can become very small. Under such conditions, the deterioration of the photocathode is mainly due to the ionization of the residual gases. However, in an accelerator system where the beam dump is located in the laboratory, as is the case in our system, the contribution of the desorbed gases on the decay of *QE* is higher.

The effect of various contamination sources in the vacuum system such as CH_4, O_2, CO_2, CO, N_2 and H_2 on the *QE* of a GaAs photocathode under the base pressure of 1.5×10^{-11} mbar has been investigated in [27]. Fig. 2.3 represents the result of the quantum efficiency decay. The gas exposures are quoted in unit of Langmuir[1], L.

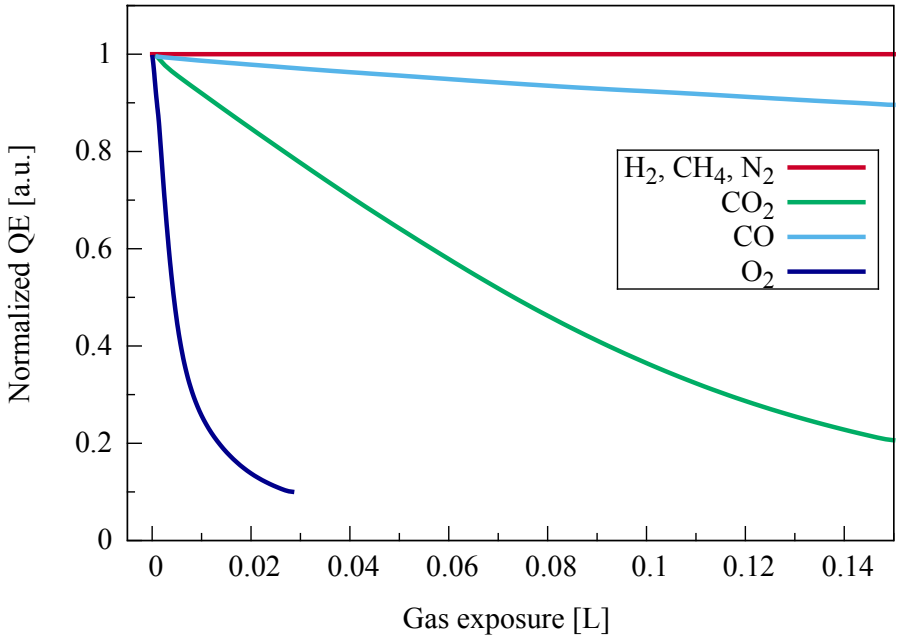

Figure 2.3: QE degradation for a typical bulk GaAs during different gas exposures. Reproduced from [27].

As seen in Fig. 2.3, the residual gases H_2, CH_4, and N_2 have no effect on the *QE* loss. While CO has a slight effect, CO_2 has a significant impact on decay of *QE*, and O_2 has the most severe effect, degrading the *QE* to 10 % of the initial value after an exposure of approximately 0.025 L. The lifetime can be increased by reducing the negative impact of the ion back-bombardment and the desorbed gas. In practice, this can be achieved by improving vacuum conditions, limiting the activated area of the photocathode [47], and minimizing the beam loss near the source.

[1] $1\,\mathrm{L} = 10^{-6}$ Torr s.

Another major process affecting the *QE* decay is the rise of the photocathode temperature due to laser illumination [140]. When the cathode is illuminated, a substantial portion of the laser power is converted to heat. The rise in temperature increases the thermal desorption of the active layer and enhances the *QE* degradation. In [56], the effect of the temperature on a GaAs photocathode under a vacuum pressure of 5.4×10^{-11} mbar has been studied. The findings indicated that an increase of 60 °C in temperature resulted in the *QE* loss escalating from 22 % to 92 % during the same time interval.

Although the *QE* of the GaAs photocathode can be recovered by reactivation, it is proven that the *QE* will never be restored to its initial value. It was shown that under the O_2 exposure, the *QE* can be recovered to 95 % of its initial value [27]. A much less restoration of only $60 - 70$ % of the *QE* initial value was reported for the GaAs cathode degraded under CO and CO_2 exposures. Eq. 2.2 indicates that *QE* eventually falls to a point where the cathode is not able to deliver the needed current. Some of the *QE* loss can be regained by reactivating the cathode, but at some point the cathode must be replaced.

2.3.3 Time response

The response of a photocathode represents the distribution of times when the photoexcited electrons exit the cathode. The structure of the electron bunch is governed by several factors, such as the structure of the laser pulse and the photocathode material. For fundamental research, the laser pulses have to be considerably shorter than the experimental resolution. For this reason, fast laser pulses in the order of hundred femtoseconds are preferred. In order to preserve the fast pulse structure from the laser, a photocathode with a fast response is needed. A slow response time will taint the temporal profile of the electrons, making it larger than the initial laser pulse profile.

In practice, however, even with an ideally fast laser pulse, i.e. delta-shape pulse, the response time of the cathode has a finite width. This width is the result of the finite photocathode emission time, which predominantly depends on the optical absorption length of the laser and the electron escape depth. Both of these factors depend strongly on the photocathode material.

In order to have a fast response time, these factors must be small to allow the electrons quick transport to the surface and emission to the vacuum. Optical absorption length is defined as the depth which the laser can penetrate inside the cathode before the intensity falls to $1/e$ of its original value. The absorption length for a given cathode is a function of the exciting wavelength. Electron escape depth depends on the kinetic energy of the excited electrons, and one must distinguish between the NEA and the PEA photocathodes.

In NEA cathodes, electrons may loose all their kinetic energy, thermalize to the bottom of the conduction band, and still be emitted due to the NEA state. However, in the PEA cathodes only those photoexcited electrons which do not lose their entire kinetic energy through various inelastic scatterings on their passage to

the surface will be emitted. The escape depth in PEA cathodes is given by the distance the electrons travel until they have lost their energy in the collisions and are thermalized, while in NEA photocathodes is the distance electrons travel until they recombine with the holes (in order of a few nanoseconds).

The response time of different photocathode materials as a function of the *QE* was investigated [114], and the results are presented in Fig. 2.4. For each type of photocathode, the dominant scattering mechanism is also shown.

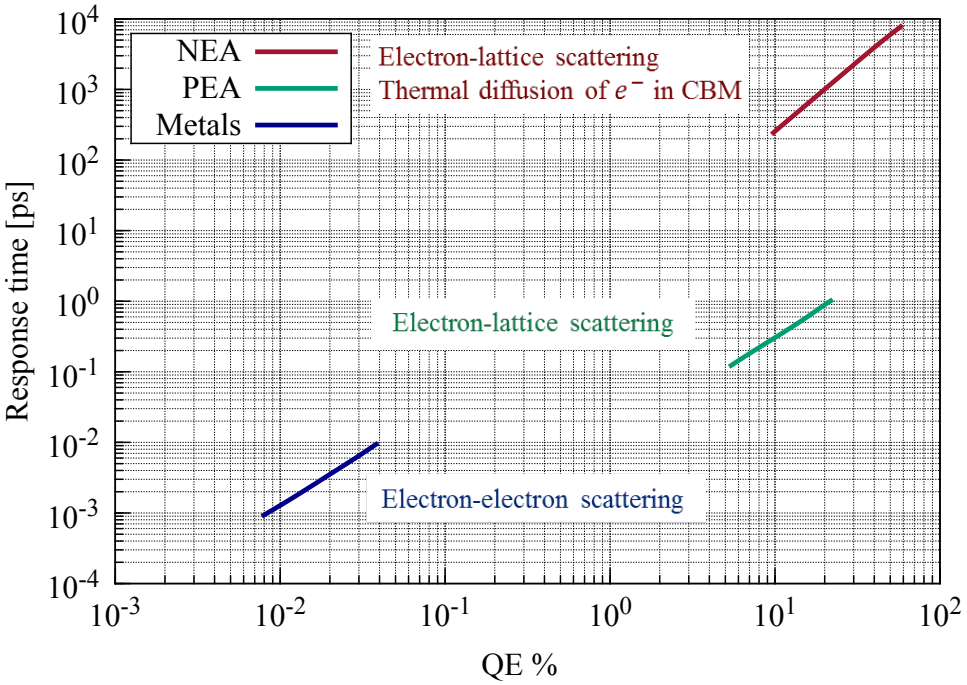

Figure 2.4: Range of time response and QE for metals, semiconductors, and NEA photocathodes according to Spicer. The dominant scattering mechanism for each type of photocathode is also shown. Reproduced from [114].

Metals have the advantage of a short optical absorption length of tens of nanometers and a short escape depth of a few nanometers. In metals, the photoexcited electrons are generated near the surface and consequently, have a better chance of reaching the surface and escaping into the vacuum. Metals are considered prompt emitters with response times in the order of sub-picosecond to femtosecond. In metals, photoexcited electrons thermalize rapidly through the inelastic interactions with the electrons in the conduction band. Thus, the electrons deep in the metal are not able to be emitted, and as a result, they have a lower *QE*.

In contrast, semiconductors have a longer optical absorption length of a few hundred nanometers. In semiconductors, the electrons are created deep within the cathode and have a higher possibility of multiple inelastic scattering processes before

emission. This prolongs the electron transit time and as a result, semiconductors typically have a longer response time in the range of several picoseconds. However, semiconductors offer a lower reflectivity compared to the metals and have a better optical absorption, allowing higher *QE* values.

In addition, semiconductors have a longer electron escape depth. The escape depth of the NEA cathodes is much larger than of the PEA cathodes. Therefore, even electrons which go through many collisions and arrive at the surface late can still be emitted. This results in higher *QE* values, but longer response time for the NEA photocathodes.

In the case of the NEA semiconductors photocathodes such as GaAs, the photoelectrons diffused in the band bending near the photocathode surface can also escape into the vacuum at very low energy, see Section 2.5. This factor further increases the possibility of multiple scatterings and causes long response times; however, it also enhances the number of emitted electrons and thus offers a higher *QE* as compared to the other semiconductors.

2.3.4 Emittance

Another important factor in characterizing the quality of the electron beam generated from a photocathode is the emittance. Generating low-emittance electron beams is crucial for the performance of most applications of photoinjectors. In general, the motion of the electron bunch is described by a six-dimensional phase space comprised of position and momentum. The six-dimensional volume is projected onto two transverse phase planes and one longitudinal phase plane.

The emittance is defined as the volume occupied by the beam in the phase space and indicates the size of the beam and its deviation. According to *Liouville*'s theorem, as the electron beam travels through the beamline, the volume remains constant [136] . However, the transverse angles decrease with momentum. The normalized emittance is defined as $\beta\gamma$ times the geometrical emittance, and can be written as

$$\varepsilon_{\mathrm{n},x} = \beta\gamma\sqrt{\langle x^2\rangle \langle x'^2\rangle - \langle xx'\rangle^2} \tag{2.4}$$

where x is the position of electrons and x' is the tangent of the angle of electrons trajectory with respect to the reference trajectory[2]. β and γ are the *Lorentz* factors corresponding to the beam velocity and energy. $\beta\gamma$ takes into account the shrinking of the angle with momentum as the electrons are accelerated.

The intrinsic emittance, also known as thermal emittance, of the beam from a photocathode is determined by the size of the laser beam and the angular spread of the electrons as they exit the cathode. The normalized transverse emittance in the x-plane (similar equation holds for the y-plane) is

$$\varepsilon_{\mathrm{n},x} = \sigma_{\mathrm{l},x}\sqrt{\frac{MTE}{mc^2}} \tag{2.5}$$

[2]For small angles, x' is equal to the angle of the trajectory.

where $\sigma_{l,x}$ denotes the RMS (root mean square) radius of the laser spot in the x-plane, m_0 is the electron mass, and c is the speed of light. *MTE* is the mean transverse energy of the emitted electrons, which depends on the photocathode material and is defined as

$$MTE = \frac{1}{2} m \left\langle v_x^2 + v_y^2 \right\rangle . \tag{2.6}$$

Lowering the laser beam size is limited by the required charge per bunch for the specific experiment. Therefore, reducing the *MTE* of the emitted electrons is the only way to further reduce the emittance. It must be noted that although low values of *MTE* are desirable in obtaining a low emittance, if the *MTE* is too low ($1-2\,\mathrm{meV}$), it will create other problems, such as disorder-induced heating [75]. *MTE* can be reduced at longer laser excitation wavelengths [138], albeit usually at the expense of other important parameters.

In accelerator applications, another important figure of merit directly related to the normalized emittance is brightness. Electron beam brightness is defined as current density per unit solid angle in the axial direction. For an electron beam with the current I traveling in the z-direction, the brightness can be written as [57]

$$B_n = \frac{2I}{\pi^2 \, \varepsilon_{n,x} \, \varepsilon_{n,y}} \tag{2.7}$$

where $\varepsilon_{n,x}$ and $\varepsilon_{n,y}$ are the transverse normalized emittances in the x and y direction, respectively. High values of brightness can be obtained by reducing the emittance.

2.3.5 Threshold for emission

The underlying condition for the photoemission process is the release of the electrons from the atomic binding when it absorbs suitable radiation energy. The photoemission process will be discussed in detail in the next section. A minimum energy is required for an electron to be removed, called the threshold energy, sometimes referred to as work function. The photon energy must be above the work function to allow the release of electrons from the solid to a point in the vacuum immediately outside of the surface of the photocathode. The work function is a characteristic property of the photocathode surface and is defined as the difference between the electron energy just outside of the surface (vacuum energy), E_V, and the Fermi level, E_F,

$$\phi = E_V - E_F. \tag{2.8}$$

If the photon energy exceeds ϕ, the excess energy appears as the electron's kinetic energy in the vacuum. In the case of metal photocathodes, electrons occupy all the states up to the Fermi level. Therefore, the threshold energy to liberate the electrons to the vacuum is same as the work function. However, in the case of

semiconductors, they have a bandgap between the valence band maximum and the conduction band minimum with energy E_{gap}. The electron affinity, χ, is defined as

$$\chi = E_{\mathrm{V}} - E_{\mathrm{c}} \tag{2.9}$$

where E_{c} is the energy of the conduction band minimum. Therefore, the threshold energy for photoemission will be the sum of E_{gap} and χ, $E_{\mathrm{th}} = E_{\mathrm{gap}} + \chi$, while the work function is the energy difference between the Fermi level and the conduction band minimum, plus the electron affinity,

$$\phi = \chi + (E_{\mathrm{c}} - E_{\mathrm{F}})\,. \tag{2.10}$$

For accelerator applications using a semiconductor photocathode, a high work function in tandem with low electron affinity is preferred. The potential barrier of a high work function obstructs the emission of the electrons generated through field emission or thermal emission. A low electron affinity increases the possibility of the photoexcited electrons exiting the photocathode and being emitted into the vacuum. In NEA photocathodes, like GaAs, the vacuum level is below the conduction band minimum. This creates a favorable condition for the electrons reaching the surface to escape to the vacuum. The NEA condition will be explained in Section 2.5.3. In PEA cathodes, however, the vacuum level lies above the conduction band minimum. Therefore, only electrons which do not lose their entire kinetic energy through inelastic scatterings with the lattice during the thermalization process can be emitted into the vacuum.

To conclude this section, it must be noted that although each of the aforementioned fundamental photocathode characteristics is crucial, very often these parameters are coupled. For example, the cathodes exhibiting high *QE*s tend to have low lifetime, while on the other hand, low-*QE* cathodes are more robust. Thermalization of the electron concentration improves emittance, but at the expense of the response time [16].

Some compromise is necessary, therefore, in choosing the appropriate photocathode material to meet the requirements of the specific application. Significant strides have been made in accelerator technology to engineer the ideal photocathode which meets most application requirements. One such example is utilizing strained superlattice structures in polarized electron sources [73], which is the subject of Section 2.6.2 and Chapter 6.

2.4 Density of states

In order to determine the carrier concentrations and the energy distributions of the electrons in the semiconductor, the *density of states* (DOS) must be known. The density of states is the number of allowed electron (or hole) states per unit volume per unit energy interval. At absolute zero temperature, an intrinsic semiconductor has electrons only in the valence band because the electrons do not have sufficient

energy to be excited to the conduction band. However, at temperatures above zero a probability of finding the electrons in the conduction band exists.

In general, the probability function of the electron occupying a state at temperature T follows the *Fermi-Dirac* statistics

$$f(E) = \frac{1}{1 + \exp\left(\frac{E - E_\mathrm{F}}{k_\mathrm{B} T}\right)} \tag{2.11}$$

where k_B is the *Boltzmann* constant. For the electron in the conduction band of a semiconductor $E - E_\mathrm{F} \gg k_\mathrm{B} T$, and the distribution can be approximated to *Boltzmann* distribution

$$f(E) = \mathrm{e}^{-\left(\frac{E - E_\mathrm{F}}{k_\mathrm{B} T}\right)}. \tag{2.12}$$

The number of electrons at the energy interval $\mathrm{d}E$ in the conduction band is obtained by multiplying the density of states, $g(E)$ by $f(E)$,

$$n = \int_{E_\mathrm{c}}^{\infty} g(E) f(E)\ \mathrm{d}E \tag{2.13}$$

where E_c is the conduction band minimum energy level. In the k-space, the number of available states in a spherical shell of radius k and the thickness of $\mathrm{d}k$ is $g(k)\mathrm{d}k$, and is approximately equal to k-space volume times the k-space density

$$g(k)\ \mathrm{d}k = 4\pi k^2 \left(\frac{V}{\pi^3}\right)\ \mathrm{d}k\,. \tag{2.14}$$

Since two electrons of opposite spin can occupy each state, the total number of electrons is twice that given by Eq. (2.14). Using the dispersion equation for the electrons in the conduction band with the effective mass m^*, one obtains

$$k^2 = \frac{2\,(E - E_\mathrm{c})\, m^*}{\hbar^2}. \tag{2.15}$$

In the above equation, the energy of the electrons in the conduction band is with respect to the conduction band minimum energy. By differentiating Eq. (2.15) and inserting it into Eq. (2.14), for a unit of volume we have [61, 121]

$$g(E)\ \mathrm{d}E = \frac{1}{2\pi}\left(\frac{2m^*}{\hbar^2}\right)^{3/2} \sqrt{E - E_\mathrm{c}}\ \mathrm{d}E \tag{2.16}$$

which provides the number of electron states in the conduction band per unit volume in the energy interval $\mathrm{d}E$. Eq. (2.16) indicates that the DOS for electrons in the conduction band of a $3D$ semiconductor is proportional to the square root of energy.

In the case of a $2D$ semiconductor, such as a finite quantum well, the density of states is independent of energy. The DOS in this case is a step function with steps occurring at the discrete energy levels,

$$g(E) = \frac{m^*}{\pi\hbar^2}\,. \tag{2.17}$$

The DOS of a superlattice can be obtained by considering the interaction of a series of finite quantum wells in the periodic potential. Due to the interaction between the wells, the DOS of a superlattice is no longer constant as it is in the finite quantum well, although it still retains a step-like behavior [94].

2.5 Photoemission from GaAs photocathode

The GaAs semiconductor is one of the first materials considered a good photoemitter of polarized electrons [105]. GaAs photocathodes belong to group III-V semiconductors. They have a large direct bandgap and can create a large NEA level, enhancing the photoemission yield. The remainder of this chapter is dedicated to discussing the fundamental properties of GaAs, the state of NEA, and the physics of the photoemission process with a special emphasis on generating spin-polarized electrons and the strained superlattice structure.

2.5.1 Crystal structure

The GaAs crystal lattice has a *zincblende* symmetry, i.e. its structure consists of two interpenetrating *face-centered cubic* (fcc) arrangements such that each atom is surrounded by four nearest neighbors located at the vertices of a tetrahedron. Fig. 2.5 shows a unit cell of the GaAs crystal structure.

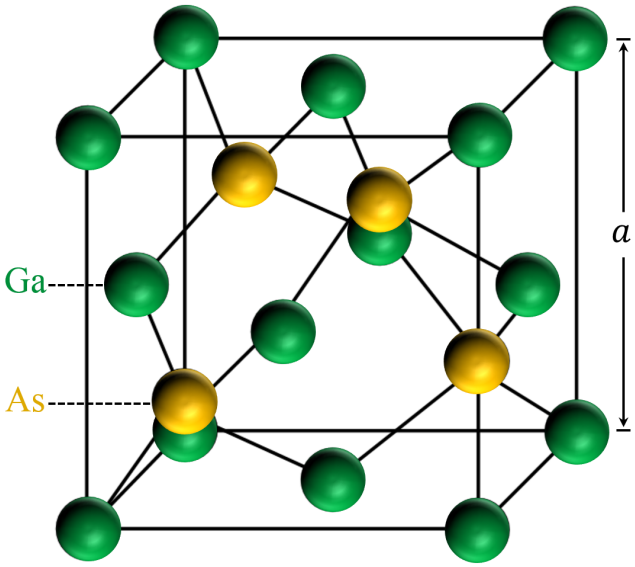

Figure 2.5: The zincblende crystal structure of the GaAs photocathodes. a represents the lattice constant.

The band structure of a semiconductor shows the energy-momentum relationship for an electron inside the material. The band structure for GaAs can be obtained

by solving the Schrödinger equation with a periodic potential. The energy band structure of the GaAs is illustrated in Fig. 2.6.

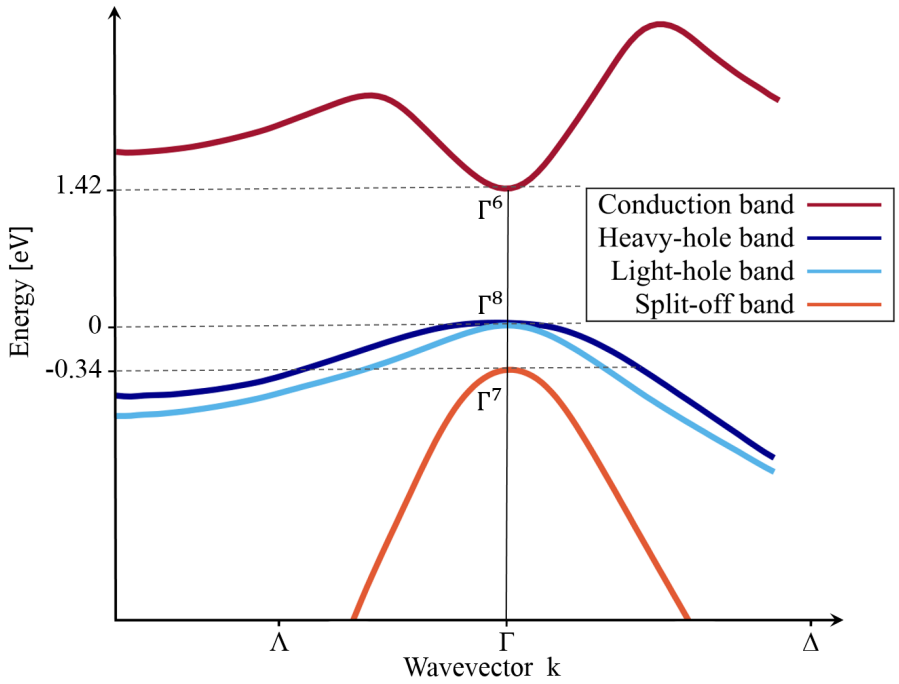

Figure 2.6: Abbreviated band structure of GaAs around the Γ point. The spin-orbit interaction creates $\Delta E_{\mathrm{so}} = 0.34\,\mathrm{eV}$ between the valence bands at Γ_7 and Γ_8. Reproduced from [90].

The valence bands and the conduction bands are separated by a gap, known as the forbidden energy gap (E_{gap}), in which no energy state for the electrons exists. The bandgap energy at room temperature is 1.42 eV and increases to 1.5 eV at 120 K. At the Γ point, the upper valence band with angular momentum $l = 1$ has a three-fold degeneracy. Including the spin, the degeneracy breaks due to spin-orbit interaction. The upper two degenerate bands at the Γ point are known as *heavy hole* (Hh) and *light hole* (Lh) bands due to different effective masses.

The dispersion relationship near the bandgap for an electron with an effective mass of m^* can be approximated with a quadratic equation

$$E_k = \frac{\hbar^2 k^2}{2m^*} \tag{2.18}$$

The curvature of the two parabolic bands at the valence band maximum represents the effective mass of the Hh and Lh bands,

$$m^* = \hbar^2 \left(\frac{\mathrm{d}^2 E}{\mathrm{d}k^2} \right)^{-1}. \tag{2.19}$$

Different crystal properties of the GaAs semiconductor according to [61] are listed in Table 2.1.

Table 2.1: Properties of GaAs crystal

GaAs property	**Parameter**
Lattice constant	$a = 5.65\,\text{Å}$
Nearest neighbor distance	$d = \frac{\sqrt{3}}{4}a = 2.45\text{Å}$
Angle between the bonds	109.47°
Density	$5.32\,\text{g}\,\text{cm}^{-3}$
Hh effective mass	$0.45\,m_\text{e}$
Lh effective mass	$0.082\,m_\text{e}$
Effective mass of electrons in CB	$0.067\,m_\text{e}$
Spin-orbit splitting energy	0.34 eV

Any photoexcited electron transition from the valence band to the conduction band requires the conservation of energy and momentum. One advantage of the direct-bandgap crystals is that the electrons move directly from the valence band to the conduction band without any phonon absorption or emission, leading to a high photon absorption. Different crystal properties of GaAs are listed in Table 2.1.

2.5.2 Photoemission process

Einstein published his quantum theory of photoemission in 1905 [40]; however, over half a century passed before researchers were able to obtain a comprehensive understanding of the photoemission process. The initial groundwork for explaining the photoemission process of electrons from a semiconductor into vacuum was laid by William Spicer in 1958 in what is known as Spicer's three-step model [115]. Prior to Spicer's description, photoemission had been considered a pure surface effect. Spicer, in contrast, described the process as a bulk phenomenon in terms of bulk optical constants, electron scattering length and surface properties, such as the work function at the surface of crystal.

Spicer's photoemission model consists of three main steps. These steps are illustrated in Fig. 2.7.

① *Photoexcitation* of electrons from the valence band into the conduction band

② *Transport* of electrons to the surface

③ *Emission* of electrons from the surface into the vacuum

In the first step, electrons in the valence band are excited to the conduction band by absorbing photons, and holes are generated in the valence band. According to *Bouguer*'s law [88], the intensity of the incident light decreases exponentially with

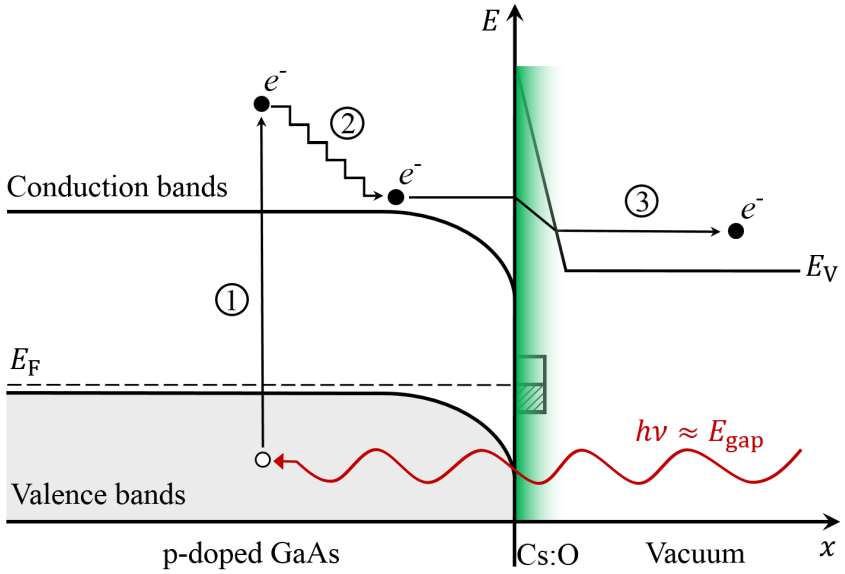

Figure 2.7: Schematic presentation of the Spicer's three-step model. Step ① represents the photoexcitation of the electrons as they are illuminated with the laser energy slightly above the E_{gap}. In step ② electrons are thermalized and transported to the surface, and in step ③ they are emitted to the vacuum.

the thickness of the photocathode. This dependence means the probability of a photon being absorbed decreases exponentially with the distance travelled.

The optical absorption coefficient is an important factor in the photoemission process. The absorption coefficient determines the depth at which a light of a certain wavelength can penetrate in the material before it is absorbed. The absorption coefficient depends on the photocathode material and also on the excitation wavelength. Direct-bandgap semiconductors, such as GaAs, offer the highest absorption coefficients, and thus are considered good photoemitters [135]. The absorption coefficient, α, of GaAs in the vicinity of the bandgap when excited with photons with energy E_γ follows the proportionality

$$\alpha \propto \sqrt{E_\gamma - E_{\text{gap}}} \tag{2.20}$$

Comparing Eq. 2.20 with Eq. 2.16 suggests absorption coefficient is proportional to the DOS of the bulk semiconductor. Absorption coefficient of GaAs at 800 nm excitation wavelength is in the order of $\alpha \approx 1\,\mu\text{m}^{-1}$. This means the electrons are generated relatively deep inside the material at a typical absorption length of $\alpha^{-1} \approx 1\,\mu\text{m}$ and they have to travel "far" to come to the surface.

In the second step, the photoexcited electrons are transported to the surface of the photocathode. During the transportation, electrons undergo different scattering processes with phonons and other electrons; they lose energy and thermalize at the

conduction band minimum [113]. The time required for the electrons to thermalize is in the order of 0.1–1 ps, corresponding to a length of about 100 nm [114]. Typically, the thermalized electrons can live for only nanoseconds before they recombine with the holes in the valence band.

Electrons lose their energy through different processes such as acoustical and phonon scattering and recombining with holes. For GaAs heavily p-doped at concentration of $1 \times 10^{19}\,\mathrm{cm}^{-3}$, the electron-hole recombination is the dominant energy loss mechanism [26]. The energy of electrons after thermalization is approximately $k_\mathrm{B}T$, where k_B is the Boltzmann factor and T denotes the temperature. At room temperature, the electron energy is approximately 25 meV.

Comparing the thermalization and recombination time, another process besides thermalization is obviously involved during the transport of electrons to the surface. For heavily doped NEA photocathodes, the mean free path is significantly smaller than the active layer thickness, $\lambda \ll d$, and thus the electron transport can be expressed by the diffusion model. According to *Fick*'s first law, the diffusion flux is proportional to the concentration gradient [127]. The electrons concentration at each point in time inside the cathode, $c(r,t)$, according to Spicer is given by

$$\frac{\partial}{\partial t}c(r,t) = g(r,t) - \frac{1}{\tau_\mathrm{rec}}c(r,t) + D\frac{\partial^2}{\partial x^2}c(x,t) \tag{2.21}$$

where $g(r,t)$ describes the generation of conduction band electrons by photoexcitation. Assuming an infinitesimally short laser pulse, $g(r,t)$ will be zero. The term $\frac{1}{\tau_\mathrm{rec}}c(r,t)$ represents the reduction of the conduction electron concentration by recombination. The last term in (2.21) describes the electron movement by diffusion. D is the *diffusion constant*, which expresses the ease of electron diffusion in response to a concentration gradient and is limited by vibration of the lattice atoms and ionized dopant. The diffusion constant in p-doped materials is a linear function of electron mobility μ by *Einstein's relation*

$$D = \frac{\mu k T}{e}\,. \tag{2.22}$$

The average distance an electron travels before recombination with the holes is called *diffusion length* and can be found with

$$L_D = \sqrt{D\tau_{rec}}\,. \tag{2.23}$$

The transport process can be described by the *mean free path*

$$\lambda = \frac{3D}{\bar{v}} \tag{2.24}$$

where $\bar{v} = (2/\sqrt{\pi})\sqrt{2kT/m^*}$ is the average velocity of the thermalized electron ensemble and m^* is the electron effective mass in the conduction band. For GaAs, the diffusion constant is approximately between 30–80 $\mathrm{cm}^2\,\mathrm{s}^{-1}$ depending on the doping [112]. The lower (higher) value corresponds to high (low) doping density of

$1 \times 10^{19}\,\mathrm{cm}^{-3}$ ($1 \times 10^{17}\,\mathrm{cm}^{-3}$). This correspondence will result in a mean free path between 30 nm (high doping) and 55 nm (low doping) and yield a typical diffusion length of $L_\mathrm{D} \approx 2\,\mu\mathrm{m}$. The diffusion length is in the same order as the 800 nm light absorption length $\frac{1}{\alpha} \approx 1\,\mu\mathrm{m}$.

This data validates the proposition of the diffusion process during the transport mechanism and the fact that a large number of photoexcited electrons reach the cathode surface during the diffusion process. The solution to the diffusion model and the specific implications in the case of the GaAs photocathode used in the present research will be discussed later in Section 5.6.

In the third step, electrons reaching the surface cross the *band-bending region* (BBR), tunnel through the potential barrier, and are emitted into vacuum. Electrons approaching the surface can be trapped in the empty surface states within the band bending region. The probability of electrons escaping from the surface into vacuum depends strongly on the photocathode surface characteristics and on the nature of the surface states.

The electron surface density and the electron-phonon interactions are the controlling factors for the electron transitions in the surface states. Since the density of the surface states is very high, excited electrons which are trapped in the BBR will lose their energy to the GaAs surface region and eventually recombine with the holes in the valence band. For an electron to escape into vacuum, the electron's final energy after thermalization and phonon interactions must be above the vacuum level. For GaAs, the surface can be treated so that the vacuum level falls below the conduction band minimum.

2.5.3 Negative electron affinity

In the photoemission process, to achieve a successful emission of electrons into vacuum, the vacuum level must be below the electron's energy level. The probability of electrons escaping into vacuum can be greatly enhanced by achieving a NEA state on the surface. According to Eq. (2.9), an NEA state is obtained when the vacuum level lies below the conduction band minimum. One of the advantages of the group III–V semiconductor photocathodes is their ability to obtain NEA. Lowering the vacuum level below the conduction band minimum occurs in two steps. These steps are demonstrated in the energy band diagram of a typical III–V semiconductor in Fig. 2.8.

In the diagrams, which illustrate the energy on the y-axis and the space coordinate perpendicular to the surface of the cathode on the x-axis, E_vb, E_cb, E_V, and E_F, denote the energy level at valence band, conduction band minimum, vacuum, and Femi level, respectively. The Fermi level in intrinsically undoped GaAs crystals is near the middle of the bandgap, illustrated in Fig. 2.8, (a).

When the GaAs photocathode is heavily p-doped (for example by zinc atoms with concentration in the range of $10^{18} - 10^{19}\,\mathrm{cm}^{-3}$), the Fermi level inside the crystal is lowered to a value right above the valence band maximum. However, Fermi level is pinned on the surface region somewhere in the bandgap according to the surface

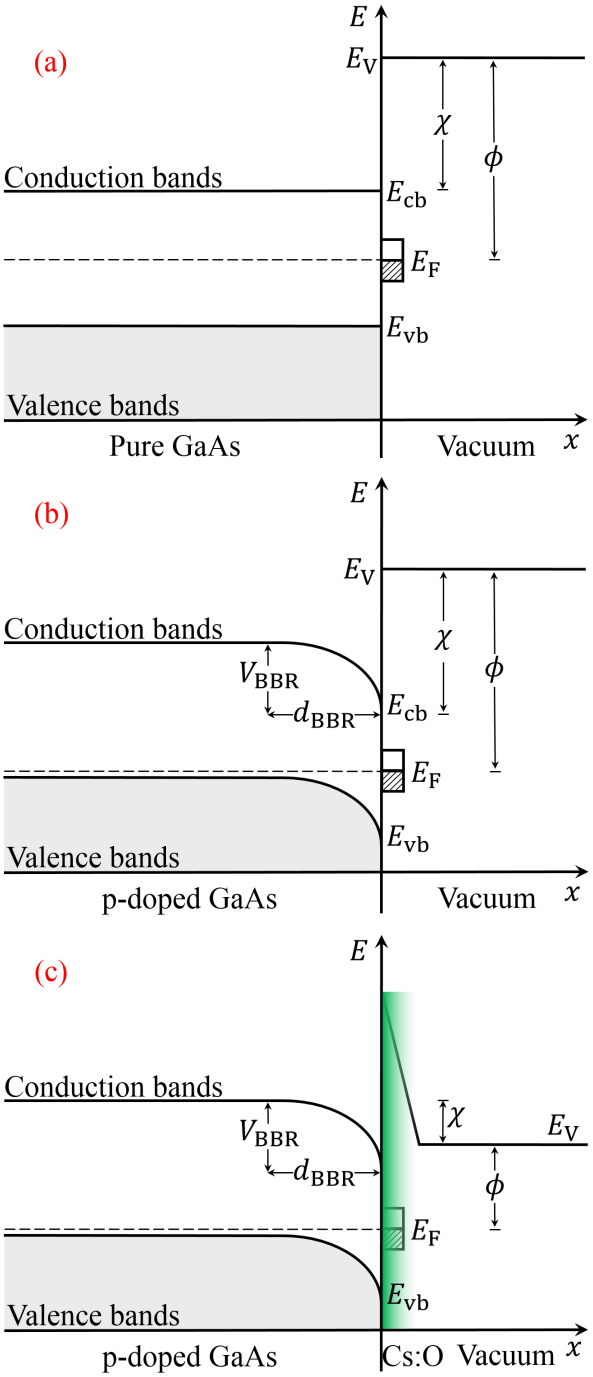

Figure 2.8: Schematic representation of achieving the state of NEA. (a): pure Bulk GaAs; (b): p-doping GaAs lowers E_V and creates the BBR, and (c): Cs : O layer lowers the vacuum level below E_{cb} and creates the state of negative electron affinity.

conditions. The Fermi level must remain constant in thermal equilibrium. This results in bending of the bands inside the crystal towards the surface, which in turn forms the band-bending region near the surface [104] and reduces the vacuum level, as shown in Fig. 2.8, (b).

A co-deposition of Cs and O_2 on a p-doped GaAs photocathode surface significantly lowers the vacuum level and reduces the electron affinity of the crystal to negative values with respect to the valence band minimum [105]. This is illustrated in Fig. 2.8, (c). Although the precise nature of the deposition of Cs and the oxidant is not fully understood, a possible explanation is the formation of a dipole layer. In this model, the desorption of Cs induces donor-like surface states. Therefore, the surface will have a positive charge, and the region immediate to the surface will become negatively charged. This induced electric field further decreases the vacuum level and the electron affinity. The co-deposition of O_2 will intensify this effect leading to an additional decrease of the vacuum level. The width of the BBR is given by [121]

$$d = \sqrt{\frac{\epsilon\epsilon_0}{2\pi e^2}\frac{eV_{\mathrm{BBR}}}{N_{\mathrm{p}}}} \tag{2.25}$$

where ϵ and ϵ_0 are the dielectric constant of the material and the vacuum, respectively. V_{BBR} denotes the band bending potential, and N_{p} is the doping concentration. In practice, a narrow BBR is desirable since a wide BBR increases the electron-phonon scattering, and thus decreases the probability of electron escape into vacuum. Since a high V_{BBR} is favorable, shortening of d can be achieved by increasing the concentration of the dopant. However, too high of doping density will increase electron spin relaxation, which is not desirable in producing spin-polarized beam.

Therefore, a compromise must be made in choosing a doping concentration which delivers a high escaping probability and high polarization. With high p-doping density in the order of $10^{19}\,\mathrm{cm}^{-3}$, a band-bending region with a width of $\approx 10\,\mathrm{nm}$ is obtained with a band bending potential of $0.3 - 0.5\,\mathrm{eV}$ [37]. The co-deposition of Cs and an oxidant on the GaAs surface gives the major contribution to the enhancement of the GaAs photocathode characteristics such as high *QE*, as discovered by Scheer and Spicer [91, 105].

According to Spicer's model, the photoexcited electrons thermalize at the conduction band minimum, and when their kinetic energy is above the E_{cb}, they can escape into vacuum. A simple assumption infers that all the electrons have constant energy during the escape process. However, this assumption is erroneous.

The energy distribution of an electron beam as a function of the longitudinal ($E_{\parallel}$) and transverse ($E_{\perp}$) energy in a photoemission process from GaAs (Cs, O_2) at 90 keV was studied in [86] by *Orlov et al.*. $E_{\parallel}$ and $E_{\perp}$ are electron energies associated with their momentum parallel and perpendicular to the GaAs crystal surface normal. The GaAs photocathode was activated to an NEA of 280 meV. Fig. 2.9 represents the complete energy distribution of photoemitted electrons [86].

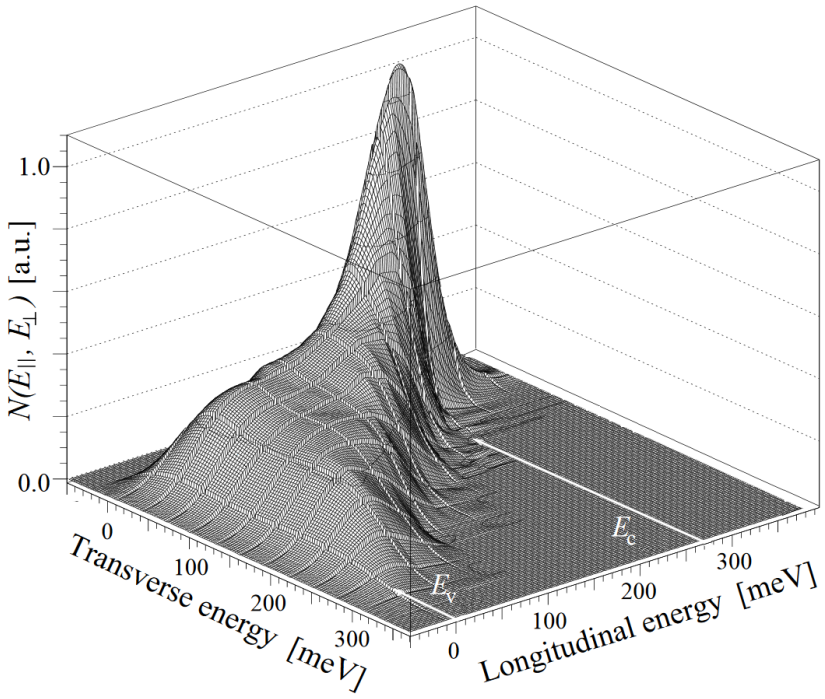

Figure 2.9: The complete energy distribution of the photoelectrons as a function of the longitudinal and transverse energy. Energy at conduction band minimum (E_c) and vacuum energy (E_V) are shown in the figure. Figure modified from [86].

Figure 2.9 demonstrates an exponential decay of the electron yield in both the transverse and longitudinal direction for energies above the conduction band minimum. However, for energies below E_c, the distribution is not exponential and is governed by complicated scattering processes in the band bending and surface region. Furthermore, while the mean transverse energy of electrons in the bulk was about 8 meV, the photoemitted electrons were found to have a wide transverse energy distribution with an MTE of 75 meV [86]. These energy distributions clarify some of the details of the emission process and clearly show the influence of elastic and inelastic electron scattering processes on the energy loss near the interface during the escape process.

2.6 Polarized electrons

As discussed earlier, group III-V semiconductors, and specifically GaAs, are the most useful sources of polarized electrons. Since the first measurement by Pierce in 1976 [91], NEA photocathodes have been used as a source of polarized electron beams for almost half a century. The orderly band structure of GaAs allows se-

lection of a specific spin state from the valence band to the conduction band and, thus, the generation of polarized electron beams.

The generation of spin-polarized electrons can be explained best by using the energy band diagram. Figure 2.10 demonstrates the energy bands for a GaAs photocathode where the degeneracy between the Lh and Hh bands is broken.

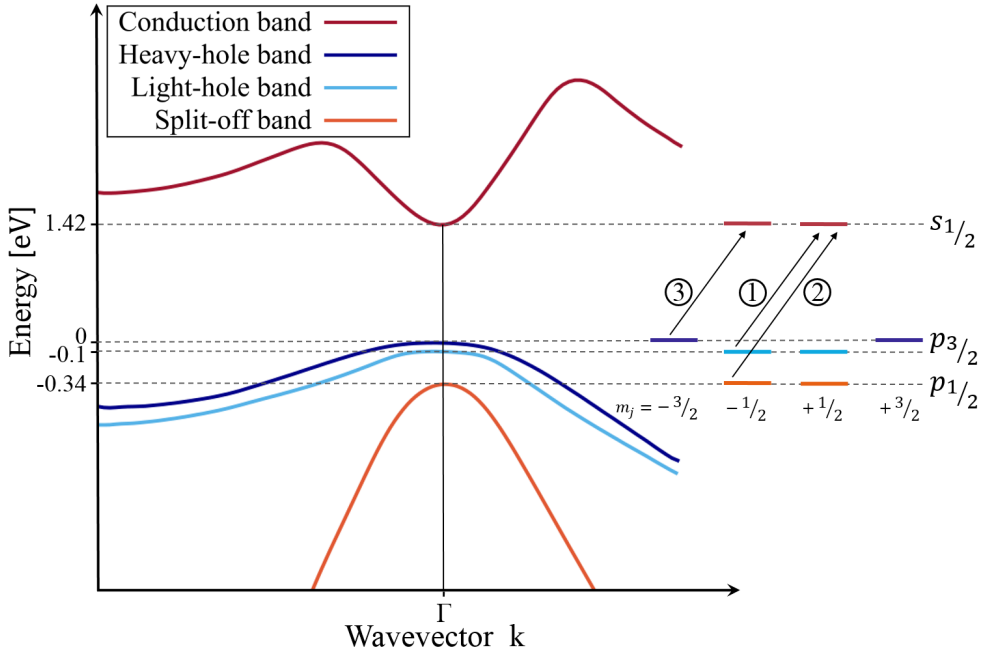

Figure 2.10: Energy bands of a strained GaAs crystal where the degeneracy between the Lh and Hh is broken. By using a circularly polarized light of specific energy, the generation of polarization approaching 100 % is possible. The arrows indicate the allowed transitions for light of positive helicity. Next to the arrows are the relative transition probabilities obtained from the Clebsch-Gordan coefficients indicated in circles. Similar transitions can be obtained for light of negative helicity.

When a bulk GaAs photocathode is illuminated with a circularly polarized light of energy between $E_{\mathrm{gap}} < E < E_{\mathrm{gap}} + \Delta E_{\mathrm{so}}$, where ΔE_{so} is the split-off energy, the transitions from the split-off band are restricted. Therefore, transitions are possible only from the upper valence band. This selective transition results in generation of polarized electrons. Following the quantum mechanical selection rules, only transitions with $\Delta m_j = \pm 1$ from the top two degenerate valence bands, the $p_{3/2}$ states, are allowed, see Fig. 2.10. The relative transition probabilities from each of the states can be obtained from the *Clebsch-Gordan* coefficients. These probabilities are shown in circles for a circularly polarized light of positive helicity. This selective excitation leads to a maximum achievable polarization of 50 % for bulk GaAs.

The quality factor for polarized electron source delivering a beam with quantum efficiency of QE is defined as $QE \cdot P^2$, where P is the measured polarization. Thus, achieving higher polarization values is desirable for polarization applications. One successful technique to generate higher polarization electron beams involves introducing mechanical strain in the GaAs crystal. In practice, two main types of photocathodes have this feature: the strained photocathodes and strained superlattice (SSL). The specific design structures and physical basis of these cathodes are discussed in the following section.

The induced strain lifts the degeneracy between the heavy-hole and light-hole bands at $k = 0$, creating different bandgap energies between these bands and the conduction band minimum, as shown in Fig. 2.10. Using circularly polarized light with only enough energy allows selective excitation of electrons from one type of spin state [91]. Theoretically, electron beams can be generated with polarization approaching 100 %. In practice, however, the achievable polarization falls lower than the expected value [92], due to lattice imperfections and other depolarization effects occurring during the transport and emission of electrons. The discussion of depolarization mechanisms in GaAs crystal is deferred to Section 2.6.3.

2.6.1 Strained photocathodes

The cubic symmetry structure of the GaAs crystal results in a four-fold degeneracy of the Hh and Lh valence energy levels. Breaking the symmetry of the crystalline structure through introducing an axial strain within the GaAs crystal structure induces valence band splitting, allowing higher polarization. *Maruyama et al.* were the first to achieve polarization in excess of 50 % by using this approach [72, 82]. In practice, strained layers are formed by growing a thin layer of a photocathode material on a substrate with a slightly smaller lattice constant. In the contact plane between the two layers, the epilayer lattice is compressed to adapt to the lattice constant of the substrate, thereby forcing the epilayer to stretch in the normal direction. This strain deformation leads to the splitting of the valence bands.

In order to induce an effective strain to deliver higher polarization, the bandgap of the substrate must be larger than the bandgap of the strain epilayer to ensure that photoemission occurs only from the epilayer. In addition, the strain must be great enough to create a large split between the Hh and Lh bands to warrant a selective transition. Furthermore, the thickness of the epilayer must not exceed the critical thickness. Critical thickness is the thickness at which the strain relaxation appears via misfit generation at the strained layer interface. Hence, exceeding the critical thickness will result in polarization reduction.

Denoting a_{S} and a_{L} as lattice constants for the substrate and the epilayer respectively, the lattice mismatch is defined as

$$\epsilon = \frac{a_{\mathrm{S}} - a_{\mathrm{L}}}{a_{\mathrm{S}}}. \tag{2.26}$$

For a GaAs strained epilayer grown on a $\mathrm{GaAs_{1-x}P_x}$ buffer layer, where x is the fraction of phosphorus, the lattice mismatch can be written [25, 82] as a function

of the fraction parameter

$$\epsilon = 0.036\, x \tag{2.27}$$

The energy splitting between the Hh and Lh bands (δ) and the bandgap energy at room temperature are estimated as

$$\delta_x = 6.5\, \epsilon \ \text{(eV)} \tag{2.28}$$

$$E_{\text{gap}} = 1.424 + 1.150\, x + 0.176\, x^2 \tag{2.29}$$

and the critical thickness (in unit of Angstrom) is estimated as

$$t_{\text{c}} \approx \frac{0.224}{\epsilon} \left[1 + \ln \frac{t_{\text{c}}}{4.00} \right] \tag{2.30}$$

The numerical values for the parameters and estimations can be found in [25]. For a phosphorus content of 36 %, which is investigated in the strained superlattice $GaAs_{1-x}P_x$ during the course of this project, the parameter values listed in Table 2.2 were obtained.

Table 2.2: Crystal properties of $GaAs_{1-0.36}P_{0.36}$

GaAsP property	**Parameter**
Substrate lattice constant	$a_{\text{S}} = 5.727\,\text{Å}$
Epilayer lattice constant	$a_{\text{L}} = 5.653\,\text{Å}$
Lattice mismatch	$\epsilon = 0.013$
Bandgap energy	$E_{\text{gap}} = 1.861\,\text{eV}$
Valence band splitting	$\delta = 0.084\,\text{eV}$
Critical thickness	$t_{\text{c}} = 6.640\,\text{nm}$

A single strained-layer cathode can deliver higher polarizations. However, the maximum achievable polarization is limited due to both the limited valence band splitting and the strain relaxation in the epilayer, as the critical thickness is exceeded for large strain. To overcome this deficiency and obtain higher polarizations, the research has shifted to developing strained superlattices.

2.6.2 Strained superlattice photocathodes

Strained superlattice (SSL) structures consist of a periodic design of strained layers sandwiched between unstrained lattice layers, where the thickness of each layer is less than the critical thickness. Since the bandgaps of these alternating layers are different, a SSL structure creates potential quantum wells and barriers. The electrons' allowed energy levels within each quantum well are quantized according to Schrödinger's equation. However, if the barrier width is sufficiently small (several nanometers), electron wave functions from the neighboring well will begin to overlap, forming continuum energy bands called minibands.

Figure 2.11 depicts the energy band structure of the GaAs/GaAsP strained superlattice. The relative locations of the minibands in the conduction band and valence band are indicated.

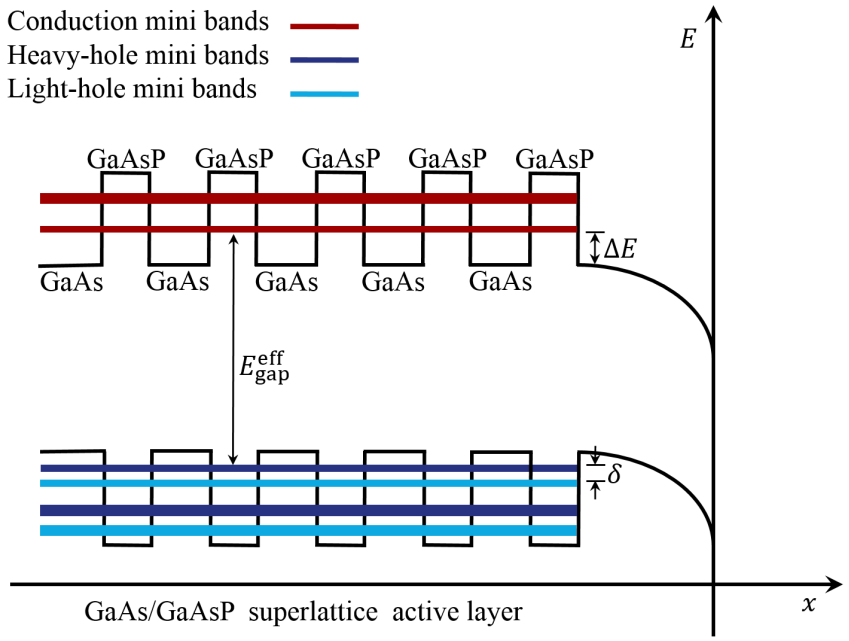

Figure 2.11: The strained GaAs/GaAsP superlattice band structure demonstrates the natural splitting of the Hh and Lh valence bands. The GaAs layers are wells and strained, and the GaAsP layers are potential energy barriers. ΔE represents energy difference between the bottom of the conduction mini-band in GaAs/GaAsP superlattice and the conduction band minimum in GaAs. δ defines the energy splitting between the Hh and the Lh valence bands.

The valence band energy splitting in an SSL is further increased compared to a single strained layer. This increase is due to the difference in the effective mass of the Hh and Lh causing a natural splitting of the valence bands, which adds to the strain-induced splitting. Moreover, each of the superlattice layers is thinner than the critical thickness, but the total activation layer thickness can exceed the critical thickness of the photocathode. As a result, in strained superlattice the strain can be preserved to a higher degree than in a single strained layer. Therefore, SSL photocathodes overcome the deficiencies of a strained GaAs cathode and make them superior to the latter. Thus, polarization values from a SSL cathode are inherently significantly higher. Electron accelerators have routinely achieved electron spin polarizations exceeding 80 % with strained superlattice GaAs/GaAsP photocathodes [73, 81]. Fig. 2.12 illustrates the structure of the GaAs/GaAsP SSL which was investigated in this project.

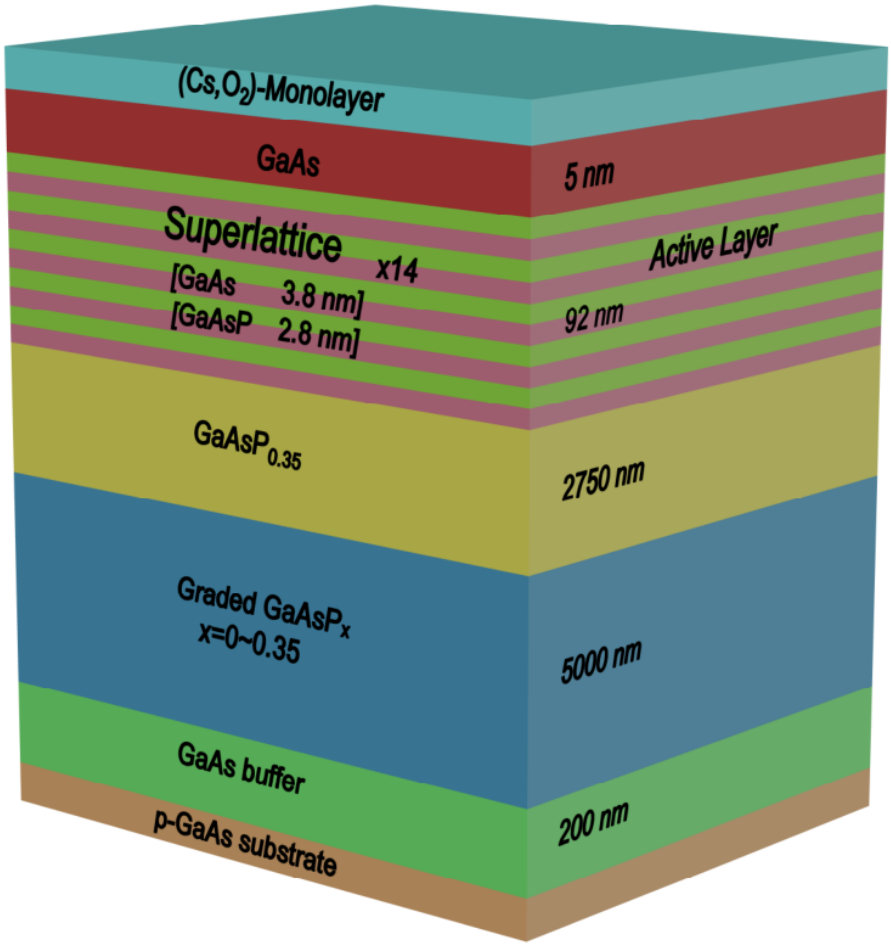

Figure 2.12: Schematic crystal layer structure of strained GaAs/GaAsP superlattice which is investigated in this work.

The epitaxial growth of the materials on a substrate in the structure of the strained superlattice are carried out by several different techniques such as molecular beam epitaxy (MBE) and metalorganic chemical vapor deposition (MOCVD). The GaAs/GaAsP SSL investigated in the course of this research was fabricated using an MBE method. In the MBE growth process, fluxes of the respective elements converge on a heated wafer to form the desired compound in a controlled environment. The MBE technique allows for very precise control over the flux at which an element is deposited and how thick the layer becomes; and as a result, high-purity layers can be obtained. Any variations in the uniformity of the layers lead to fluctuations in the mini-band structure and can affect the transport process of the electrons.

A few points must be considered regarding the structure of a strained superlattice photocathode. First, increasing the barrier thickness enlarges the valence band

splitting and delivers higher polarization. However, a thicker barrier decreases the probability of the electron transport and, therefore, reduces the *QE*. For practical purposes, the thickness of the barrier must be optimized for the polarization and *QE*.

Second, generally a superlattice is designed with a high p-doping density near the surface (in the 10 nm region) to allow large band bending and thereby a large NEA. Higher p-doping density, on one hand, leads to higher *QE*s and reduces the surface electron trapping, which is responsible for the surface charge limit, see Section. 2.7. On the other hand, increasing the doping density results in a higher probability of spin depolarization. For this reason, a lower doping density is usually used in the remaining sections of the superlattice to reduce the depolarization.

2.6.3 Depolarization processes

The polarization of the electrons generated in the photoemission process in the conduction band is not constant but decays exponentially with time. The electron spin is subject to depolarization due to various processes in the bulk of semiconductors which may occur before recombination of the conduction band electrons. Different spin relaxation mechanisms and their relative strength are discussed extensively in [21, 41, 93, 139], from which most of the material in this section was obtained.

Two major spin relaxation processes exist in p-type semiconductors with medium to high doping density near room temperature, namely the *Bir-Aronov-Pikus* (BAP) process and the *D'Yakonov-Perel* (DP) process.

In the BAP process, the strong efficiency of electron scattering by holes is considered in the spin relaxation. The rate of electron spin relaxation due to holes is proportional to the time of interaction with the holes [21] and can be written as

$$\frac{1}{\tau_s} = N_\mathrm{h}\,\sigma_\mathrm{BAP}\,v \tag{2.31}$$

where N_h is the concentration of holes, σ_BAP represents the spin-flip cross section, and v is the velocity of the electrons. In GaAs, σ_BAP is in the order of $10^{-18}\,\mathrm{cm}^2$. In highly doped GaAs, ($10^{17} - 10^{19}\,\mathrm{cm}^{-3}$), the BAP process is considered to be the dominant relaxation mechanism at low temperatures. The typical spin relaxation rate in this process is between 2×10^{10} and $4 \times 10^{10}\,\mathrm{s}^{-1}$. At room temperature, the spin relaxation time is typically about 50 ps [10], and therefore, it may no longer be neglected for electron pulses with a temporal length of a few picoseconds. As a result, for such pulses, a time-dependent decrease in polarization is expected.

The DP process arises from the lack of inverse symmetry in the III-V semiconductor crystal structures. This asymmetry leads to a splitting of the conduction band spin up and down states for $k \neq 0$. In zincblende crystals, such as GaAs, the spin splitting near the Γ-point is proportional to the cube of the electron momentum. This spin splitting occurs in a manner analogous to the effect of a magnetic field inducing the precession of electron spins. The DP mechanism can predominate at relatively low doping density levels ($< 10^{17}\,\mathrm{cm}^{-3}$) and at high temperatures.

In DP process, typical spin relaxation rates are between 4×10^9 and $2 \times 10^{10}\,\mathrm{s}^{-1}$. Since the GaAs photocathodes investigated in this work have a high doping density of $10^{19}\,\mathrm{cm}^{-3}$, the DP process does not have a large impact on the spin relaxation of the cathodes. Fig. 2.13 shows the boundaries of temperature and doping density regions within which the BAP and DP spin relaxation mechanisms in a GaAs crystal predominate.

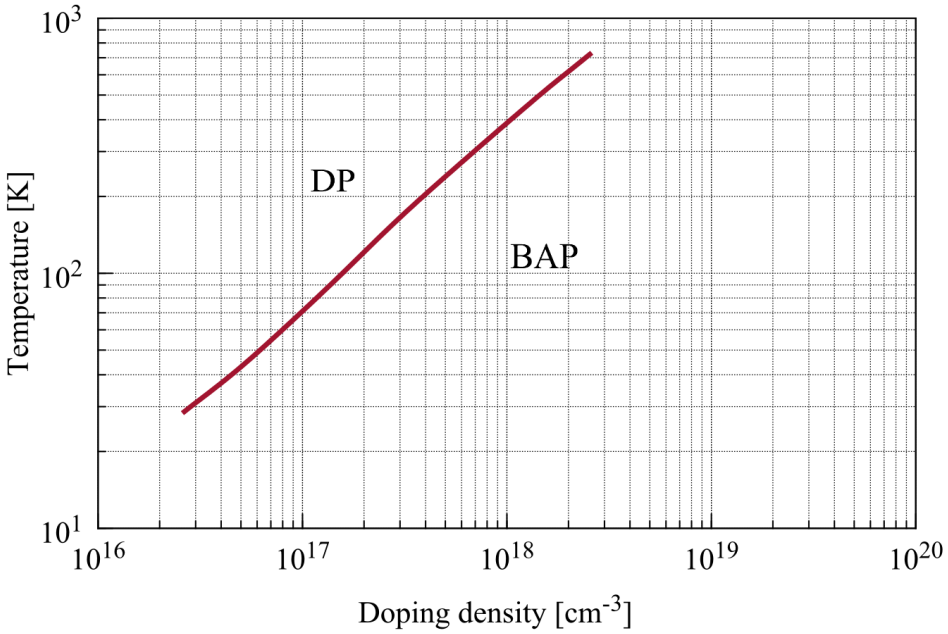

Figure 2.13: Boundaries between the temperature and doping density regions in which the BAP and DP spin relaxation mechanism predominates for GaAs crystal [7].

2.7 Surface charge limit

Negative electron affinity photocathodes can be excited with short laser pulses. By increasing the laser power the photocathodes have the potential to produce high peak currents. The *surface charge limit* (SCL) at high-excitation laser power restricts this process, however, and the extracted average current density is limited.

At high-power illumination, a large number of electrons are excited from the valence band to the conduction band. A small fraction of electrons exit the cathode and are emitted into the vacuum. However, the excess electrons are trapped in the band bending region and produce an opposing field which deflects the subsequent electrons arriving at the surface. As a result, the vacuum level rises, and the escape probability of the electrons is reduced. Since the surface potential changes at high-intense optical illumination, this effect is referred to as *surface photovoltage effect*.

In 1995, *Woods et al.* at SLAC were the first to observe SCL phenomena with a bulk GaAs photocathode and electron source operated at 120 kV [137]. Since then, many research groups have investigated the SCL phenomenon in a wide variety of photocathodes. For example, *Saez et al.* [101] and *Tang et al.* [124] studied this phenomenon in a variety of bulk and strained GaAs photocathodes with different doping concentrations. In [54], the studies of SCL on thin unstrained GaAs were conducted. Later, in 1998, the effect of the SCL was extensively studied by *Togawa et al.* in GaAs/AlGaAs superlattice and InGaAs/AlGaAs strained superlattice with different doping densities [130]. *Malhollan et al.* followed with an investigation of the effect with a set of thin GaAs with active layer of 100 nm [79].

The effect of the surface photovoltage is further explained in Section 5.7.1 where the low *QE* investigations of the bulk GaAs are discussed.

3 Experimental setup

3.1 PKAT transport system

In the early 1990's the researchers conceived the idea of a pulsed source of polarized electrons to satisfy the needed increased efficiency of the MAMI[1] accelerator. In 1993 this idea came to fruition [9, 50] with the construction of the PKAT[2] beam line, which allowed for the time-resolved measurements of the intensity and polarization of the electron pulses emitted from the cathode.

PKAT is a low-energy beam transport system designed with the assistance of the Beam Optic simulation program [50, 117]. The PKAT electron source is identical to the MAMI source injector systems [9]. Furthermore, the PKAT is equipped with an ultra-high vacuum loadlock transport system which allows photocathodes to be transported to and from the source without breaking the vacuum [80].

For more than two decades PKAT has been operating, allowing for conducting of independent measurements [103, 108] and serving as a testing center to investigate properties of the photocathodes, both with polarized and unpolarized beams. Important properties, such as quantum efficiency, lifetime, emittance, and the degree of polarization were explored before the routine use of the cathodes at the MAMI accelerator.

Occasionally, the PKAT transport apparatus has been modified. For example, the Torus condenser was removed due to lack of space in order to perform beam-induced fluorescence (BIF) and Thomson scattering (TLS) measurements [133]. Other modifications were a renewal of the high frequency system, i.e., replacing the Klystron with a new high-frequency semiconductor amplifier, commissioning of the new frequency-doubler laser system, and installing the analyzer slit and channeltron [60]. In addition, to resume time-resolved polarization measurements after removing the Torus condenser, the Wien filter spin rotator was added to the PKAT beamline. The latter was commissioned specifically in the context of this project.

Since the beginning of its use, PKAT has supported the performance of time-resolved measurements of the emission of photocurrents, and the measurements of the longitudinal halo. Longitudinal halo is the part of electron pulse not contained in the longitudinal acceptance of the accelerator. The losses associated with the longitudinal halo must be minimized as they can cause harm to the cathode, accelerator components, and the surrounding. Different types of photocathodes have been

[1] Mainzer Mikroton
[2] Polarisierte Kanone Test

investigated, including: bulk GaAs [35, 99, 100, 107, 134] and multi-alkali K_2CsSb photocathodes [18, 60]. In the time-resolved investigations of InAlGaAs/GaAs superlattice, a longitudinal halo of 1 % compared to the maximum intensity was reported [45].

Furthermore, polarization and time-resolved measurements of spin polarization have been conducted with variety of photocathodes, such as strained GaAsP [50, 107], InAlGaAs/AlGaAs crystals with integrated DBR [100], and a GaAs/GaAsP strained superlattice photocathode. The latter of which has been investigated in the course of this project.

3.2 Experimental structure

The PKAT transport system is comprised of a DC photoemission electron source with an almost 7-meter-long beamline for beam diagnosis. A schematic drawing of the PKAT structure is shown in Fig. 3.1.

The electron source, which operates with a fixed voltage, consists of a main electrode, an anode, and an intermediate electrode. The intermediate electrode is connected to a variable potential, creating the ability to set different extraction gradients. After the laser pulse is generated, it is reflected via 7 mirrors before passing through a telescope, located directly under the first α-magnet. The laser then illuminates the photocathode vertically from below. The generated electron pulses are accelerated into vacuum, anti-parallel to the laser beam. Later, the electron pulses are deflected from vertical to horizontal at an angle of 270° with the help of an α-magnet [117].

A large quantity of small correcting magnets are located throughout the PKAT beamline to correct the beam position. The beamline also includes several screens for beam diagnosis and a differential pumping stage to separate the source vacuum (kept at pressures in the low 10^{-10} mbar) from the rest of the beamline. For simplicity, these elements are not highlighted in the schematic drawing of the PKAT. Only the elements which are relevant for the time-resolved measurements of the intensity and polarization of the electron pulses are highlighted in color.

As the electron pulses go through the beamline, approximately three meters down the path, there is an *RF deflector cavity* operates in the TM_{110} mode (see Fig. 3.7), which transforms the longitudinal profile of the electron pulses into transverse. This transformation is a necessary step to investigate the temporal response of a photocathode. The detection of the transverse profile is achieved with the help of a *YAG* screen and a *CCD* camera or, alternatively, by using a *slit* and a *channeltron* to detect the current through the slit. The deflector cavity and the measuring methods will be further explained in this chapter.

Furthermore, in the PKAT laboratory system, the execution of time-resolved measurements of spin polarization of electrons is possible, through the use of a *Mott polarimeter*. For this purpose, after electron pulses go through the deflector

cavity and the slit, the transmitted fraction is guided through a second α-magnet and deflected vertically.

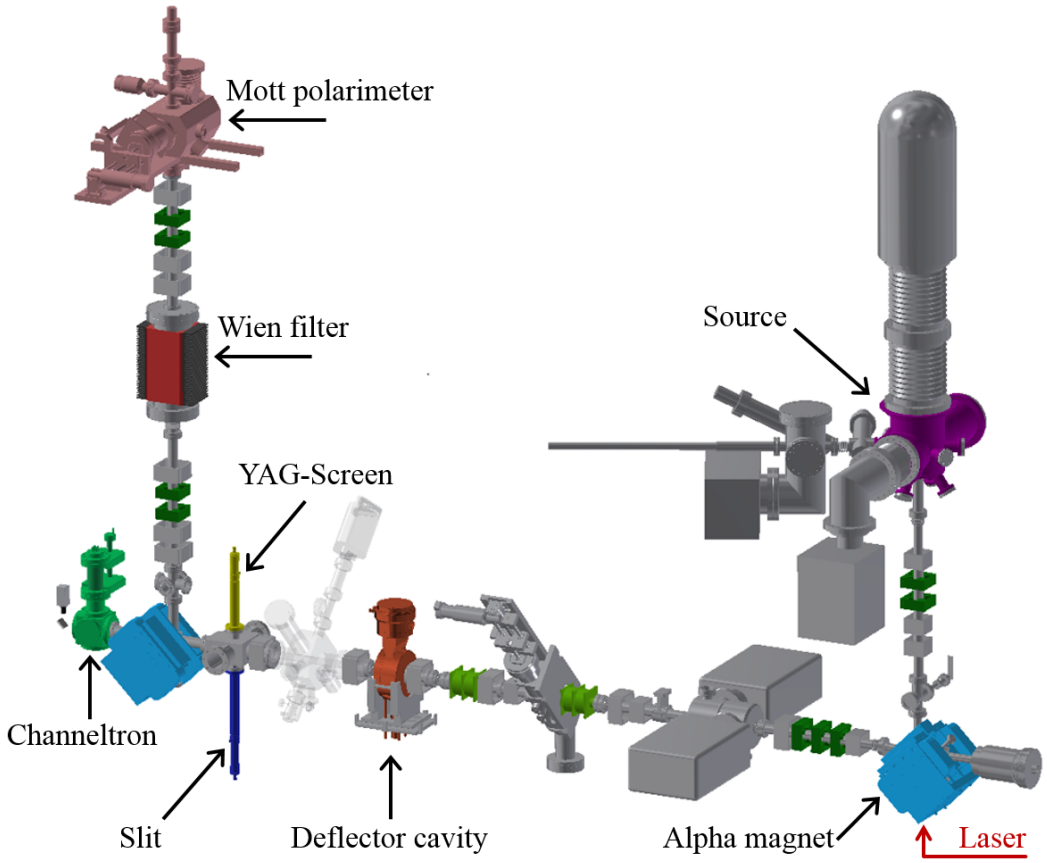

Figure 3.1: Overview of the schematic structure of PKAT. The elements which are relevant for the time response and time-resolved spin polarization measurements are highlighted in color. In addition, the quadrupoles and double solenoids for focusing the electron beam are shown. The femtosecond laser (shown with red arrow) illuminates the photocathode from below, and the generated electron pulses travel through the beamline. The lower insulator in the source chamber was removed due to the defect (see Fig. 3.3). The electric field was maintained at approximately the same value as in the initial design, see further explanations in Section 3.3.

In addition, since the Mott polarimeter requires the spin of the electrons to be perpendicular to the plane of scattering, electron beams must go through the *Wien filter* spin rotator system before entering the Mott. In the Mott, electrons are backscattered on a gold foil and detected with two detectors, each positioned at an angle of 120° to the direction of the beam. The principal operation of Wien filter and

Mott polarimeter are discussed later in this chapter. The principle of time-resolved spin polarization measurements are presented in Chapter 4.

In the following sections, each of the individual elements relevant for this project is explained in greater detail. First, however, a review of the status of the PKAT electron source is presented.

3.3 PKAT previous and present status

As mentioned earlier, the PKAT transport system was built over two decades ago and has been operating successfully. The flexibility of the PKAT apparatus has permitted different experiments to be adequately conducted with no restrictions to other experiments [18, 35, 133]. The initial design and construction of the PKAT allowed the electron source to operate at 100 keV, similar to the MAMI injector system [9, 50]. A close-up cross section of the PKAT electron source is illustrated in Fig. 3.2.

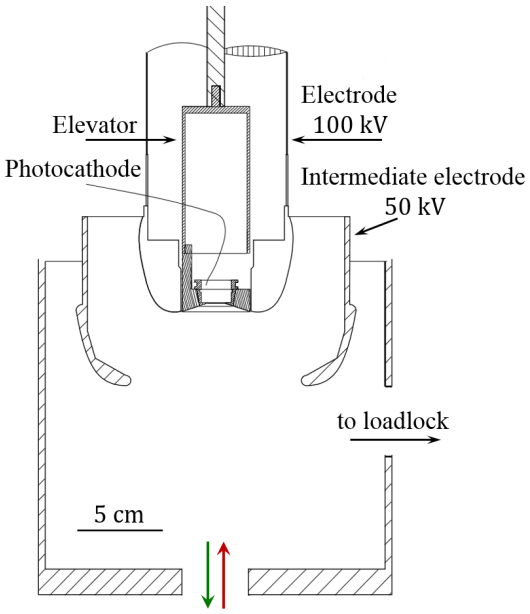

Figure 3.2: A cross section sketch of the PKAT electron gun. The elevator, which transports the photocathode to and from the preparation chamber (not shown here) and to the source, is shown. The main and intermediate electrodes and their respective electric potentials, as in the initial design, are also shown. The red and green arrows represent the directions of laser illumination and generated electron beam, respectively. Taken from [50].

In the initial design, the main electrode of the electron gun was set at −100 kV, the anode at 0 kV, and the intermediate electrode connected to a variable potential

between −38 kV and −62 kV. The generated electron pulses were accelerated to a kinetic energy of 100 keV ($v = 0.55\ c$).

In October 2016, at the early stages of this project, field emission starting at an energy of 77 keV was observed at the PKAT electron source. Many efforts were made to identify the cause of the field emission and to eliminate it. The elevator inside the source chamber was moved up and down in increments of 1 mm, and the voltage at which the field emission occurred was investigated, confirming that moving the elevator did not affect the voltage at which the field emission occurred. The first assumption was that the observed field emission was possibly due to impurities gathering around the anode and contaminating the source. Prior to the field emission incident, a K_2CsSb photocathode had been used for a few months for time response measurements [18]. Since K_2CsSb has a large layer of Cs on the top, excessive Cs in the source chamber was suspected as the cause of field emission.

Attempts were made to use Kr gas in the source chamber to create a discharge and eliminate the possible contamination. In a separate testing area, Kr gas was tested, and the voltage and current expectations for the discharge were obtained. The discharge was observed at 400 V and at a current of 0.5 mA.

The next step was to prepare the PKAT system to attach the Kr container to the source chamber. In the process, a leak was observed in the PKAT system. After identifying the source, the leak was fixed with vacuum sealer, and the NEG[3] material was activated at 450 °C. The hope was that during the leak the possible Cs contamination on the anode was oxidized and field emission no longer existed. Afterward, however, continued field emission was observed, although at a higher voltage of 96 kV. The higher field emission voltage was possibly due to oxidization of the Cs contamination around the anode.

The observed high pressure in the source chamber was related to the surface contaminants due to the leak at the earlier stage and could not be eradicated completely by pumping. Furthermore, since vacuum sealer spray had been used to stop the leak, the source chamber could not be baked out to higher temperatures.

The only solution to revive the operation of the source at 100 keV was dismantling the entire source chamber, replacing all the gaskets, and UHV-compatible cleaning of all the parts inside the source chamber. During the following six months, the source chamber was dismantled and thoroughly cleaned after more than 20 years of operation. A close-up photo of the PKAT source chamber prior to dismantling is shown in Fig 3.3.

In the process of dismantling, however, one of the high voltage ceramic insulators around the source chamber was damaged and rendered unusable. Given the yearlong process necessary for the acquisition of a new insulator, the decision was made to replace the defective ceramic insulator with a metal cylinder of the same dimensions and continue the measurements required for this project. In Fig. 3.3, the photo on the right shows the PKAT source chamber at present.

[3]Non Evaporable Getter pump

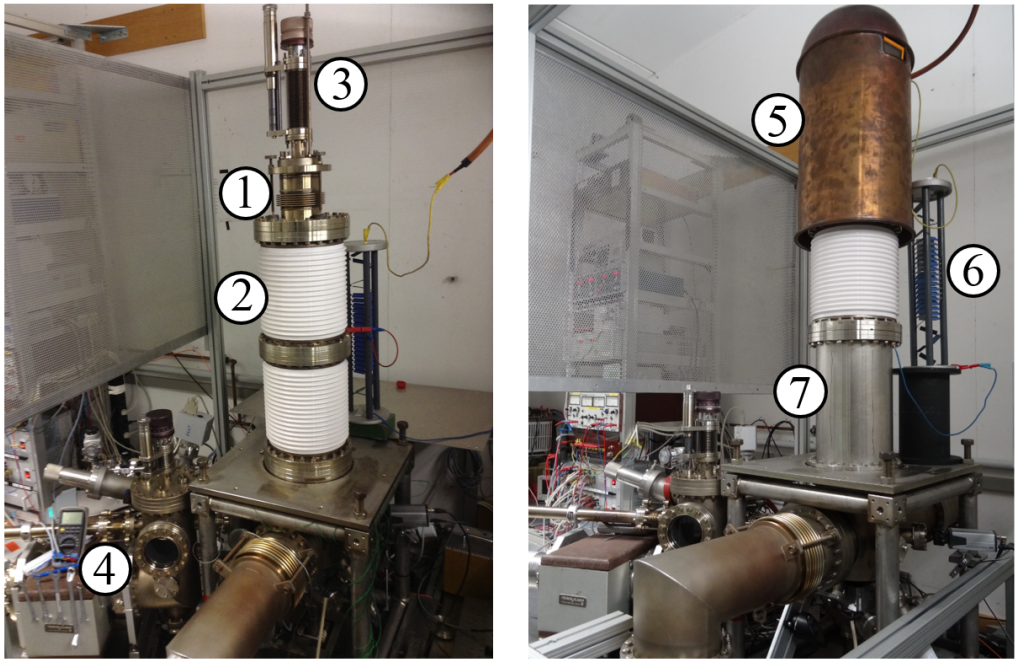

Figure 3.3: The PKAT source chamber. On the left, source chamber prior to dismantling due to the experienced leak. On the right, source chamber in the present condition, in which the measurements in this project were performed. The main parts in the photos are: ① the electron source, ② ceramic insulators, ③ the elevator, ④ the preparation chamber, ⑤ the copper shield around the source, ⑥ the variable potential, ⑦ the stainless steel tube in place of the damaged ceramic insulator.

The intermediate electrode (see Fig. 3.2) was kept and grounded (0 V potential). Keeping the intermediate electrode provided two advantages. First, the electric field strength could be maintained at a fairly similar field strength to the PKAT in the original design, approximately $1\,\mathrm{MV\,m^{-1}}$ at the crystal surface. Second, because the field conditions at the cathode are important for the initial trajectory of the electrons, this measure guaranteed the use of the electro-optical lenses without any changes to the arrangement.

Operating the PKAT electron source with only one insulator imposed many limitations and resulted in many challenges during the course of the measurements. From May through September of 2017, the highest energy the source was able to deliver without experiencing field emission was 30 keV. Finally, in September 2017, operations could be conducted at 45 keV. All the measurements presented in this thesis were performed with the PKAT electron source operating at 45 keV.

Working with such a low-energy electron beam presented many challenges, in part because the beam was not magnetically rigid and required a much longer time for optimization. To focus and guide the beam through the PKAT assembly was very

difficult. In addition, any small external field easily disturbed the beam; the electron beam was not stable throughout each measurement. During the measurements, the presence of other high-voltage power supplies or magnetic fields in the vicinity of the beamline, and even the operation of the MAMI accelerator system, were observed influencing the electron beam and causing disturbances. In Chapters 5 and 6 results of the measurements are presented and effects of the less energetic electron beam on the measurements, where applicable, are explained.

In the following sections, the measuring principles for time response measurements are discussed and the related elements are explained.

3.4 Time response measurements

Some of the primary tasks of this thesis were to investigate the pulse response and polarization of different photocathodes in a time-resolved manner. The charge distribution of electron pulses will shed light on the transport mechanisms inside photocathodes and demonstrate the quality of the photocathode material and its construction. Investigating the time dependency of the spin polarization of the electrons will help to better understand the motion of electrons inside the semiconductor.

In order to detect ultrashort electron pulses, two necessary conditions have to be attained. First, to generate electron pulses, one must illuminate the photocathode with a pulsed laser. Considering both the distance that the generated electron pulses must be transported before reaching the analyzing device and the apparative resolution limitations of the equipment between the source and the analyzing device, the use of a laser pulse whose pulse length is smaller than the pulse response of the cathode under investigation is necessary. The photocathodes studied in this project have pulse responses with FWHM in the range of a few picoseconds. In order to generate such ultra-short electron pulses in the PKAT laboratory, a femtosecond laser system was used.

The space-charge problems in the PKAT beam transport limit the bunch charge to approximately 0.1 fC [8]. This measurement corresponds to approximately 600 electrons in a bunch and therefore, makes conducting pulse response measurements with a single pulse impossible. This limitation leads to the second necessary condition, in order to perform time response measurements, the integration of many consecutive pulses is imperative. In doing so, laser pulses must be well synchronized with the RF signal of the deflector cavity.

3.4.1 Measuring principle

The principle of generating synchronized electron pulses and detecting them for time response measurements is schematically shown in Fig 3.4.

A femtosecond laser pulse generates electron pulses, which are synchronized with the RF of the deflector cavity. In the deflector cavity, the longitudinal profile of the electron pulses is transformed into a transverse profile. A phase shifter induces

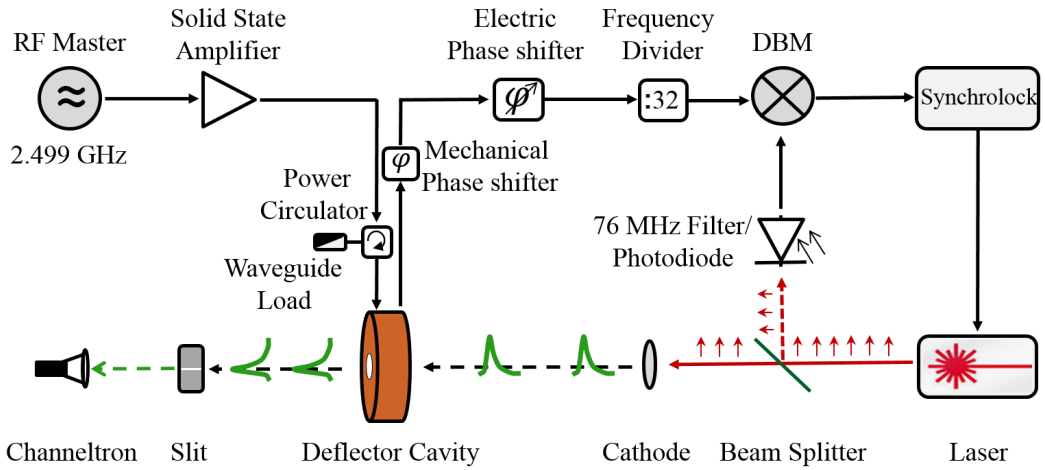

Figure 3.4: Schematic overview of the principle of time response measurements. A laser pulse synchronized with the RF of the cavity generates electron pulses. As electron pulses go through the deflector cavity, the longitudinal profile of the electron bunch is transferred into a transverse profile. The transverse profile can then be detected and analyzed either by *a*) slit and channeltron method: the profile of the electron pulse is scanned through a slit, current is amplified in a channeltron, and measured with a picoammeter or alternately, by *b*) screen method: profile of electron pulse is captured on a YAG screen and analyzed with a camera. For simplicity, the latter method is not shown in the figure.

a time delay in the electron pulses arrival at the deflector cavity, and thereby, the electrons are deflected differently in the transverse direction. Transversely deflected electrons can be detected and analyzed in two ways:

1. *Screen method*: The transverse profile of electrons is captured by a Ce:YAG screen[4], photographed with a CCD camera[5], and then analyzed.

2. *Slit method*: By changing the phase of a phase shifter, different parts of electron pulses are transmitted through a slit. The transmitted current is amplified by a channeltron and measured.

The complete discussion of these methods is given in Section 3.5.

3.4.2 Laser pulse system

The laser system[6] in the PKAT laboratory is a mode-lock ultrafast laser which uses a *Titanium:Sapphire* crystal as the laser gain medium and a 10 W pump laser[7]. The

[4]Cer-doped Yttrium Aluminum Garnet
[5]Charge-Coupled Device
[6]Coherent MIRA 900 with Synchro-Lock
[7]Coherent, Verdi G10

MIRA laser has the capacity to function in both DC mode and pulsed mode and can generate a laser beam of (0.8 ± 0.1) mm diameter at the output coupler [29]. The MIRA laser can be tuned to produce pulses in the wavelength range of 755 nm to 890 nm, with a pulse length of less than 150 fs and a repetition rate of 76 MHz.

In addition, laser pulses of 400 nm wavelength can be generated with the help of an *SHG* (Second Harmonic Generator)[8] frequency doubler. SHG was integrated into the PKAT laser system and has been used to measure time response of K_2CsSb [60] and bulk GaAs [35], but SHG was not relevant in the measurements of this work.

For the majority of the measurements performed in this project, the MIRA laser was operating at a set wavelength of 800 nm, except where the effects of various wavelengths was investigated, for example as in Section 6.5. A detailed description of the optical elements and modes of operation for the MIRA laser can be found in [107]. After the laser beam exits the MIRA, the laser beam is directed through various mirrors and prisms, and its intensity is controlled by several attenuators before illuminating the photocathode.

As previously mentioned, time response measurements require integrating many individual electron pulses which are well synchronized with the RF of the deflector cavity. In this project, in the case of the measurements with the slit, about 1×10^7 pulses are integrated. The process of achieving synchronization can be seen in Fig. 3.4, and a picture of synchronized pulses is shown in Fig. 3.5.

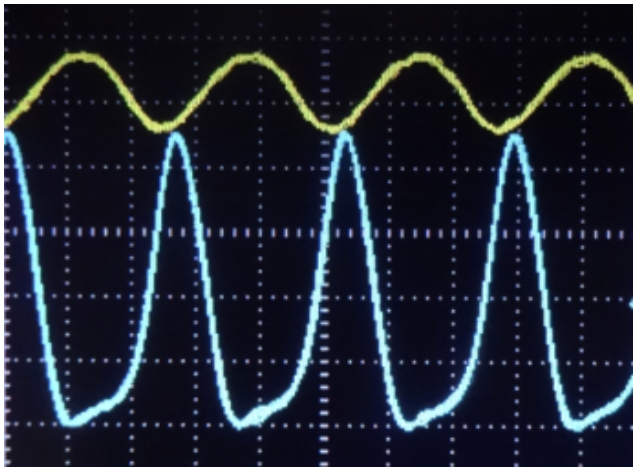

Figure 3.5: A photo of the oscilloscope showing the laser pulses (in blue) synchronized with the RF/32 of the deflector cavity in (yellow) prior to time response measurements. The timescale on the screen is 5 ns/division.

The deflector cavity is operated at a frequency of 2.449 GHz, which is the MAMI master oscillator. In order to satisfy the condition of synchronization between laser pulses generated by the MIRA at a repetition rate of 76 MHz and the frequency of

[8] APE, Harmonixx SHG

the deflector cavity, a double balanced mixer (DBM) and a synchro-lock unit[9] for MIRA 900 are used.

The DBM receives two signals: 1) A reference signal from the deflector cavity passes through the phase shifter and then into the frequency divider before entering the DBM. The frequency divider takes the 32^{nd} sub-harmonic pulse, which is equivalent to 76 MHz. 2) By means of a beam splitter, a fraction of the laser beam is sent into a photodiode. The generated electric current enters the DBM. These two signals are balanced out in the DBM, and the output goes to a synchro-lock unit in order to keep the phase relationship constant.

3.4.3 Phase shifter

To perform time-resolved measurements, in addition to having a pulsed laser, a deflector cavity, and a synchro-lock system, one must have a means of changing the phase relationship between the deflector cavity and the laser pulse without causing any interference to the synchro-lock unit. This change is accomplished by using a phase shifter. A phase shifter can delay the time of entry of electron pulses into the deflector cavity. This delay, in turn, causes the transverse profile of electrons to be shifted, allowing different parts of the electron pulse to be scanned and analyzed through the analyzing device.

Two phase shifters are used for this project. The main phase shifter is a *computer-controlled electro phase shifter*, which allows automatic control of voltage change in the range of 0–10 V in steps of 1 mV, corresponding to a phase shift range of 0–400°. The second phase shifter, used in conjunction with the electronic one, is a *mechanical phase shifter* and can operate in a range of 0–10 V as well. The electronic phase shifter, which is fast, robust, and more reliable, serves to control the phase and define the relative displacement of the beam on the pulse detecting system.

3.4.4 Deflector cavity

In accelerator systems, cavities are used to store and transfer electromagnetic energy to the particles under investigation. The most commonly used cavities are radio-frequency (RF) cavities.

In the PKAT beamline, a transverse deflector cavity is used as a diagnostic tool for characterization of the longitudinal properties of electron bunches. The cavity which is used to transform the longitudinal profile of the electron bunches into a transverse profile is a pillbox copper cavity and operated at the lowest dipole mode, a TM_{110}-like mode. A picture of the cylindrically symmetric deflector cavity used in the PKAT transport system is shown in Fig. 3.6.

Cylindrical cavities have degeneracy between the horizontal and vertical dipole modes. By making the cavity slightly asymmetric, through the use of coupling slots or parallel rods, the frequencies of these passbands can be separated. This

[9]Coherent Synchro-lock

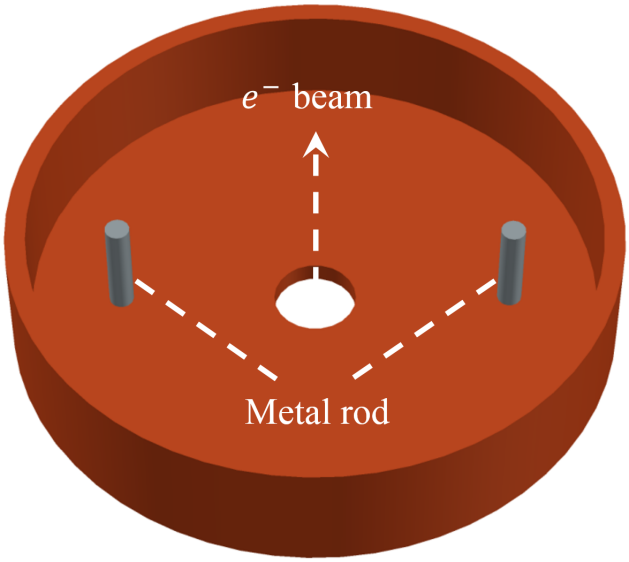

Figure 3.6: The deflector cavity used in PKAT is cylindrically symmetric and made from copper. The two metal rods are used for mode stabilization.

separation will set the two dipole modes in the cavity at 90° to each other. The two metal rods used for mode stabilization in the PKAT deflector cavity are shown in Fig. 3.6.

For a cavity operating at TM_{110}, no longitudinal electric field exists on the beam axis. Therefore, when a beam is injected into the cavity at the zero-crossing of the RF, due to the Lorenz force, the beam experiences only a transverse force from the magnetic field. In addition, since the slope of the RF is maximum at the zero-crossing, the magnetic field will exert a strong transverse kick on the electron beam. Furthermore, when the center of electron pulse passes the cavity at zero phase of the RF, the head and the tail of pulse are deflected in opposite directions, while the center of the electron pulse remains undeflected. As a result, the longitudinal profile of the bunch is transformed into a transverse profile. Fig. 3.7 depicts the electric and magnetic fields of the TM_{110} cavity used in the PKAT.

By changing the phase from the zero-crossing in small increments, a shift in transverse position of the beam on the profile monitor occurs at each step. This method can be exploited in electron bunch length diagnostic measurements, as seen in this thesis.

The deflection angle of electrons in MKS system is given by

$$\tan\alpha = 2.35 \times 10^{-4} \frac{\lambda_0}{\gamma} H \sin\frac{\pi h}{\beta\lambda_0} \tag{3.1}$$

where λ_0 is the vacuum wavelength at the resonance frequency, H denotes the magnetic field amplitude along the axis of the cavity, h is the length of the resonator, βc is the axial velocity, and $\gamma = 1/\sqrt{1-\beta^2}$ is the Lorentz factor.

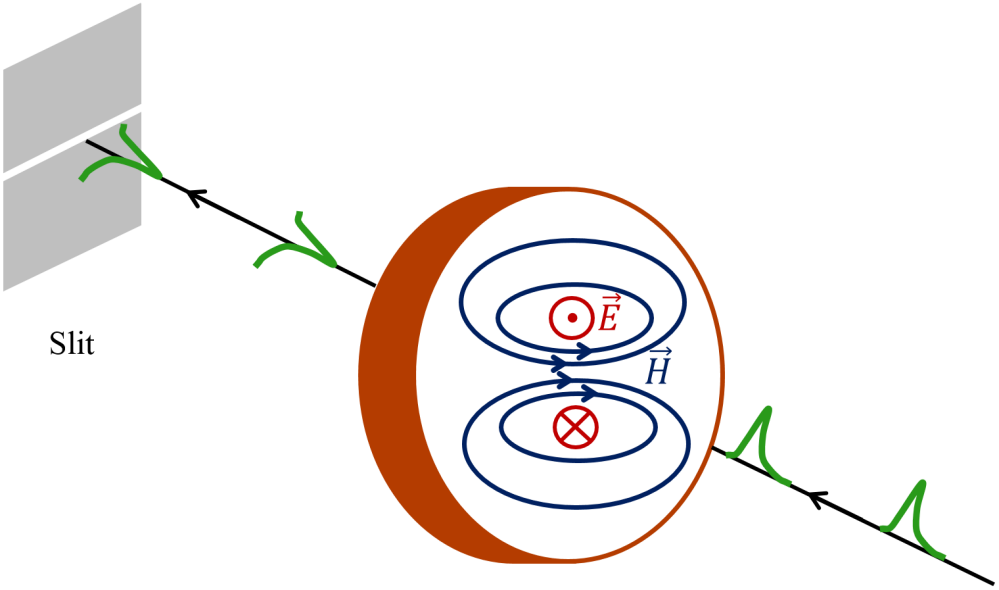

Figure 3.7: Electric and magnetic fields of a TM_{110} mode in the center of the cavity. As the beam travels through the cavity, the fields inside the cavity transform the longitudinal profile of the electron bunch into a transverse profile before the electron bunch reaches the detection area.

From the geometry drawn in Fig. 3.8, for a screen or slit positioned at a distance s from the cavity, one can write the equation for the deflection angle of α based on the deflection amplitude X in the transverse direction. According to Fig. 3.8,

$$\tan\alpha = \frac{X}{s + \frac{h}{2}}\,. \tag{3.2}$$

By equating Eq. 3.1 and 3.2, and using the surface resistivity for a copper cavity given by

$$R_s = \frac{4.52 \times 10^{-3}}{\sqrt{\lambda_0}} \quad \Omega, \tag{3.3}$$

the deflection amplitude is obtained by [49]

$$X = 44.3 \times 10^{-4} \left(\frac{s + \frac{h}{2}}{\gamma}\right) \left[\frac{P_{\text{cav}}\,\lambda_0^{\frac{1}{2}}}{0.61 + \frac{h}{\lambda_0}}\right]^{\frac{1}{2}} \sin\left(\frac{\pi h}{\beta\lambda_0}\right) \tag{3.4}$$

where P_{cav} is the power at which the cavity is operated, with a maximum value of 322 W. For the PKAT beam line, $h = 3.14$ cm and $s = 69$ cm. Operating at $P_{\text{cav}} = 322$ W, results in $X = 2.8$ cm, a deflection angle of $\alpha = 40.10$ mrad, and a deflection amplitude of 5.6 cm.

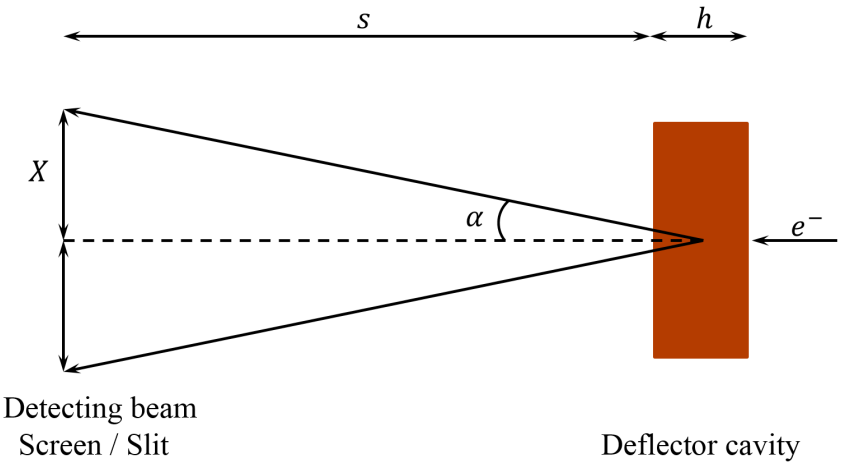

Figure 3.8: Simplified sketch of deflecting a beam through the deflector cavity. The value X represents half of the peak-to-peak deflection amplitude.

3.5 Electron pulse detection method

Two methods exist for detecting and analyzing the electron beam profile, the screen and camera method and the slit and channeltron method. From the time electrons are generated in the photocathode until they are detected, several factors contribute to the limitations of the time response investigations in the PKAT system. These limitations initiate from the apparative resolution of each element and transit time dispersion. The latter is a physical limitation of the photocathode itself.

Since the beam conditions at 45 keV considerably worsened when compared to the 100 keV, the time resolution was increased substantially. The time resolution of our measurements with the slit[10] is estimated at $\sigma \approx 1.37$ ps compared to $\sigma \approx 1.03$ ps under the optimum conditions [18]. Due to the unstable conditions, we estimate an uncertainty of at least 0.50 ps in the obtained time resolution in our measurements. The three main factors contributing to the poor resolution are the jitter of the RF phase, the transverse beam diameter, and the jitter of the position of the electron beam. The jitter of the RF phase initiates from the magnetic fields associated with the frequency fluctuations in the synchronized system. The jitter of the position of the electron beam is a result of the positional fluctuations of the electrons due to the external environment conditions. The details of the measure of the transverse beam diameter on the screen are presented in the next chapter. The factors contributing to the time resolution of the time response measurements are discussed in more details in [18].

The longer measuring time required for beam conditions at 45 keV results in poorer resolution for the asymmetry measurements, especially for the data points

[10] For the screen measurements, the time resolution has increased from $\sigma \approx 0.83$ ps under optimum conditions [18] to $\sigma \approx 1.10$ ps.

at higher phase shift values, see Section 5.9. In the following sections, the two detection methods are discussed.

3.5.1 YAG screen and CCD camera

In this method, the electron pulse impinges on a 100 µm thick screen and then is imaged with a CCD camera[11]. The screen is a single-crystal *Yttrium Aluminum Garnet* activated with *Cerium*, YAG[12], a yellowish and translucent crystal with the chemical formula $Y_3Al_2O_{12}$.

YAG:Ce exhibits specific physical and chemical properties which makes it a practical scintilator. YAG:Ce offers a photon yield of 35 /e/keV with maximum emission at a wavelength of 550 nm and a decay time of 70 ns, after which the number of excited light-emitting centers decreases by a factor of e [31]. YAG screens emit light by scintillation after collision with the electron beam. Next, an optical system directs the light to the CCD camera, where the image is collected and analyzed. After a single electron hits the YAG screen, the number of photons that arrive at the CCD camera is given by

$$N = \frac{1}{4\pi} Y \cdot \Omega \cdot E \tag{3.5}$$

where Y is the YAG photon yield, $Y = 35$ /e/keV, Ω denotes the solid angle covered by the optical system, and E is the energy of the electrons. Referring to Fig. 3.9, the solid angle Ω can be calculated using the diameter of the YAG screen, 23 mm, the distance between the screen and the camera, 69 cm, and the angle θ.

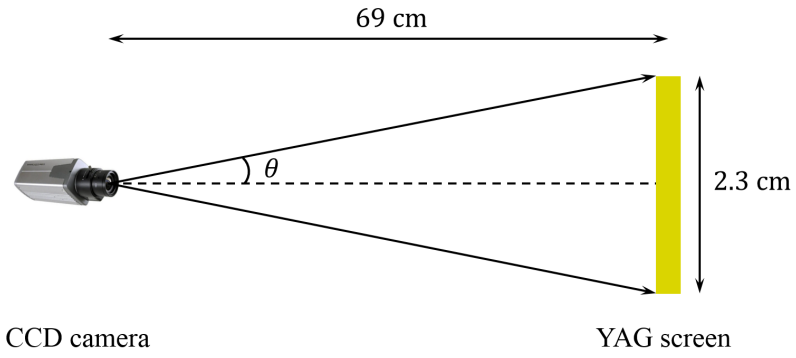

Figure 3.9: As the electron beam collides with the 8 µm YAG:Ce screen, the beam produces photons which will be detected by the CCD camera at a distance of 69 cm. The dimensions in the sketch are not to scale.

$$\Omega = 2\pi\,(1 - \cos\theta) = 8.72 \times 10^{-4}\,\mathrm{sr} \tag{3.6}$$

[11] VC4067 Professional, Vision Components GmbH, Ettlingen
[12] Manufacturer: Crytur, http://www.crytur.cz/

Assuming 100 % efficiency along the optical system, a single electron at 45 keV produces about 0.1 photons that will arrive at the CCD sensor. For a typical camera exposure time of 1 ms and a current of 1 nA, about 10^6 photons reach the CCD camera.

The investigation of the electron penetration depth in the YAG screen for different beam energies indicates that a 100 keV electron beam penetrates to a depth of approximately 33 µm into the YAG screen, where photons are produced [5]. Using the information provided for the electron penetration depth as the beam energy changes, one can draw the conclusion that the 45 keV electrons of the PKAT are completely absorbed at a depth of around 8 µm. Within this depth electrons will be scattered before complete absorption.

The CCD camera uses a thin silicon wafer chip, and its operation principle is based on the internal photoelectric effect. The chip consists of 1280×1240 pixels, with a pixel size of $6.45\,\mu m \times 6.45\,\mu m$. Each pixel is surrounded by a non-conductive boundary; therefore, the charge collected during exposure remains within the pixel. The bit depth of the chip is 8, which means the maximum dynamic range of the sensor is 255. This range is the highest dynamic range that the camera is capable of reproducing, if all other constraints are eliminated. However, in reality, the dynamic range is much less due to background noise and in this study is approximately 2 bits. Therefore, the dynamic range is actually about 100 : 1. The camera has an internal shutter, which allows an exposure time range between 5 µs to 17 s.

The lens which is used with the CCD camera has a fixed focal length of 85 mm and an aperture which corresponds to 2.8. The optical limitations of the lens, such as the effects of aberrations and shallow depth of field, are discussed in [35] and are found to be negligible for electron pulse temporal measurements.

3.5.2 Slit and Channeltron

In this method, portions of the electron pulse will go selectively, first, through a slit[13]. Then, at a distance of about 69 cm past the slit, electrons will enter a *Channel Electron Multiplier*, CEM[14]. The inner surface of the CEM tube is manufactured from a specialty lead silicate glass, which is suitably processed to yield an efficient secondary emitting layer. When the inner surface is struck by an electron, secondary electrons are generated. By applying a voltage to the channeltron, these secondary electrons travel down the CEM channel. Eventually, these secondary electrons will strike the emissive surface again, in turn causing the release of subsequent electrons. The high voltage power supply[15], which can be controlled remotely, delivers voltages in the range of $1.1 - 2.1$ kV. At the output end of the multiplier, these electrons are collected and fed into a picoammeter[16].

[13] Manufactured by the Laser Job company
[14] Detectors Technology Inc., Model 2403
[15] LeCroy High Voltage Module, Model 1461
[16] Keithley Instruments Inc, Model 6485

The channeltron is capable of reaching a gain of 5×10^7 at an operating voltage of 2.05 kV in a rise time of $3 - 5$ ns. The CEM operates at a typical bias current of 21 µA, and can produce a maximum output current of 10 % of the bias current, 2.1 µA[17]. The amplification of the channeltron used in PKAT was measured in [60]. Operating at a voltage of 1.950 kV, which is the voltage used during this thesis, the CEM was found to deliver a gain of 2×10^3. This huge drop in the gain of the CEM can be attributed to the aging of the CEM and to the electron depletion and ion contamination, as the manufacturing company suggests.

The picoammeter is equipped with high speed auto ranging with top speeds of 1000 readings per second and can measure small currents with high accuracy. The picoammeter is capable of measuring currents in the range of 10 fA to 21 mA in eight available ranges. In addition, the picoammeter has a feature which maintains stability and accuracy over time and through changes in temperature [58].

3.6 Pockels cell

As discussed in the previous chapter, one of the essential requirements to perform spin polarization measurements is a circularly polarized laser beam. This requirement is met with the help of a Pockels cell and a polarizer. A Pockels cell, based on the *Pockels effect* discovered in 1893 by *Friedrich Carl Alwin Pockels*, is an optical device consisting of an electro-optic crystal with two electrodes attached to it. The placement of the electrodes on the crystal, and therefore the orientation of the electric field inside the crystal, determines whether the Pockels cell is transverse or longitudinal.

In this experiment the longitudinal configuration is used, and a sketch of the Pockels cell is illustrated in Fig. 3.10. The electrodes are located on the two ends of the crystal, which the laser beam passes through, creating an electric field which is parallel to the propagation of the laser. When a voltage is applied, and the laser is transmitted through the crystal, the crystal induces birefringence, Δn, which is proportional to the applied voltage.

$$\Delta n = r_{ij} E \, n_0^3 \tag{3.7}$$

where r_{ij} is the electro-optic coefficient for the specific crystal, E is the electric field experienced by the crystal due to the applied voltage, and n_0 is the ordinary refractive index. By applying a constant voltage, the Pockels cell operates as a voltage-controlled waveplate, a device which changes the polarization direction of the incident laser beam. In the absence of an external electric field, no phase retardation occurs, and Pockels cell will transmit the light with no change in the polarization state.

[17] Detector Tech

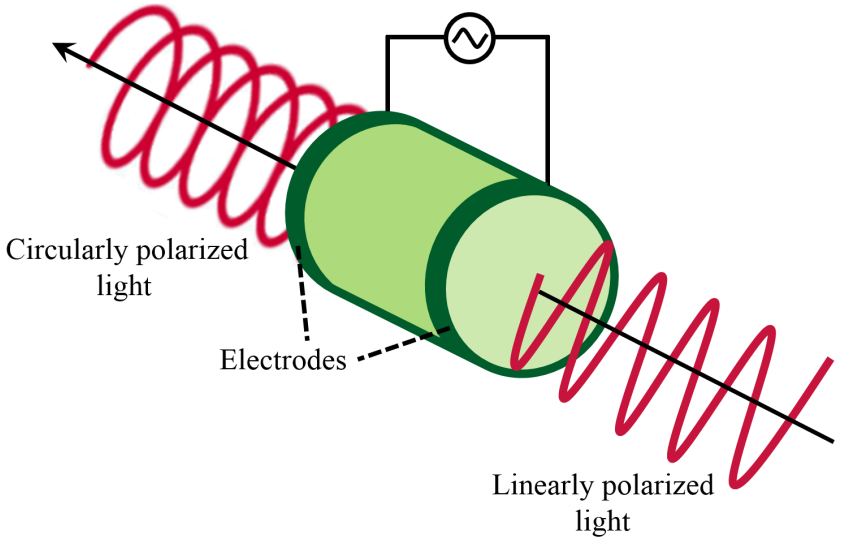

Figure 3.10: As linearly polarized light travels through the Pockels cell, the light will be transformed to circularly polarized light. In a longitudinal Pockels cell, electrodes are located on the two ends of the crystal.

In a waveplate, the relative phase retardation between the two polarization components of the laser beam is given by

$$\Gamma = \frac{2\pi \Delta n L}{\lambda} \tag{3.8}$$

where L is the thickness of the crystal and λ denotes the wavelength of the excitation laser. Inserting Eq. 3.7 in Eq. 3.8 and using the equality of $E = V/L$ for the longitudinal configuration, where V is the applied voltage, one obtains

$$\Gamma = \frac{2\pi\, r_{ij} V n_0^3}{\lambda}\,. \tag{3.9}$$

With careful design and orientation, the phase shift between the polarization components is $\pi/2$. This arrangement is called a quarter-waveplate and will result in

$$V = \frac{\lambda}{4\, r_{ij}\, n_0^3}\,. \tag{3.10}$$

When linearly polarized light passes through a quarter-waveplate such that the axis of polarization makes a 45° angle with the fast and slow axes of the waveplate, the emitted wave will become circularly polarized.

The Pockels cell provides switching of the polarization of the laser in the order of nanoseconds [125], an essential requirement in conducting asymmetry measurements. The Pockels cell used in the PKAT system[18] is made with a KD*P, Potassium di-deuterium phosphate (KD_2PO_4) crystal, referred to as DKDP. This type of

[18] Gsänger Optoelektonik GmbH

crystal demonstrates high optical quality and can be used at wavelengths ranging from 400 nm to about 1.1 µm [125]. The electro-optic coefficient for KD*P crystal is r_{63} with the value of $r_{63} = 25\,\mathrm{pm\,V^{-1}}$.

3.7 Wien filter

The polarized electron source in PKAT produces a longitudinally polarized electron beam. However, one of the important prerequisites when making asymmetry measurements using a Mott polarimeter is polarized electrons with a spin transverse to the scattering plane. The spin rotator which was used in prior years in the PKAT system, toroidal condenser [116], could not be installed due to space limitations. For this purpose, a Wien filter spin rotator was commissioned for this project and was built in house. The Wien filter is a replica of one used in MAMI for many years and is dedicated to parity-violating asymmetry measurements and other measurements which require a frequent change of spin orientation at the target, from parallel to perpendicular to the direction of the electron travel path [68, 69].

3.7.1 Electron-optical principle

The Wien filter is a compact spin rotator system with a length of 445 mm. It consists of homogeneous electric and magnetic fields which are perpendicular to each other and transverse to the direction of the electron travel. A cross section of the Wien filter is illustrated in Fig. 3.11.

The stainless-steel electrode plates are designed with contoured edges to ensure the condition of no deflection (see Equation 3.11) is fulfilled in the fringes as well. Otherwise, it leads to large additional deflections of the electron beam by the fringes. Applying high voltage to the electrode plates produces a vertical homogeneous electric field, while a constant current going through the symmetric window-frame coils surrounded by a magnetic yoke results in a homogeneous horizontal magnetic field. Additional metal plates at the two ends are used to reinforce the shielding against fringe field effects.

In the following, a perfect homogeneous distribution of the electric and the magnetic field everywhere inside the Wien filter is assumed. The objective is to choose electric and magnetic field forces so that the electron beam is not deflected from the reference trajectory beam as electrons with velocity $\vec{v}$ travel through the Wien filter while the spin rotates. The state of no deflection is fulfilled if the exerted electric and magnetic fields follow the Lorentz force equilibrium condition of

$$\vec{E} + \vec{v} \times \vec{B} = 0 \quad \therefore \quad \left|\frac{E}{B}\right| = |v| \tag{3.11}$$

The precession of the spin vector of the electron, $\vec{S}$, which is due to the interaction of the magnetic field with the magnetic moment associated with spin, is described by the Thomas [126], Bargmann, Michael and Telegdi (BMT) [13, 64] equation.

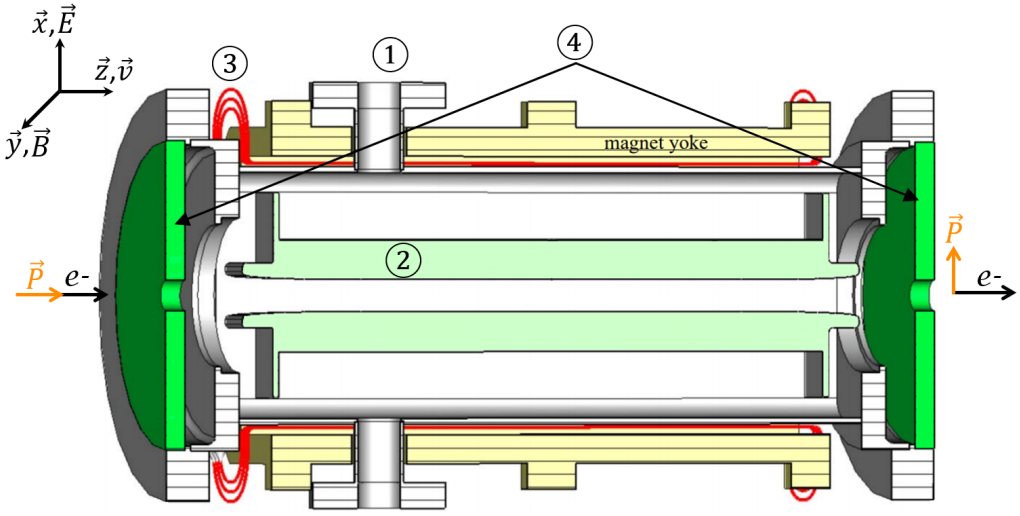

Figure 3.11: Cross section of the Wien filter. The main components are: ①: High voltage feedthrough, ②: Electrode plates, ③: Magnetic coils, ④: Magnet mirror plate. Magnet yokes to support the magnetic coils are also shown. By correctly selecting the directions and the magnitudes of the electric and magnetic fields, the polarization of the electrons (shown in orange arrows) can be rotated by 90° as shown. Modified from [118].

For an electron traveling with velocity $\vec{v}$ in an static electromagnetic field, the spin equation of motion can be written as

$$\frac{\mathrm{d}\vec{S}}{\mathrm{d}t} = \frac{e}{\gamma m_0}\vec{S} \times \left[(1+\gamma G)\,\vec{B}_\perp + (1+G)\,\vec{B}_\parallel + \gamma\left(G + \frac{1}{\gamma+1}\right)\frac{\vec{E}\times\vec{v}}{c^2}\right] \tag{3.12}$$

where G is the electron anomalous gyromagnetic moment related to the *electron gyromagnetic factor* with the relationship $G = \frac{1}{2}(g-2)$ and $g = 2.002319$. $\vec{B}_\perp$ and $\vec{B}_\parallel$ are the transverse and longitudinal components of the magnetic field in the laboratory frame, E is the electric field, and γ is the *Lorentz factor* defined as $\gamma = 1/\sqrt{1-\beta^2}$, where $\beta = v/c$ with v and c velocity of electron and the speed of light, respectively.

As the electron travels through the Wien filter, the magnetic field along the direction of travel is $\vec{B}_\parallel = 0$. Applying the condition of no deflection, Eq. 3.12 becomes

$$\frac{\mathrm{d}\vec{S}}{\mathrm{d}t} = \frac{e}{\gamma m_0}\vec{S} \times \left[(1+\gamma G)\,\vec{B}_\perp - \gamma\left(G + \frac{1}{\gamma+1}\right)\beta^2\vec{B}_\perp\right]. \tag{3.13}$$

The factor γG is negligible at 45 keV, and substituting β^2 in terms of γ, Eq. 3.13 can be simplified to

$$\frac{\mathrm{d}\vec{S}}{\mathrm{d}t} = \frac{eB_\perp}{\gamma m_0}\vec{S}\left[1 - \frac{\gamma}{\gamma+1}\cdot\frac{\gamma^2-1}{\gamma^2}\right] \tag{3.14}$$

Note that Eq. 3.14 has the form of a spin precession equation

$$\frac{\mathrm{d}\vec{S}}{\mathrm{d}t} = \vec{\omega}_{\mathrm{spin}} \times \vec{S} \tag{3.15}$$

where

$$\omega_{\mathrm{spin}} = \frac{eB_\perp}{\gamma^2 m_0} \tag{3.16}$$

is the angular velocity of the spin rotation.

Adopting the relationship $\omega = v/r$, where $r = L/\theta$ and L and θ denote the length of the Wien filter and the angle of the spin rotation, results in

$$\omega = \frac{\beta\, c\, \theta}{L}. \tag{3.17}$$

Equating Eq. 3.16 and 3.17 will yield

$$B = \frac{m_0\, \beta\, c\, \gamma^2\, \theta}{e\, L} \tag{3.18}$$

where, for simplicity, the subscript $\perp$ is dropped since the applied magnetic field is orthogonal.

For a given magnetic field strength and the associated electric field, as electrons fly through the Wien filter, one can obtain the angle of spin rotation

$$\theta = \frac{e\, L\, B}{m_0\, \beta\, c\, \gamma^2}. \tag{3.19}$$

As noted previously, in these calculations an identical effective length of the electric and magnetic field inside the Wien filter has been explicitly assumed. However, in practice, the perfect fields at the edges can hardly be realized; therefore, the relation between the field strengths for the no-deflection condition is not fulfilled [102, 128].

In an investigation with a similar Wien filter [128], the specific design of the filter resulted in the electrical field fringes having a shorter extension compared to the magnetic fringes. As a result, the focusing properties of the device were changed, which created a distortion to the horizontal beam trajectory. Therefore, some modifications were necessary. As the electrons pass through the two edges of the Wien filter, the imperfect cancellation of the forces in the extended fringe-field region causes electrons to experience a parallel offset from the central trajectory.

In [102], assuming that the effective lengths of both fields are equal, and therefore, an angular deflection is not present, an expression for this offset is given. In this study, the effective length of the Wien filter is considered 320 mm, and an offset in the order of $1 - 2$ mm is predicted [128].

3.7.2 Electron-optical properties of the Wien filter

In [89], Penner describes the optical properties of electrons for different magnetic deflection systems using a matrix method. The matrix method can be applied to particle trajectories of small spatial, angular, and energy spreads. In applying this method for the Wien filter, the following assumptions are made. First, the end fringe-field regions are assumed to be small compared to the length of the Wien filter. Second is the assumption that electrons are moving along the z-axis and that the electric and the magnetic fields are directed along the x and y axes respectively. Under no-deflection condition for electrons, the first-order approximation of the transformation matrix for the horizontal motion can be expressed by

$$T = \begin{pmatrix} \cos(L/R) & R\sin(L/R) & -R(1-\cos(L/R)) \\ -R^{-1}\sin(L/R) & \cos(L/R) & -\sin(L/R) \\ 0 & 0 & 1 \end{pmatrix} \tag{3.20}$$

where $R = \gamma m_0 v/eB$, and L is the field effective length. Using the equality of 3.18, R can be simplified to $R = L/\gamma\theta$.

In principle, by using a Wien filter achievement of spin rotation for an angular range of $-\frac{\pi}{2}$ to $+\frac{\pi}{2}$ is possible. The negative values of spin rotation are readily attained by reversing the field orientations. Moreover, since the spin orientation may be reversed through switching the helicity of the laser by using a Pockels cell [11], practically any desired spin orientation in the plane of the accelerator can be achieved.

In closing, one must note that the Wien filter is astigmatic and does not provide the same focusing properties for every spin rotation angle. While no focusing action by the Wien filter occurs in the vertical direction, and therefore, the corresponding matrix is a drift space, the horizontal matrix is identical to a quadrupole with varying focusing strength. For a similar Wien filter used in MAMI, a focusing variation of $0 - 5.5\,\mathrm{m}^{-1}$ for the spin rotation between 0 and $\frac{\pi}{2}$ was obtained [128]. However, in principle, mitigation of this focusing variation is possible by using additional quadrupoles before and after the Wien filter [129].

3.8 Mott polarimeter

Beams of polarized electrons are essential in many investigations, such as spin-dependent effects in atomic collisions [14, 59], parity violation in high energy nuclear scattering [95], and surface magnetic properties of solids [3, 63]. Electron spin analyses are commonly accomplished by using a Mott polarimeter. Mott polarimeters have the advantage of operating with an unpolarized target compared to Moller or Compton polarimeters, which use spin polarized targets. Moreover, they offer good efficiencies and are fairly simple to implement.

3.8.1 Principle of Mott polarimeter

Mott polarimeters exploit the left-right scattering asymmetry resulting from the *spin-orbit coupling* as the high-energy electrons interact with the *Coulomb potential* of a heavy nucleus. The measured scattering probability depends upon whether the electron spin and its orbital angular momentum are parallel or anti-parallel. In the rest frame of the electron, the electron near the target nucleus experiences a magnetic field, which interacts with its spin and induces a torque in the scattering potential.

The spin-dependent part of the Hamiltonian of an electron experiencing spin-orbit interaction is given by

$$H = \frac{Z\,e^2}{2m^2\,c^2\,r^3}\vec{L}\cdot\vec{S} \tag{3.21}$$

where $\vec{L}$ and $\vec{S}$ are the electron orbital and spin angular momentum, Z is the nucleus atomic number, r is the distance between the electron and the nucleus, e and m are electron charge and mass, and c is the speed of light. The scattering cross section, $\sigma(\theta)$, in the presence of the spin-orbit potential can be written as

$$\sigma(\theta) = \sigma_0(\theta)\left[1 + S(\theta)\,\vec{P}\cdot\hat{\mathrm{n}}\right] \tag{3.22}$$

where $\sigma_0(\theta)$ denotes the scattering cross section of the unpolarized electrons at an angle θ, $S(\theta)$ is the asymmetry function known as *Sherman function* or the polarimeter *analyzing power*, $\vec{P}$ is the electron beam polarization, and $\hat{\mathrm{n}}$ is the unit vector normal to the scattering plane. If $\vec{k}$ and $\vec{k}\,'$ represent the wave vectors associated with the incident and the scattered electron beam respectively, then

$$\hat{\mathrm{n}} \equiv \frac{\vec{k}\times\vec{k}\,'}{\left|\vec{k}\times\vec{k}\,'\right|}\,. \tag{3.23}$$

Factors, such as the energy of the electron beam, atomic number of the target, and the scattering transverse polarization angle of the electrons, affect the value of the measured asymmetry. The polarization can be obtained from the asymmetry if the Sherman function is known. Fig. 3.12 displays the angular dependence of the theoretical Sherman function for scattering on gold nuclei.

Since the orbital angular momentum, $\vec{L}$, is perpendicular to the scattering plane, the asymmetry is largest when the polarization is transverse to the scattering plane and thus transverse to the direction of the beam. For this reason, a spin rotator is required in the beamline to rotate the spin of electrons from longitudinal to transverse before entering the Mott. The spin rotation in the PKAT beamline is achieved with the Wien filter, which was discussed earlier in this chapter.

A thin gold target is eminently suitable in a Mott polarimeter. A high atomic number of $Z = 79$ ensures higher asymmetry values due to the larger spin-orbit coupling, see Eq. 3.21. Furthermore, gold has the advantage of chemical inertness

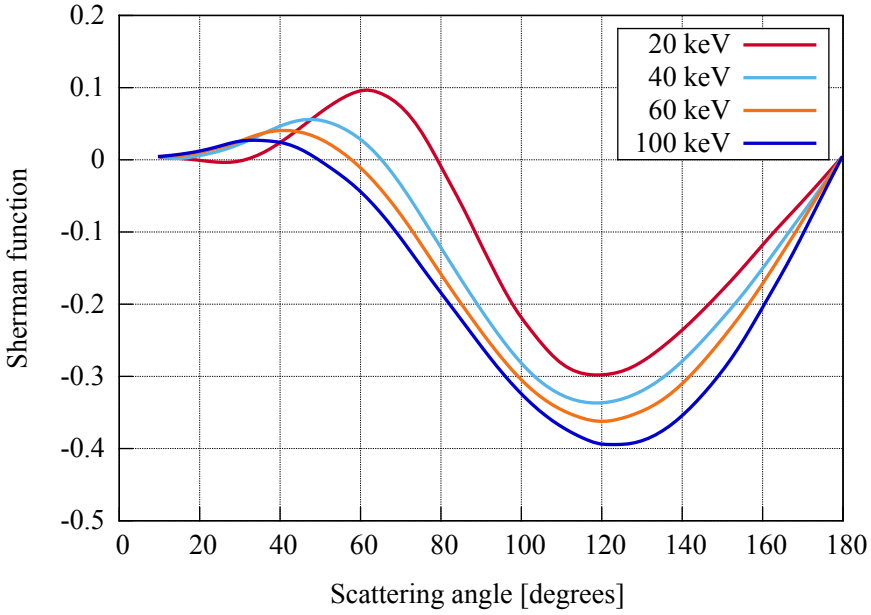

Figure 3.12: The angular dependence of the theoretical Sherman function for different beam energies of 20 keV, 40 keV, 60 keV, and 100 keV. The Sherman function has a broad maximum at $\theta = 120°$, and its value strongly increases with increasing beam energy. Reproduced from [120].

as the formation of oxides reduces the asymmetry. Additionally, gold can easily be fabricated into very thin foils, which is an essential requirement in reducing multiple scattering.

In order to diminish the systematic effects associated with small changes in the beam intensity during the measurements, the Mott polarimeter utilizes two identical detectors positioned at the azimuthal angle at which the scattering cross section is optimal. For low-beam-energy experiments, such as the one in the PKAT, silicon diode detectors are a good choice, as they discriminate against the background electrons [43, 110]. The detectors are positioned to detect the electrons scattered at $\theta = 120°$, where the Sherman function has a broad maximum, as can be seen in Fig. 3.12.

To reduce the systematic errors as a result of the unwanted backscattered electrons, the Mott chamber and other internal parts are made from Aluminum. The details of the construction of the PKAT Mott polarimeter has been discussed elsewhere [50]. Fig. 3.13 illustrates how the polarization is measured in the Mott polarimeter.

As the polarized electron beam impinges on the target, the helicity of the electron polarization at each given time determines the tendency for the electrons to scatter to each of the two detectors. If the Sherman function $S(\theta)$ is known, one can obtain

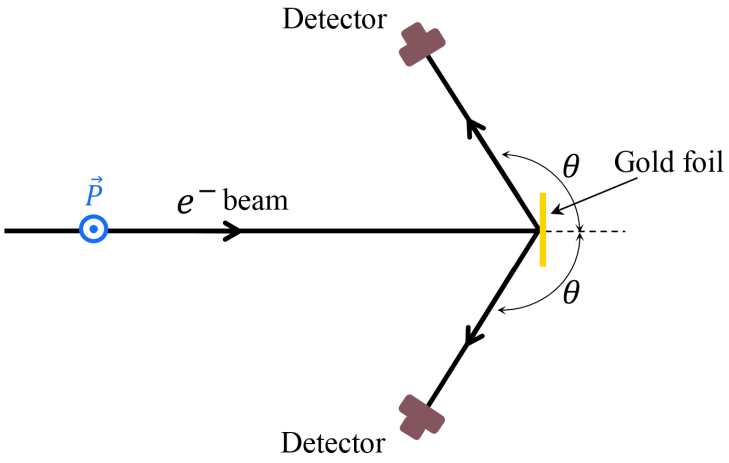

Figure 3.13: The interaction of the electrons with the heavy gold nucleus creates an asymmetry in the azimuthal scattering plane where the two Mott detectors are located. To achieve the maximum asymmetry, the polarization, shown in blue,must be perpendicular to the scattering plane.

the polarization by measuring the asymmetry between the count rates of the two detectors [59].

Let the L and R denote the detectors on the left and the right. Then, for each helicity, the expected count rates are L_+, R_+, and L_-, R_- respectively, where $\pm$ represent the helicity of the laser. Allow a and b to be the proportionality constants due to the detectors unequal solid angles, and I^+ and I^- represent the current fluctuations due to switching the helicity, by using Eq. 3.22 one can obtain the sets of equations for the count rates

$$\begin{aligned} L_+ &= I^+ a\,(1 + PS\,(\theta)) \quad \text{and} \quad R_+ = I^+ b\,(1 - PS\,(\theta)) \iff \text{positive helicity} \\ L_- &= I^- a\,(1 - PS\,(\theta)) \quad \text{and} \quad R_- = I^- b\,(1 + PS\,(\theta)) \iff \text{negative helicity} \end{aligned}$$

These equations will lead to

$$\frac{L_+}{L_-} = \frac{I^+}{I^-} \cdot \frac{1 + PS\,(\theta)}{1 - PS\,(\theta)} \qquad \text{and} \qquad \frac{R_-}{R_+} = \frac{I^-}{I^+} \cdot \frac{1 + PS\,(\theta)}{1 - PS\,(\theta)}. \tag{3.24}$$

Multiplying the two last equations and applying some algebra, and replacing the theoretical value of the Sherman function, $S(\theta)$, calculated based on scattering from a single free atom in target with the *effective Sherman function* of the target, $S_{\text{eff}}\,(\theta)$, will result in

$$A = PS_{\text{eff}}\,(\theta) \qquad \text{with} \qquad A = \frac{N^+ - N^-}{N^+ + N^-} \tag{3.25}$$

where $N^+ \equiv \sqrt{R_+ L_-}$ and $N^- \equiv \sqrt{R_- L_+}$. Introducing $Q \equiv R_- L_+ / R_+ L_-$, the asymmetry can be written as

$$A = \frac{1 - \sqrt{Q}}{1 + \sqrt{Q}} \tag{3.26}$$

One should note that asymmetry in the form of Eq. 3.26 eliminates the helicity-dependent current fluctuation asymmetry, in addition to the asymmetry associated with the different efficiency of the detectors. When using two detectors to measure the asymmetry, the additional information gained by using two detectors under helicity switching helps the asymmetry to self-normalize with respect to fluctuations of the beam current.

The effective Sherman function, which is the most important characteristic of the Mott polarimeter, depends on factors such as the thickness and the composition of the target, the scattering angle, and the beam energy. Large values of $S_{\text{eff}}(\theta)$ are desirable in order to obtain substantial asymmetry between the two detectors. However, since the cross section and, therefore, the measured intensity, I, are small at the angles where Sherman function is large [59], one must find a compromise between high asymmetry and high intensity. The best practice is to choose the parameters in such a way that the figure of merit (FOM) is maximal. In Mott polarimetry the FOM is defined as

$$FOM = \frac{I}{I_0} S_{\text{eff}}^2 \tag{3.27}$$

where $\frac{I}{I_0}$ is the ratio between the scattered and the primary current used in Mott measurements. For the measurements in this work, with the count rate in the order of kHz and a typical primary current of 1 nA, the figure of merit is in the order of $FOM \approx 10^{-5}$. In practice, one can make the ratio bigger by increasing the solid angle of the detectors. In order to optimize FOM a complex interplay between the solid angle, energy dependency of S_{eff}, and foil thickness effects is required.

The thickness of the target plays an important role in the measured asymmetry. The effect of the target thickness and various electron energy resolutions on asymmetry for different beam energies have been investigated [44, 131]. The results for a beam energy of 20 keV is illustrated in Fig. 3.14 [44]. The research as outlined in [44], showed that for all beam energy values with an energy resolution of 4 eV, the asymmetry decreases with increasing foil thickness. However, the rate at which the asymmetry decreases is larger as the beam energy decreases, especially at thicknesses below 200 Å. More importantly, however, is the effect of the energy resolution on the asymmetry values. The energy resolution of the asymmetry measurements in this project is approximately 10 keV. Therefore, the drop of the asymmetry values will be much more dramatic than what is shown in Fig. 3.14.

The Sherman function is very sensitive to the thickness of the target, which is why S_{eff} must be used instead of S_{th}. Every target contains a great number of atoms, and the multiple scattering processes cause substantial deviations from the S_{th} of the ideal single atom scattering.

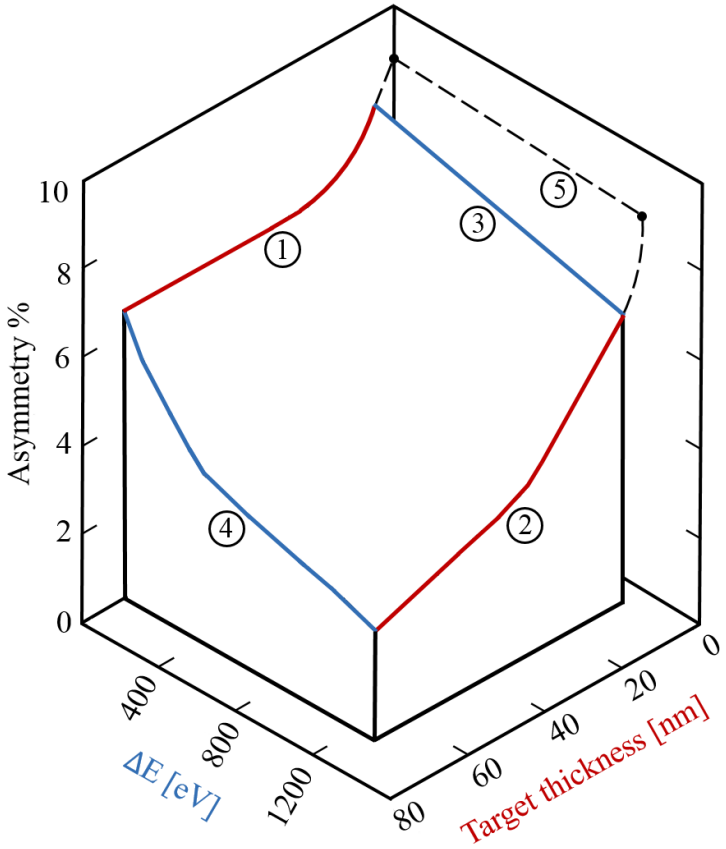

Figure 3.14: Mott asymmetry as a function of the gold target thickness and the electron energy loss at beam energy of 20 keV. ΔE denotes the maximum energy loss which electrons can have and still be detected. Curve ① shows the dependence of asymmetry on target thickness with no energy loss (elastic scattering). Curve ② represents the thickness dependence for a 1.2 keV energy loss. Curve ③ demonstrates the asymmetry dependence on the energy resolution for a thin target. Curve ④ presents the energy resolution dependency for a 68 nm gold target, and curve ⑤ indicates the asymmetry dependency on energy resolution for single atoms. Reproduced from [44].

As the target thickness increases, the probability of such processes substantially increases, which in turn reduces S_{eff} significantly. Thus, extremely thin gold targets are desirable for the asymmetry measurements. Moreover, the effect of multiple scattering is worsened at lower energy, resulting in further reduction of S_{eff}.

4 Measuring principles and preparatory measurements

After reconstruction of the PKAT laboratory was completed, experimental testing was initiated to discern the functionality of the instruments and to obtain the parameters for optimum measurements. The PKAT is equipped with instruments to test the temporal distribution and polarization characteristics of a photocathode. Some of the instruments used for these purposes include: a *Ti-Sapphire* laser to probe the photoemissive properties of the semiconductor photocathode, a deflecting cavity, a slit and a channeltron to study the temporal distribution of the beam, a spin-rotator Wien filter, and a Mott polarimeter to measure the average asymmetry.

Of the above-mentioned instruments, the Wien filter was the latest addition to the laboratory and had to be commissioned for operation. Furthermore, the Mott polarimeter had not been in operation since the last asymmetry measurements performed in 2011 [100]. More importantly, the electron gun was not equipped to deliver energies beyond 45 keV without experiencing field emission, as compared to the 100 keV previously, see the discussion in Section 3.3.

Therefore, the execution of a variety of tests to discern the possibility of conducting the pulse response and polarization measurements with the PKAT beamline under suboptimal conditions was crucial. Consequently, a number of systematic tests on the Wien filter and the Mott polarimeter were required to study the reproducibility of the measurements and to obtain the parameters necessary to achieve optimal experimental results. This testing included finding the Pockels cell's high voltage set up to produce circularly polarized light, obtaining the Wien filter spin-rotator high voltage and current set up, and determining the Mott detector amplifier threshold voltage.

The most challenging aspect of this project was accounting for the very low-energy electron beam. One of the difficulties working with such a low-energy beam was accomplishing the transport of the electron bunches from the cathode to the detecting point while preserving beam emittance and energy spread at a level acceptable for effective measurements.

The difficulties due to the advanced age of the apparatus, in combination with the low-energy beam, hampered the performance and operational reliability of the PKAT system. Less than ideal beam quality significantly impaired the time resolution of the apparatus, see Section 3.5. This difficulty especially tarnished the time response measurements using the slit, as the accuracy of these type of measurements rely on having a very small beam with high brightness to be able to scan the beam through the slit by changing the phase.

A defining challenge was the negative impact of the low-energy electron beam on the polarization measurements. The lack of energy notably decreases the Mott polarimeter analyzing power, leading to much lower asymmetry values. As a result, obtaining accurate asymmetry measurements with same statistical error throughout the measurements requires a much longer time, see the discussion in Section 5.8.

In the following, the setups for different types of investigations in the course of this project and the related preparatory procedures are explained.

4.1 Beam width measurement

The screen method offers a fast recording of the electron beam. This speed is advantageous over the slit method because the jitter contribution to the time resolution is much smaller in this method. However, the slit method has the advantage of allowing recording of the low intensity area in the tail of the pulse response, known as longitudinal halo. The CCD camera has a much lower dynamic range compared to the channeltron, and as a result, the CCD camera is limited in the recording of the tail. Within the scope of this thesis, the screen and camera method was used to determine the transverse beam diameter of the electron pulse, and the slit and channeltron method was used for the time response measurements.

A schematic representation of the screen method is illustrated in Fig. 4.1. In this method, the measurement duration depends on the required exposure time, which hinges on the current density. For the average extracted currents between 0.1 nA to 10 nA, limited by the space charge in the PKAT transport system, the CCD camera is capable of resolving images between 10 ms to 50 ms. This imagery corresponds to a superposition of between 7.60×10^5 to 3.88×10^6 pulses.

4.1.1 Screen calibration

Two necessary pieces of information are required in order to calibrate the screen: 1) conversion of pixels to micrometers and 2) conversion of micrometers to picoseconds. Having the diameter of the screen, 23 mm, the needed information can be obtained with the help of an image of a deflected beam on the screen created with a DC laser; see the left photo in Fig. 4.2. For better visualization, the colors in the image are inverted.

The beam is deflected by a fixed and arbitrary power of $P_{\mathrm{cav}} = 63\,\mathrm{W}$. The circumference of the screen is shown in red with the diameter D, and d denotes the size of the beam on the screen. The two end points of the beam stripe represent the reversal points of the sinusoidal deflection through the cavity.

According to the image in Fig. 4.2, the diameter of the screen is equivalent to 440 pixels. Therefore,

$$1\,\mathrm{px} \equiv (52.3 \pm 0.2)\,\mu\mathrm{m} \tag{4.1}$$

Due to the unknown accuracy of the screen dimension, the numbers which are derived from Eq. 4.1 are estimated to have an error of 1 %. Plotting the intensity

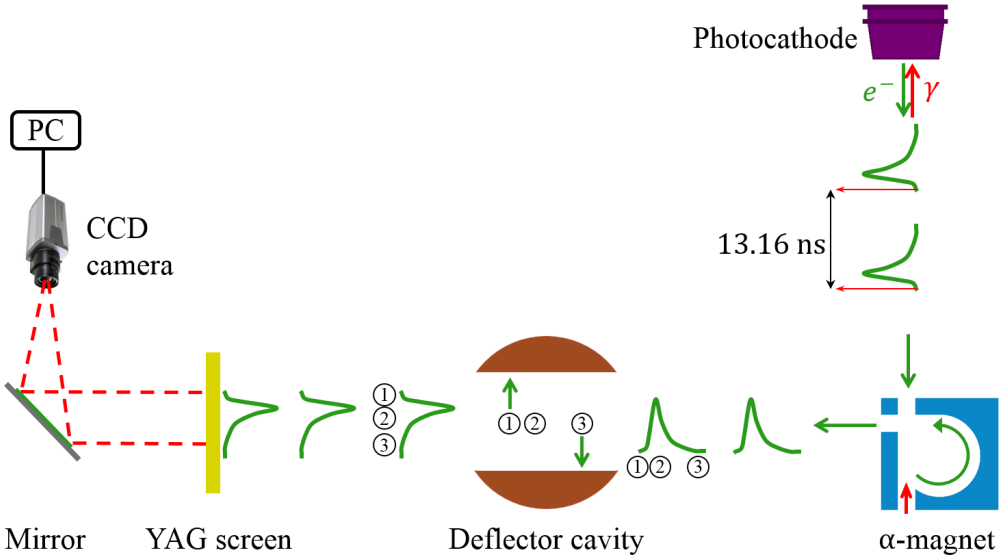

Figure 4.1: Schematic representation of the screen method. After the electron beam passes through the cavity, the beam impinges on the YAG screen. The emitted light is recorded by the CCD camera, and the image is analyzed with a computer.

profile of the observed beam results in what is shown on the right side of Fig. 4.2. The position of the beam on the screen at a given time t can be described by a sinusoidal deflection

$$x(t) = X \sin(\omega t) \tag{4.2}$$

where X denotes the amplitude of the deflection on the screen, and ω is the angular frequency equal to $\omega = 2\pi \cdot 2.449\,\mathrm{GHz}$. At a reference time of $t = 0$, the velocity is

$$\dot{x}(t) = X \cdot \omega. \tag{4.3}$$

The deflecting amplitude, according to Eq. 3.4, is proportional to the square root of the applied RF power in the cavity. If the amplitude at a reference cavity power is known, one can use the inverse steepness relationship to calculate the amplitude for other cavity powers. This leads to

$$S^{-1} = \sqrt{\frac{P_{\mathrm{ref}}}{P_{\mathrm{cav}}}}\,(X \cdot \omega)^{-1}\,. \tag{4.4}$$

In our case, P_{ref} is $P = 63\,\mathrm{W}$, and X can be deduced from the images in Fig. 4.2. The distance between the two end points, d, represents twice the amplitude. Together, by applying Eq. 4.1, one obtains

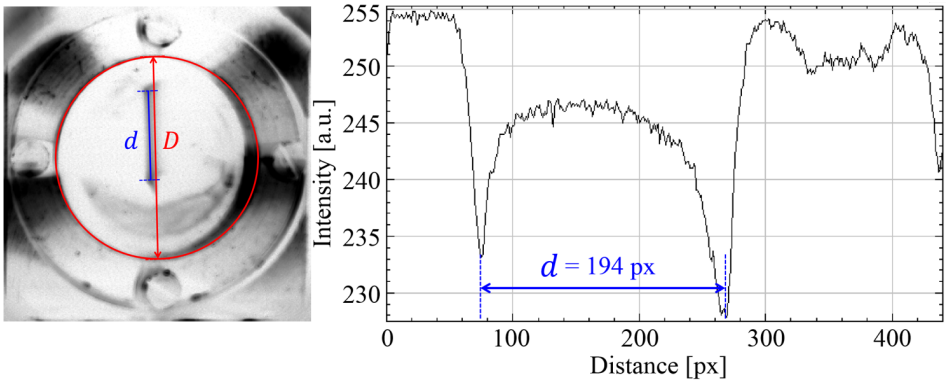

Figure 4.2: On the left: The image of the beam after being deflected with an arbitrary RF power. Laser and RF are not synchronized to allow the full deflection amplitude to be seen. For better clarity, the image is inverted and the circumference of the screen is shown in red. D and d represent the screen diameter and the size of the beam on the screen, respectively. On the right: Intensity profile of the observed beam on the left.

$$X = \frac{d}{2} = 97\,\mathrm{px} = (5.07 \pm 0.02)\,\mathrm{mm}. \tag{4.5}$$

For the cavity operating at $P_{\mathrm{cav}} = 322\,\mathrm{W}$, the result is

$$\begin{aligned} S^{-1} &= \sqrt{\frac{63}{322}} \cdot (X \cdot \omega)^{-1} \\ S^{-1} &= 5.67\,\mathrm{ps\,mm^{-1}}. \end{aligned} \tag{4.6}$$

Eq. 4.1 together with Eq. 4.6 provide the necessary information for the screen calibration. It is estimated that S^{-1} has a typical error of 1 %.

4.1.2 Transverse beam diameter

As previously discussed in Section 3.5, there are two factors limiting the time resolution of a pulse response measurement, apparative resolution and transit time dispersion. The transverse beam diameter is one factor contributing to the apparative resolution. To reduce this contribution in the time response measurements, the beam is optimized so that it has the smallest transverse diameter possible.

The transverse beam diameter is measured by operating the laser in DC mode while the deflector cavity is switched off. Fig. 4.3 represents an image of the electron beam taken with the CCD camera at 500 ms exposure time.

Assuming that the intensity has a Gaussian form, one can calculate the FWHM of the beam from the Gaussian fit. In the y-direction, this leads to

$$\mathrm{FWHM} = (6.3 \pm 0.1)\,\mathrm{px}. \tag{4.7}$$

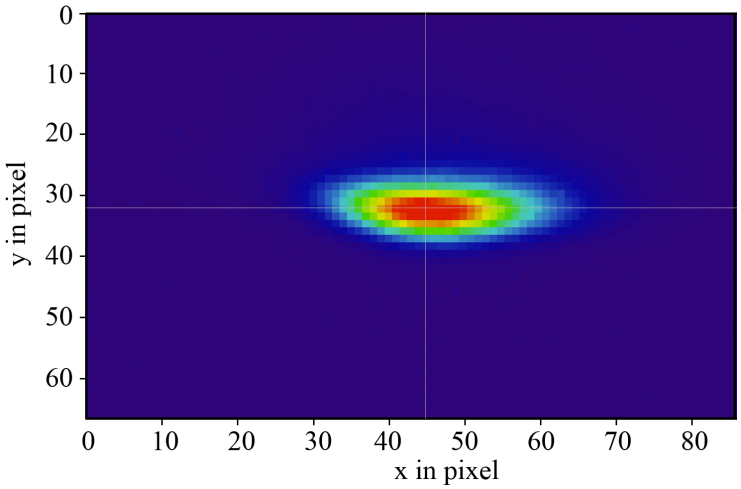

Figure 4.3: Image of the electron beam on the screen prior to the pulse response measurements. In order to reduce the contribution of the jitter to the resolution, the beam is focused with the minimum transverse width. The horizontal and vertical lines going through the beam show the positions at which the beam diameter in the x and the y direction were calculated.

Implementing the obtained conversion equations, Eq. 4.1 and Eq. 4.6, will result in the transverse beam diameter of

$$D_{\text{beam}} = (330.4 \pm 5.2)\,\mu\text{m} \equiv (1.87 \pm 0.03)\,\text{ps}. \tag{4.8}$$

4.2 Pulse response measurement

In order to measure the temporal profile of the electron pulse with large dynamic range, the slit method is used. A schematic representation of the setup for these measurements is shown in Fig. 4.4. The method can be explained by the following steps. First, the laser pulse is synchronized with the RF of the cavity. Then, as the beam goes through the cavity, the longitudinal profile of the electron pulse is transferred to the transverse. Next, by changing the phase from the zero crossing of the cavity in small steps, the transverse position of the beam shifts, and only a specific portion of the pulse is allowed to go through the slit. The transmitted current is amplified and detected with the help of the channeltron and a picoammeter.

4.2.1 Beam length and cavity power

As indicated by Eq. 3.4, the amplitude of the deflected electron pulse depends on the RF power applied to the cavity. In this section, the RF power was applied at

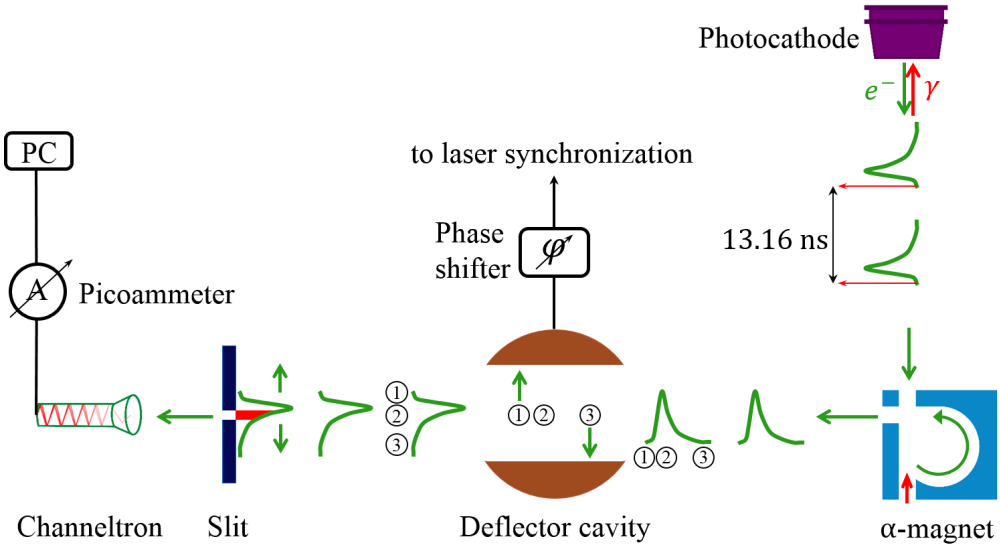

Figure 4.4: Schematic representation of the slit method for the pulse response measurements. The laser and the RF of the cavity are synchronized. After the electron pulses pass through the cavity, by changing the phase, the beam profile is scanned across the slit. The channeltron amplifies the transmitted current before the current is measured with the picoammeter and is later analyzed with a computer.

different levels and the observable length of the beam on the screen was measured for each level. The results are presented in Fig 4.5.

The measurement was accomplished with the help of steering magnet 20[1], located directly behind the screen. First, the screen was calibrated according to the steering magnet current. While the cavity was switched off, the beam was moved along the vertical diameter of the screen and the current through the steering magnet was recorded. This calibration resulted in

$$578\,\mathrm{mA} \equiv 23\,\mathrm{mm} \quad \therefore \quad 1\,\mathrm{mA} \equiv 39.79\,\mu\mathrm{m} \tag{4.9}$$

Then, the RF power was changed slightly and the steering magnet current was changed so that the two ends of the beam stripe matched up with the edges of the screen. The net current was converted to the unit of length, and the diameter of the screen was subtracted from or added to the conversion result, depending on whether the beam was smaller or larger than the screen. In Fig. 4.5, the fit function to the data is shown in black. The fit function indicates a square root pattern, as expected, due to the amplitude of deflection changing with the square root of the cavity power, see the discussion in Section 3.4.4. The measured beam length values are twice the deflection amplitude, as shown in Section 4.1.

[1]The numbering is according to the number of elements in the PKAT data base.

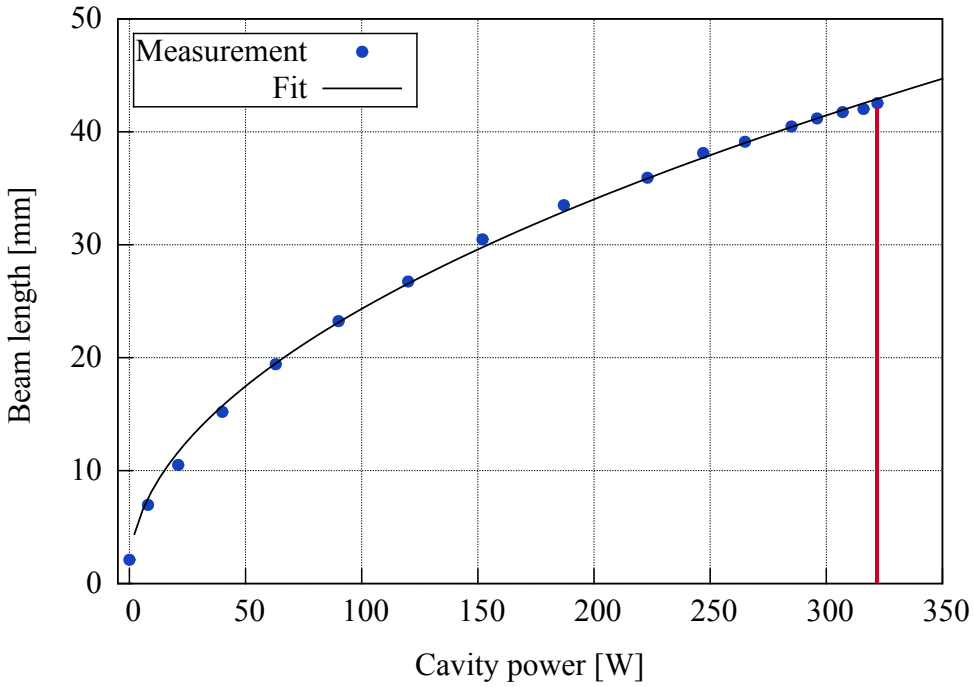

Figure 4.5: The observed length of the beam on the screen as a function of the deflector cavity power. The black curve represents the fit to the data, with a square root pattern. The red line at 322 W indicates the operating power of the cavity for all pulse response measurements. The observable beam length is twice the amplitude of the deflection (see the discussion in Section 4.1).

4.2.2 Calibration of the phase shifter

Prior to pulse response measurements, the electronic phase shifter must be calibrated to obtain the conversion between the applied voltage and the actual phase values. Phase shifter calibration was performed [18] and the results are illustrated in Fig. 4.6.

The electron pulse response measurements are based on the principle of relative phase variations. Therefore, as the electron pulses pass through the deflector cavity the actual phase value at the point of no deflection is not of importance. However, it is important to ensure that scanning the entire pulse through the slit is completed within the best linear region of the calibration. For this reason, at the beginning of each measurement, the electronic phase shifter was set to ≈ 3 V and the deflection was zeroed with the help of the mechanical phase shifter. The pulse response measurements in the course of this project were performed with the electronic phase shifter operating in the range of 3 V to 6 V. In Fig. 4.6, this region is specified with green color.

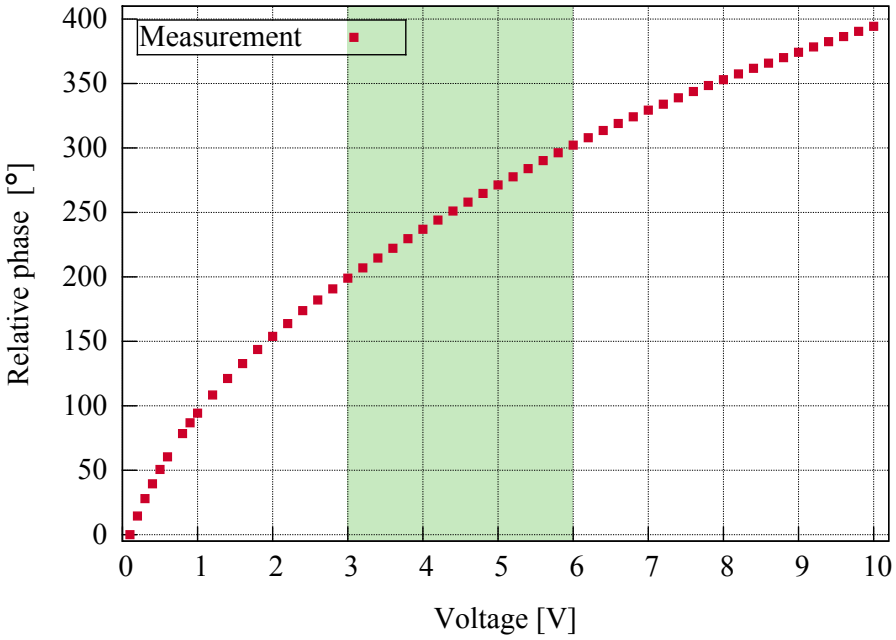

Figure 4.6: Calibration of the electronic phase shifter. Changing the voltage from 0 V – 10 V correlates with a phase shift variation of 0 - 400°. The pulse response measurements in this project were performed with the phase shifter operating in the best linear region in the range of 3 - 6 V, represented by the green area. Data obtained from [18].

4.3 Asymmetry measurement

Regardless of the type of spin-polarized source used in the accelerator system, the underlying principle of the investigation in all experiments using polarized electron beams is based on measuring the spin-dependent asymmetries. These asymmetries derive from the small differences in the detected signals, as the polarization of the incident electrons is reversed. Therefore, it is crucial to have a highly polarized intense electron beam, as well as, having stable conditions as polarization is reversed.

Part of the investigation in this research was performing asymmetry measurements. Fig. 4.7 depicts a schematic representation of these measurements.

First, the linearly polarized light is converted to circularly polarized light as it travels through the Pockels cell. The electron beam is guided through the α-magnets and then is directed through the Wien filter. In the Wien filter, the polarization of the electron beam is switched to transverse before entering the Mott polarimeter. In the Mott, electrons are backscattered through their interactions with the gold foil and are detected with the two detectors. The asymmetry is determined according to the detectors count rate, as the polarization of the electrons is switched by reversing the helicity of the laser light.

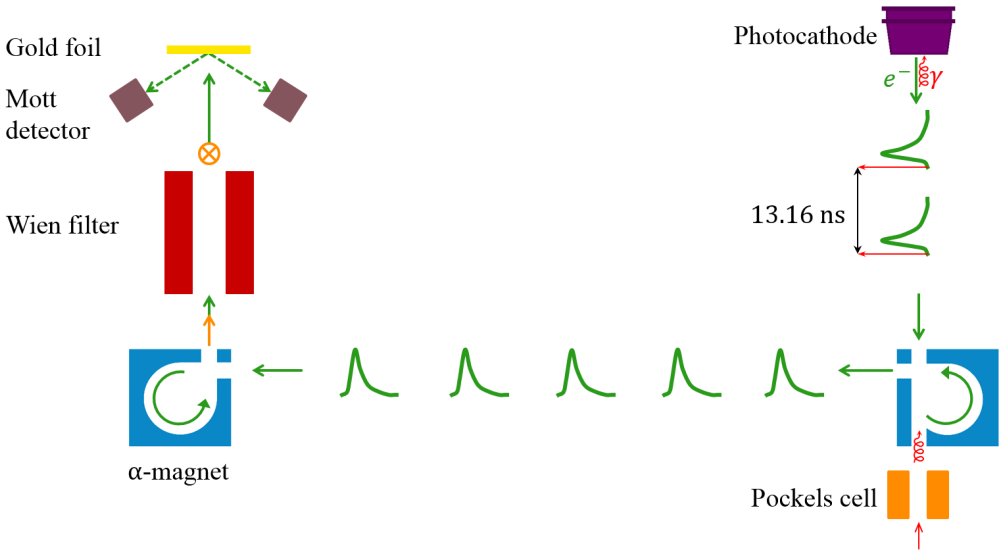

Figure 4.7: Schematic representation of the asymmetry measurements in the PKAT. In the Pockels cell, linearly polarized light is converted to circularly polarized light. After electron pulses are produced, they travel through the α-magnets. Before electrons enter the Mott, their polarization is rotated in the Wien filter from longitudinal to transverse. The red and the green arrows show the laser polarization and the direction of the electron beam travelling, respectively. The orange arrow and the cross symbol indicate the direction of electron polarization before and after the Wien filter.

In the following, the preparatory steps to achieve optimum asymmetry measurements are described.

4.4 Obtaining the circularly polarized light

In order to achieve the highest possible polarization and to have an accurate measurement, any helicity-correlated asymmetry must be avoided. In an ideal case, a circular polarization of 100 % is desirable. To attain the best circularly polarized light, the alignment of the Pockels cell crystal axis with the laser axis is critical. A photo of the Pockels cell being adjusted to deliver the maximum circularly polarized beam is shown in Fig. 4.8.

The alignment is obtained with the help of two linear polarizers placed at each end of the Pockels cell. The second polarizer is used as an analyzer. The alignment should fulfill two conditions. First, the intensity directly after the crystal must not fluctuate while the crystal is rotated around the optical axis. Second, the intensity after the second polarizer must remain minimal, even when the voltage is applied. Once the optimal condition is achieved, the crystal is rotated 45° around the optical

axis, enabling the crystal to operate as a quarter waveplate and generating the state of circular polarization.

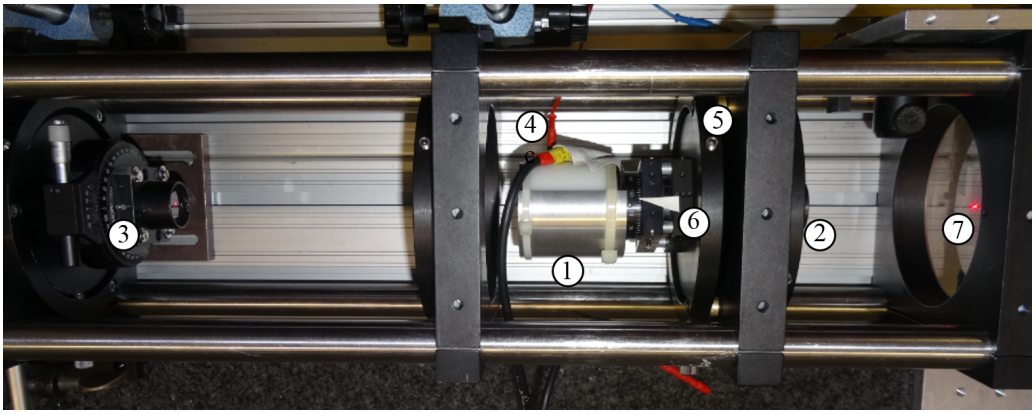

Figure 4.8: Photo of the Pockels cell inserted in its housing and being adjusted to deliver the highest circularly polarized light. The main parts are: ① the Pockels cell, ② the first linear polarizer, ③ the second linear polarizer used as an analyzer, ④ the Pockels cell high-voltage connection, ⑤ the small springs for fine adjustment of the Pockels cell along the three axes, ⑥ marking of the Pockels cell prior to 45° rotation, and ⑦ the laser being directed towards the first linear polarizer. Before conducting the experiment, the analyzer is removed and a telescope is inserted after the Pockels cell.

By applying voltage to the Pockels cell, I_{min} and I_{max} through the analyzer is recorded and circular polarization is calculated

$$P_{\text{cir}} = \frac{2\sqrt{I_{\text{min}} \cdot I_{\text{max}}}}{I_{\text{min}} + I_{\text{max}}} \tag{4.10}$$

For each voltage the polarity is reversed, and P_{cir} is obtained. The results are shown in Table 4.1.

Once the state of maximum circular polarization is obtained, the second polarizer, which is located after the Pockels cell, must be removed before performing the asymmetry measurements. A detailed description of the Pockels cell adjustment procedure can be found in [74].

Table 4.1: Obtained values of circular polarization at 3.1 kV

HV polarity	I_{min} (mW)	I_{max} (mW)	P_{cir}
+	2.51	2.20	$(99.8 \pm 0.1)\,\%$
−	2.83	2.46	$(99.8 \pm 0.1)\,\%$

4.5 Preparatory diagnosis and operational factors

As already discussed, portions of the PKAT had to be reconstructed in order to perform the polarization measurements. The Mott polarimeter had not been used for more than five years; thus, examination of the status of the Mott polarimeter was necessary. Moreover, the asymmetry measurements are inherently sensitive to the physical and mechanical conditions of the lab, such as the energy of the electron beam and the electronic noise. This section outlines some of the challenges encountered and methods of overcoming the challenges to ensure the asymmetry measurements were reproducible and reliable.

One of the Mott detectors had a deficiency and was replaced. Moreover, an observed grounding problem was mitigated by using an isolating transformer for the detection electronics and by significantly shortening the distance between each of the detectors and the respective amplifiers.

A penalty of operating at a low energy of 45 keV was the decreased immunity of the system to any electronic noise. The measurements were susceptible to instabilities in any frequency region, especially 50 Hz and harmonics. For example, although the MAMI accelerator source power supply was located far from the PKAT laboratory, the effect of turning on the MAMI source on the detector count rate was clearly observed. In one incident, upon turning on the MAMI accelerator source, the background counts jumped from below 10 Hz to almost 4000 Hz. Also, from time to time an abrupt spike on the background counts, even up to 65 000 Hz, was observed, even though no adjustments had been made.

Therefore, significant efforts were devoted to identifying any sources of noise and determining practical solutions to alleviate them. In addition, the Mott detector preamplifiers were carefully shielded with copper against any electromagnetic interference and all the beamline windows were fully covered against any stray photons entering the detectors.

The optimum operational factors for asymmetry measurements were obtained and the noise level was reduced so that it was discriminated against the background. Typical signal to background ratio was 300 : 1.

The Mott polarimeter in the PKAT laboratory is equipped with three gold targets of different thicknesses. A photo of the three gold targets with their associated numbering in the data system is shown in Fig. 4.9. The Target3, which is the thinnest gold foil, with a thickness of 85 nm, is placed on a carbon foil to make it less susceptible against damage. This placement explains the blue color seen in the photo.

By using the Mott scanner, the positions of the gold targets were obtained. Table 4.2 presents the specifications of these gold targets and their respective positions on the scanner. In addition, the region in which the Mott detector counts were linear as a function of the laser power was determined. During each measurement, to avoid distorted asymmetry values due to the nonlinear effects from high laser intensities, care was taken to ascertain that the illumination intensity was low enough to ensure the detectors operated in the linear region.

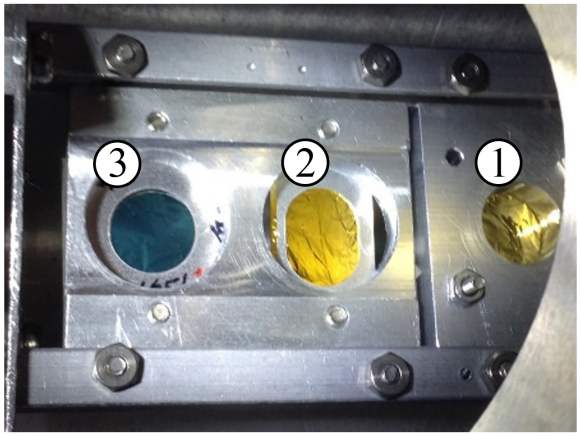

Figure 4.9: The three gold foils in the Mott polarimeter of the PKAT beamline. The numbering of the targets is according to their numbers in the data system.

Table 4.2: Gold targets in the PKAT Mott polarimeter and their specifications

Gold target	Area density	Thickness	Scanner position
(1)	$415\,\mu g\,cm^{-2}$	215 nm	91 mm
(2)	$190\,\mu g\,cm^{-2}$	98 nm	68 mm
(3)	$165\,\mu g\,cm^{-2}$	85 nm	48 mm

4.6 Wien filter calibration

In preparation for the asymmetry measurements, the Wien filter was built and installed in the PKAT beamline. Due to the beam energy being reduced in comparison to past experience, it was necessary to obtain the Wien filter high voltage and magnet current to ensure the condition of "no deflection". Fig. 4.10 depicts a picture of the Wien filter after installation in the PKAT beamline.

The Wien filter at MAMI has been used successfully for the last two decades. Therefore, its electric and magnetic field strength were used as a point of reference to obtain the electrodes high voltage and the magnetic coils current of the Wien filter in the PKAT. For a spin rotation of 90°, the required electric and magnetic field strengths and the Wien filter parameters are listed in Table 4.3. For comparison, the parameters for the MAMI Wien filter are also presented.

Regardless of the different energies between the two electron sources, the relation $B = m_0\beta c\gamma^2\theta/eL$ (Eq. 3.18) is valid for the spin rotation of both Wien filters at the state of no deflection.

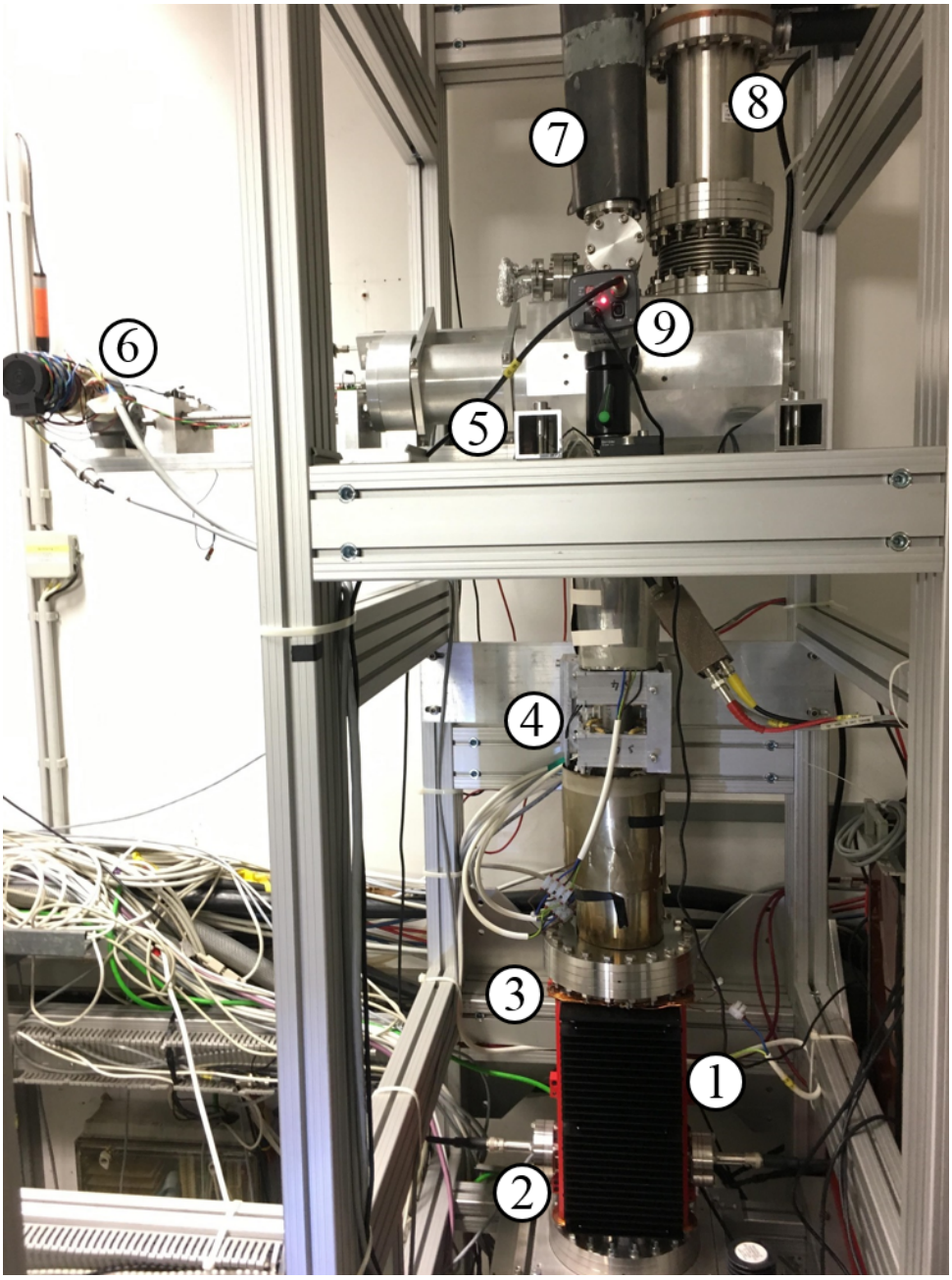

Figure 4.10: A photo of the Wien filter installed in the PKAT beamline in preparation for asymmetry measurements with Mott polarimeter. The numbers represent: ① Wien filter, ② high voltage feed through, ③ magnetic coils to produce magnetic field inside the Wien filter, ④ quadruple doublet to correct against the Wien filter astigmatism, ⑤ Mott polarimeter, ⑥ Mott scanner to allow the movement of the targets on the rail, ⑦ Faraday cup used as a beam dump, ⑧ Ion Getter pump, and ⑨ Camera to monitor the beam position on the Mott screen.

Table 4.3: Specification parameters for both PKAT and MAMI Wien filters

Parameter	**Wien filter PKAT**	**Wien filter MAMI**
Energy	45 keV	100 keV
β	0.39	0.55
Electrodes gap	15 mm	20 mm
Electric field	0.44 MV m^{-1}	1.04 MV m^{-1}
Magnetic field	3.75 mT	6.30 mT
High-voltage	3.32 kV	10.36 kV
Current	6.50 A	5.78 A

For the state of 90° rotation, $\theta_{45}/\theta_{100} = 1$, where the subscripts refer to the energy of each of the electron sources. This scenario will lead to

$$\frac{\theta_{45}}{\theta_{100}} = \frac{E_{45}}{E_{100}} \cdot \frac{(\gamma^2 - 1)_{100}}{(\gamma^2 - 1)_{45}} = 1, \tag{4.11}$$

and therefore,

$$E_{45} = \frac{(\gamma^2 - 1)_{45}}{(\gamma^2 - 1)_{100}} \cdot E_{100}. \tag{4.12}$$

Using the values from Table 4.3, the electric field strength between the electrodes is

$$E_{45} = 443.13\,\text{kV m}^{-1} \tag{4.13}$$

and with the gap between the electrodes $d = 15\,\text{mm}$, the total voltage can be obtained

$$V_{45} = 6.65\,\text{kV} \quad \therefore \quad V = 3.32\,\text{kV} \quad \text{for each plate.} \tag{4.14}$$

The corresponding magnetic field is, therefore,

$$B_{45} = 3.75\,\text{mT} \tag{4.15}$$

which is equivalent to a current of approximately $I = 6.5\,\text{A}$ for the coils.

Having obtained the Wien filter setup parameters, one can perform the asymmetry measurements. However, a couple of comments are in order before proceeding with the measurements. First, although the PKAT Wien filter is a replica of the MAMI Wien filter, the magnetic coils are not completely identical. The latter has 14 turns of coil, compared to 10 turns for the PKAT. This difference contributes to the different currents.

In addition, due to an error in the Wien filter calibration the asymmetries were measured at 120° deflection. This means the measured asymmetries were 86 %

($\sin\theta = 0.87$) of the values had the Wien filter been set properly. However, it must be noted that all the asymmetry values presented in this project have been corrected against this effect by multiplying the asymmetries by a factor $1/\sin\theta = 1.15$.

Verifying the Wien filter calibration

Although the high-voltage setup for the Wien filter was obtained through calculations, verification that the setup produced the highest asymmetry for a spin rotation angle of $\frac{\pi}{2}$ had to be confirmed. For this reason, the asymmetries for a range of voltages were measured. The electrodes high voltage was changed from 0.09 kV to 4.43 kV in increments of 0.25 kV. For each voltage, the corresponding magnetic coils current to deliver the optimum beam on the Mott screen and fulfill the no-deflection condition through the Wien filter was obtained. The results are demonstrated in Fig. 4.11.

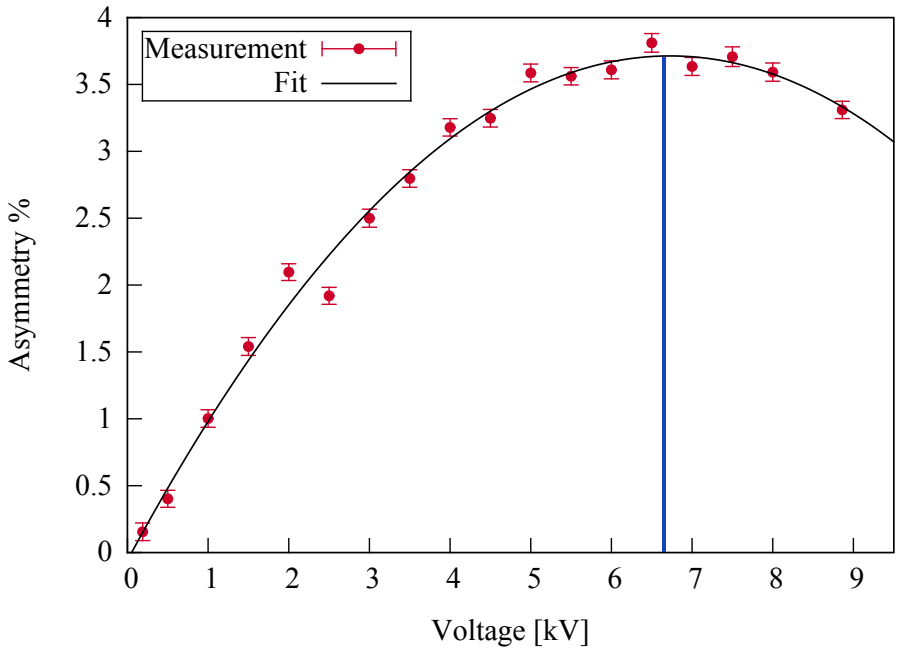

Figure 4.11: Measured asymmetries as a function of the Wien filter high voltage. The black curve is the best fit to the data, and the blue line at $V = 6.65$ kV indicates the voltage at which a spin rotation of 90° to achieve the maximum asymmetry is obtained.

The error bars in Fig. 4.11 represent the statistical errors. According to Fig. 4.11, the optimum voltage set up for the Wien filter is $V = 6.65$ kV, which is in agreement with our calculations, see Eq. 4.14.

4.7 Position of highest asymmetry using Mott screen

The Mott chamber in the PKAT is equipped with a view screen to monitor and focus the electron beam at the target. The Mott screen was scanned to determine the beam position which delivers the highest asymmetry. This position was determined by steering the beam position around a fixed gold target. Figure 4.12 shows the Mott screen with the electron beam at different positions indicated by the corresponding numbers.

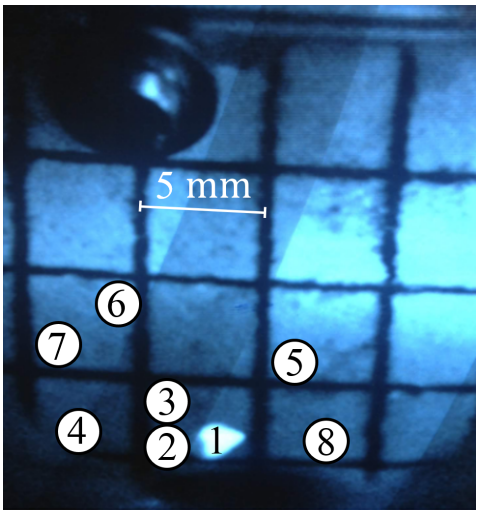

Figure 4.12: The numbers denote the position of the electron beam on the Mott screen where the asymmetry was measured. The asymmetry values are listed in Table 4.4. Position number 8 shows the location of the beam dump. The distance between each two adjacent lines on the screen is 5 mm.

Table 4.4: The asymmetry values of the scattered electrons from the gold Target2. The numbers correspond to the beam positions on the Mott screen.

Position	Asymmetry
①	4.11 ± 0.19 %
②	4.06 ± 0.19 %
③	3.71 ± 0.18 %
④	3.60 ± 0.22 %
⑤	2.72 ± 0.16 %
⑥	2.57 ± 0.21 %
⑦	2.36 ± 0.21 %
⑧	4.98 ± 0.23 %

Position 8 represents the location of the Faraday cup which is used as a beam dump. The respective asymmetries are gathered in Table 4.4. In all the asymmetry measurements, the electron beam was focused on position 1.

4.8 Time-resolved polarization measurement

After the preparatory asymmetry measurements were completed, the time-resolved polarization of the electrons, for both bulk GaAs and SSL GaAs/GaAsP, was investigated. The schematic representation of the setup to perform time-resolved polarization measurements is illustrated in Fig. 4.13.

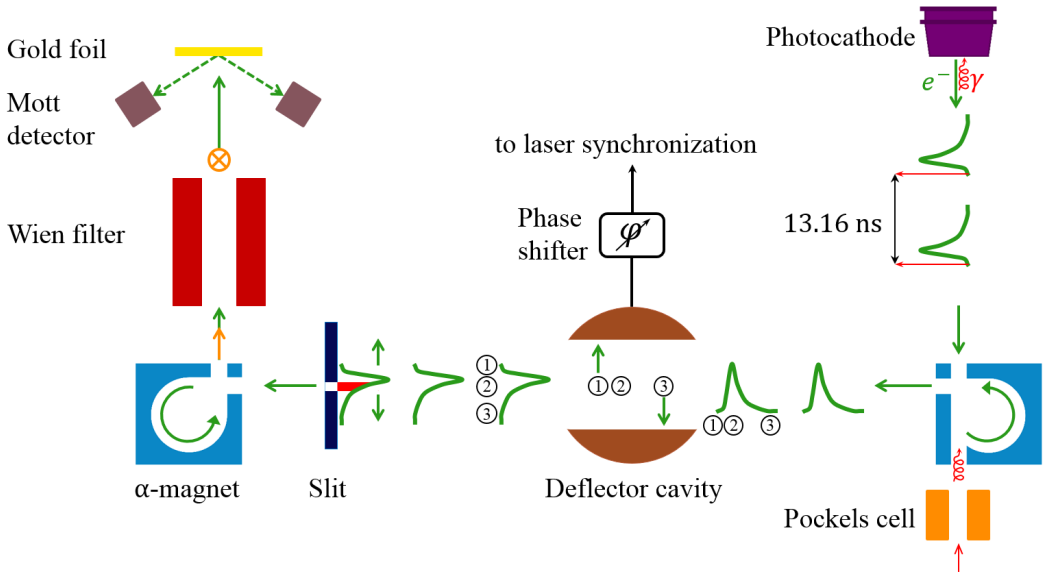

Figure 4.13: The schematic representation of the setup for the time-resolved polarization measurements. The laser and the RF of the cavity are synchronized. The linearly polarized light is changed to circularly polarized light as the laser travels through the Pockels cell (the red arrows). Then, as the electron pulses (green arrows) travel through the cavity, their longitudinal profile is transferred to a transverse profile. The polarization of the electrons is rotated by 90° as they travel through the Wien filter (the orange arrow and the cross symbol). The backscattered electrons from the gold foil are detected by the Mott detectors. By shifting the phase in small steps, a different part of the beam profile is scanned through the slit, and its associated asymmetry is measured with the Mott detectors.

After the electron pulses are generated and pass through the cavity, the electron profile is changed to a transverse profile. The phase between the laser pulse and the RF of the deflector cavity is varied in discrete steps. For each discrete variation of

the phase, only one specific portion of the electron pulses is allowed to pass through the slit. As the transmitted portion of pulse is passed through the Wien filter, the polarization of the electrons is switched to transverse. In the Mott, electrons are backscattered from the gold foil, and their asymmetry is obtained with the help of the Mott detectors. By systematically continuing to shift the phase, the complete profile of the polarization in a time-resolved manner can be obtained.

5 Experimental results and discussion

Once the systematic tests were completed, and the preliminary measurements proved to be consistent and reproducible, the study of the photocathode itself began. Two types of photocathodes have been used during the course of this research. First, commercial bulk GaAs with an active layer thickness of $510 - 517\,\mu m$ and heavily doped p-type with Zn to a level of $(1.10 - 1.32) \times 10^{19}\,cm^{-3}$. The second type is a strained GaAs/GaAsP superlattice with a layered active layer of 92 nm. This chapter covers the results regarding the bulk GaAs. The results of the strained GaAs/GaAsP superlattice investigations will be the subject of the next chapter.

5.1 Cathode preparation and activation

Before the photocathode is placed in the source chamber, it must be activated. The activation procedure starts with the preparation of a chemically clean surface, free from carbon and oxide contaminants. This process achieved in the preparation chamber by heating the cathode to 600 °C for 30 min to remove the excess Cs atoms and other residual contamination from the surface. During the activation process, if the temperature is too high (650 °C) it will cause the Ga atoms to evaporate from the crystal. Thus, care must be taken to avoid very high temperatures. After the cathode is cooled down to room temperature, it is ready to be activated to the NEA state. For this purpose, the so-called co-deposition technique is used: simultaneous deposition of caesium and oxygen.

The process consists of exposing the GaAs cathode surface to the Cs flux generated by a dispenser, which is heated by an electrical current of 3.60 A. During the deposition, the GaAs cathode is illuminated with a laser of 640 nm wavelength. After a certain time, as the Cs atoms are deposited on the surface of the GaAs crystal, the photocurrent increases due to the decrease in the electron affinity. As the Cs deposition is continued, the photocurrent reaches a peak and then begins to drop. The drop of the photocurrent is possibly due to a nonequilibrium concentration of Cs atoms deposited on the surface of the cathode, which gives rise to the depolarization of the Cs dipole [12].

Soon after the photocurrent starts dropping, and while the Cs deposition continues, the O_2 is introduced into the chamber through a mechanically operated leak valve at a typical pressure between $(1.0 - 5.0) \times 10^{-9}$ mbar. While O_2 is being administered, care is taken to assure the pressure in the chamber does not exceed 1.0×10^{-9} mbar. As O_2 is admitted, oxide layers are formed on the surface of GaAs crystal, leading to a photocurrent increase, until the current reaches its peak and begins to decrease.

At this point, the valve is closed, the O_2 exposure is stopped, and the photocurrent increases again due to the Cs deposition. This cycle is repeated a few times until the photocurrent peak value becomes steady. Once the value is steady, the activation process is completed. After the activation, the photocathode is placed into the manipulator and transferred into the source chamber through a gate valve. The preparation chamber is pumped by an *Ion Getter* pump attaining a base pressure of 1.0×10^{-11} mbar. The details of the source and preparation chambers are given in an earlier publication [11].

5.2 Bulk GaAs

The bulk GaAs crystal activated with an atomic monolayer of Cs is an excellent photoemitter. This photoemitter has many applications in accelerators as a source of both spin-polarized [92] and non-polarized electrons [39]. Despite its very stringent vacuum requirements, demanding vacuum pressure in the order of 10^{-11} mbar or below, GaAs activated using Cs remains an excellent photoemitter due to its high *QE* in visible and near-infrared light and the low *MTE* of the emitted electrons [16].

As part of this research, some of the fundamental behaviors of bulk GaAs were investigated, including the temporal response of the photocathode in terms of both current and polarization, and the impact of the *QE* on the shape of the pulse response. The results of these investigations are presented and discussed in the following sections.

5.3 Effect of subsequent activation on QE

In the course of this research, two bulk GaAs photocathodes were used. The first photocathode had been activated more than 20 times previous to our experimentation, while the latter was activated for the first time during our measurements. To distinguish between them in our discussion, we shall henceforth refer to them as Cathode1 and Cathode2, respectively. Throughout the measurements as the *QE* dropped very low reactivating the cathodes became necessary. The reactivation procedure consisted of both heat cleaning and achieving the NEA state with Cs:O_2.

Immediately after each activation, the *QE* was measured. The *QE* obtained from the two bulk GaAs crystals was in the range of 6.10 % to orders of 10^{-6} %. Performing with extremely low *QE* was intentional and was an important part of this research. The motivation behind those measurements and their findings are discussed in Section 5.7.

For the new bulk GaAs, Cathode2, the third activation delivered the highest *QE* of 6.10 %, followed by *QE* degradation thereafter with each reactivation. A plot between the number of activation cycles and the *QE* obtained from the new bulk GaAs is shown in Fig. 5.1.

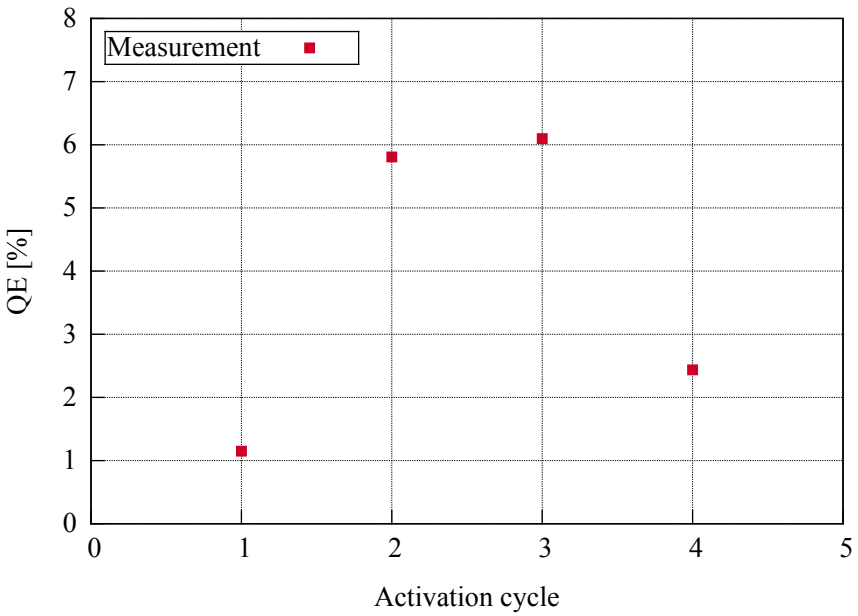

Figure 5.1: Plot showing the achieved *QE* against the activation cycle number for the bulk GaAs, Cathode2.

According to Fig. 5.1, while the relative increase of *QE* is only 5 % from the second to third activation, the *QE* relatively degrades by 60 % from the third to fourth activation cycle. The behavior of the GaAs photocathode has been observed in other studies such as [87, 132].

A possible explanation for this increase in *QE* in the second or third activation compared to the first activation is that during the heat cleaning process, the Cs atoms from the surface of the photocathode are not completely removed. In this scenario, during the heat cleaning, only the Cs atoms which are weakly bonded are desorbed from the surface, whereas those with a strong bond remain. These strongly bonded Cs atoms can find a favorable reconstruction on the surface, thereby resulting in a higher *QE* in the second and third activations.

On the other hand, since the heating temperature during the cathode preparation is not high enough, some of the oxygen atoms are left on the surface. These residual oxygen atoms will contaminate the photocathode surface after each activation. Consequently, the achieved *QE* will decrease with each activation thereafter; in our case, after the third activation [27].

5.4 QE lifetime

The *QE* lifetime is an important parameter for the photocathode and its practical use in the accelerators. The *QE* lifetime of the bulk GaAs photocathode used

throughout the experiments is shown in Fig. 5.2. The *QE*s were collected with an 800 nm laser over a 14-day period. The *QE*s range from 5.81 % to 4.94×10^{-6} %.

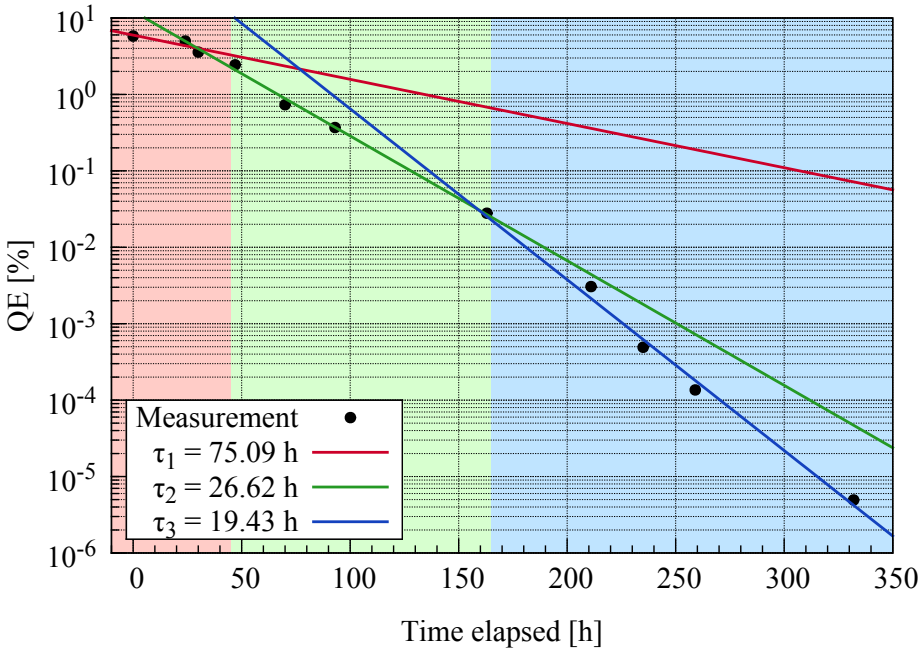

Figure 5.2: Degradation of the *QE* over 14 days for the bulk GaAs Cathode2 used for the measurements during this project. The *QE* decay cannot be described with one single lifetime.

Our data suggests that the cathode decay rate depends on the *QE* and cannot be described with a single time constant as suggested by Eq.2.2. The decay is exponential only during short intervals of a few days, but not throughout the entire time. Remarkably, this decay change rate is observed on many orders of magnitude. One can speculate that in the region $0 < t < 45$ h, the Cs : O layer has not reached equilibrium and is perhaps still self-organizing to an optimum. The timescale of the decay is $\tau_1 \approx 75$ h.

A significant change of slope occurs in the time interval $45\,\text{h} < t < 165\,\text{h}$ resulting in decay with a time constant of $\tau_2 \approx 27$ h, induced by the residual gases. The lifetime further becomes shorter in the region $t > 165$ h with $\tau_3 \approx 19$ h. This effect may result from several possibilities such as a more intense laser experimentation, opening valves or switching on the device which generates more gas. Alternatively, the change of slope during the cathode decay could have something to do with a sudden change of the surface, for example, changing from NEA to PEA conditions (see Section 5.7.2), but a definitive conclusion cannot be reached.

5.5 Pulse response measurements

In this section, the time response of the bulk GaAs using the slit method is investigated and the results are analyzed. In our study, to ensure precise measurement of the pulse response prior to each measurement, important precautions were taken, which merit some discussion here.

These precautions include, first, making sure the beam is passing through the zero crossing of the cavity, where the magnetic field of the cavity has no effect on the beam. The magnetic field changes during the passing of the electron pulse through the cavity. However, the entrance phase can be adjusted so that the electrons reach the center of the cavity when the field is zero. Second and of equal importance, ascertaining that the beam is well focused with the smallest transverse diameter at the slit position to allow high resolution measurements. Third, avoiding excessive space charge defocusing is essential. According to the previous investigations in the PKAT system, it was estimated that a typical bunch charge should be limited to the maximum 0.1 fC [8]. This charge is equivalent to approximately 620 electrons per bunch. For operation at 76 MHz, that amount translates to currents of $I < 10\,\mathrm{nA}$. Therefore, to avoid space charge defocusing and to prevent damaging the channeltron by excess current, an average beam current of $1 - 3\,\mathrm{nA}$ was chosen throughout our measurements.

The pulse response measurements were performed at an excitation wavelength of 800 nm with the cavity resonator operating at a power of 322 W. The channeltron high voltage was set at 1950 V, which delivers an estimated gain of 2000 according to [60]. Fig. 5.3 depicts a typical temporal pulse response for each of the two bulk GaAs crystals used in our studies.

The pulse impulse progression includes a steep ascending segment followed by a region where the behavior is approximately Gaussian, and then a slow exponential decay occurs. In order to have an equitable comparison between the pulses, the pulses of compatible QE, in the order of 10^{-3} %, are chosen. Both pulses exhibit very similar patterns with the new GaAs having a slower decay. Assuming that both peaks satisfy a Gaussian shape, the σ of (3.17 ± 0.50) ps and (3.33 ± 0.50) ps can be found for Cathode1 and Cathode2, respectively.

The measured temporal response of a cathode is a convolution of the true time response of the cathode plus the effects of the time resolution of the PKAT apparatus and the transit time dispersion of the cathode. The latter results from different starting energies of the electrons. The response of the photocathode consists of excitation time of the electrons, the transport time of electrons in the crystal, and the thermalization time of electrons since the thermalized electrons can be emitted also by diffusion.

In a bulk photocathode, the active layer extends throughout the entirety of the cathode, around 500 µm in this instance. As a result, the laser can penetrate deep into the crystal, and the excited photoelectrons have to travel long distances before they exit the crystal. Therefore, a long pulse response is expected for the bulk GaAs. This response can be seen clearly in Fig. 5.3.

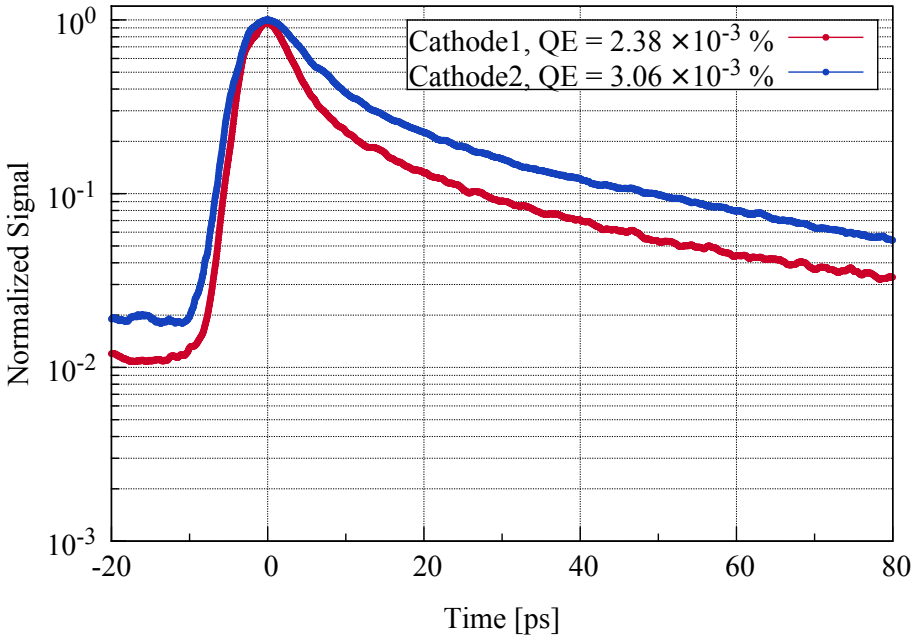

Figure 5.3: Pulse responses of the two bulk GaAs at an excitation wavelength of 800 nm are shown: in red for the GaAs Cathode1 after more than 20 activations and in blue for the Cathode2 after its first activation. For an equitable comparison, pulse responses of comparable *QE* are chosen.

According to Fig. 5.3, the slow exponential decay results in a longitudinal halo of approximately 4.5×10^{-2} and 8.0×10^{-2} compared to the relative peak intensity after 60 ps for Cathode1 and Cathode2, respectively. In Fig. 5.3, of interest to note is that although both measurements are conducted at about the same *QE*, the new GaAs crystal delivers a higher intensity throughout the entire pulse.

The photoexitation of the bulk GaAs with the 800 nm excitation had been previously recorded in [8, 35, 50], and the results indicate similar behavior. The focus of this project for the time response measurements of the bulk GaAs has not been on verifying or improving the previous results, but rather on the dependency of the time response on *QE*, and specifically, at very low *QE*s. The results of these investigations, which is palpable at *QE*s of about 10^{-4} % and lower, will be the focus of Section 5.7.

5.6 Modified diffusion model

The concentration of the photoexcited electrons in the active layer of the NEA GaAs semiconductor and its development in space and time can be found by solving the diffusion Eq. 2.21 from Chapter 2. Since the exciting laser beam diameter is several hundred micrometers, FWHM $\approx$ 150 µm, and the diffusion length is in the order

of 1 µm, a one-dimensional consideration of the diffusion model is sufficient. The repetition rate of the laser pulses is 76 MHz, which is equivalent to a period of 13 ns. The amplifier behind the slit operates with a bandwidth of 10 kHz.

In this discussion, the modification of the signal by the 76 MHz periodicity is found to be negligible. Moreover, the length of the laser pulse, which is approximately 150 fs, is practically negligible because it is more than one order of magnitude shorter than the experimental resolution. Allowing x to be the direction normal to the surface, the diffusion equation can be simplified to

$$D\frac{\partial^2}{\partial x^2}c(x,t) - \frac{\partial}{\partial t}c(x,t) - \frac{1}{\tau_{\mathrm{rec}}}c(x,t) = 0\,. \tag{5.1}$$

In [51], after applying boundary conditions, the solution to Eq. 5.1 was found. Assuming that no concentration outside of the active layer thickness d exists, and that the initial concentration at $t = 0$ must correspond to the absorption profile of the laser beam, one can write

$$\begin{aligned} c(d,t) &= c(0,t) = 0 \\ c(x,0) &\propto e^{-x/\alpha} \quad \text{for} \quad x \geq 0\,. \end{aligned} \tag{5.2}$$

However, the obtained solutions delivered unrealistically high values for the diffusion constant. Later, in [8], the solutions were improved by introducing a recombination time scale of approximately 100 ps. The solutions under these conditions take the form of

$$c(x,t) = e^{-t/\tau_{\mathrm{rec}}} \sum_{k=1}^{\infty} A_k \sin\left(\frac{k\pi x}{d}\right) e^{-\left(\frac{k\pi}{d}\right)^2 Dt} \tag{5.3}$$

The Fourier coefficients of A_k can be calculated to fulfill the boundary conditions and are given by

$$A_k = \frac{k\pi\left[1-(-1)^k e^{-\alpha d}\right]}{(\alpha d)^2 + (k\pi)^2} \tag{5.4}$$

The emitted current is proportional to the gradient of the concentration at $x = 0$

$$I(t) \propto \frac{\mathrm{d}}{\mathrm{d}x}c(0,t), \tag{5.5}$$

which leads to

$$I(t) \propto e^{-t/\tau_{\mathrm{rec}}} \sum_{k=1}^{\infty} A'_k\, e^{-\left(\frac{k\pi}{d}\right)^2 Dt} \tag{5.6}$$

with

$$A'_k = \frac{(k\pi)^2}{(\alpha d)^2 + (k\pi)^2} \tag{5.7}$$

Note that the factor $k\pi/d$ which appears after the differentiation can be neglected for the remainder of the discussion. However, a factor of $k\pi$ was retained in the numerator of A'_k to gain a simple expression for the asymptotic behaviour of the A'_k.

Assuming a single electron pulse has been produced, depending on the time t, or equivalently the RF phase $\varphi = 2\pi t/T_{\mathrm{RF}}$, a signal is detected behind the slit. The RF system in the PKAT beamline is based on a MAMI-type deflecting cavity operating at 2.449 GHz, equivalent to a period of a $T_{\mathrm{RF}} = 408\,\mathrm{ps}$. During the period of the RF, the signal passes the slit twice, first at 0° and then at 180°.

Since the integration time is much longer than the recombination time, one must consider the contribution of the charges at each half period. Thus, the observed signal is the sum of all the contributions at

$$t_n = n\,\frac{T_{\mathrm{RF}}}{2} \tag{5.8}$$

therefore,

$$I'(t) = \sum_{n=0}^{\infty} I\left(t + n\,\frac{T_{\mathrm{RF}}}{2}\right). \tag{5.9}$$

Inserting Eq. 5.6 into Eq. 5.9, and switching the order of summation will lead to

$$I'(t) = \sum_{k=1}^{\infty}\sum_{n=0}^{\infty} A'_k \exp\left[-\frac{1}{\tau_{\mathrm{rec}}}\left(t + \frac{nT_{\mathrm{RF}}}{2}\right)\right] \exp\left[-\left(\frac{k\pi}{d}\right)^2\left(t + \frac{nT_{\mathrm{RF}}}{2}\right)D\right] \tag{5.10}$$

Reorganizing the exponential terms differently results in

$$I'(t) = \sum_{k=1}^{\infty}\sum_{n=0}^{\infty} A'_k \exp\left[-t\left(\frac{1}{\tau_{\mathrm{rec}}} + \left(\frac{k\pi}{d}\right)^2 D\right)\right] \exp\left[-n\frac{T_{\mathrm{RF}}}{2}\left(\frac{1}{\tau_{\mathrm{rec}}} + \left(\frac{k\pi}{d}\right)^2 D\right)\right]$$

For a fixed value of k, the sum over n is a geometric series, defined by a constant ratio of subsequent summands. Defining q_k as

$$q_k = \frac{s_{n+1}}{s_n} = \exp\left[-\frac{T_{\mathrm{RF}}}{2}\left(\frac{1}{\tau_{\mathrm{rec}}} + \left(\frac{k\pi}{d}\right)^2 D\right)\right] \tag{5.11}$$

where the sum of the geometric series is given by

$$\sum_{n=0}^{\infty} s_n = s_0 \frac{1}{1-q_k}. \tag{5.12}$$

Therefore, the signal observed during the experiment can be simplified into

$$I'(t) = \sum_{k=1}^{\infty} A'_k\,\frac{1}{1-q_k} \exp\left[-t\left(\frac{1}{\tau_{\mathrm{rec}}} + \left(\frac{k\pi}{d}\right)^2 D\right)\right]. \tag{5.13}$$

Introducing $A_k^\star$ as

$$A_k^\star = A_k' \frac{1}{1-q_k}, \tag{5.14}$$

the observed signal can be expressed as

$$I'(t) = e^{-t/\tau_{\mathrm{rec}}} \sum_{k=1}^{\infty} A_k^\star \exp\left[-t\left(\frac{k\pi}{d}\right)^2 D\right]. \tag{5.15}$$

Equation 5.15 has the same form as Eq. 5.6, with the exception of the modification of the coefficients A_k', which are replaced with $A_k^\star$. Equation 5.15 indicates that the observed current at each point in time, $I'(t)$, is therefore slightly higher than the $I(t)$ in which only the finite recombination time was included into the diffusion model. This modification is insignificant for large values of k, as q_k will approach zero.

In Fig. 5.4, the red curve shows an experimentally observed impulse response of the bulk GaAs photocathode used in the course of this project. The pulse response was obtained at $QE = 0.37\,\%$ with an excitation wavelength of 800 nm and fitted by the diffusion model.

The observed pulse response is a convolution of the diffusion model prediction and a Gaussian function. The Gaussian function depends on the experimental parameters and is defined by its σ, which is the time resolution of the apparatus. The fit to the experimentally observed signal is found by free parameters of the diffusion model, namely, the diffusion constant D, the absorption coefficient α, and the recombination time τ_{rec}, as well as by the apparatus time resolution σ. The active layer thickness of the cathode is chosen as a fixed parameter, $d = 0.05\,\mathrm{cm}$. Each of the free parameters are not completely free but must be in reasonable agreement with the accepted physical values. The results of the diffusion model calculations with the given fixed and free parameters are plotted with solid blue and green lines in Fig. 5.4. The peak of the pulse is normalized to 1 and shifted to $t = 0$.

The blue curve shows a fit of the diffusion model considering only the finite recombination time, Eq. 5.6. The green curve illustrates the modified diffusion model corrected for the effect of the contributions of each half period according to Eq. 5.15 with the same fit parameters as the blue curve. The extracted parameters, which are listed in Table 5.1, are in reasonable agreement with the literature values for such a highly doped semiconductor [21, 22, 26, 121]. The exact doping concentration of the photocathode in this project is not known, therefore, an uncertainty in the obtained fit parameters exist.

Regarding the two diffusion model fits, a few comments merit some elaboration. First, as expected, the observed current at each time according to Eq. 5.15 is slightly higher than $I(t)$. For the obtained parameter sets, the correction is rather small, as observed by the different fits in Fig. 5.4. Furthermore, from Eq. 5.9, it is obvious that the effect of the periodic deflection is insignificant for signals which

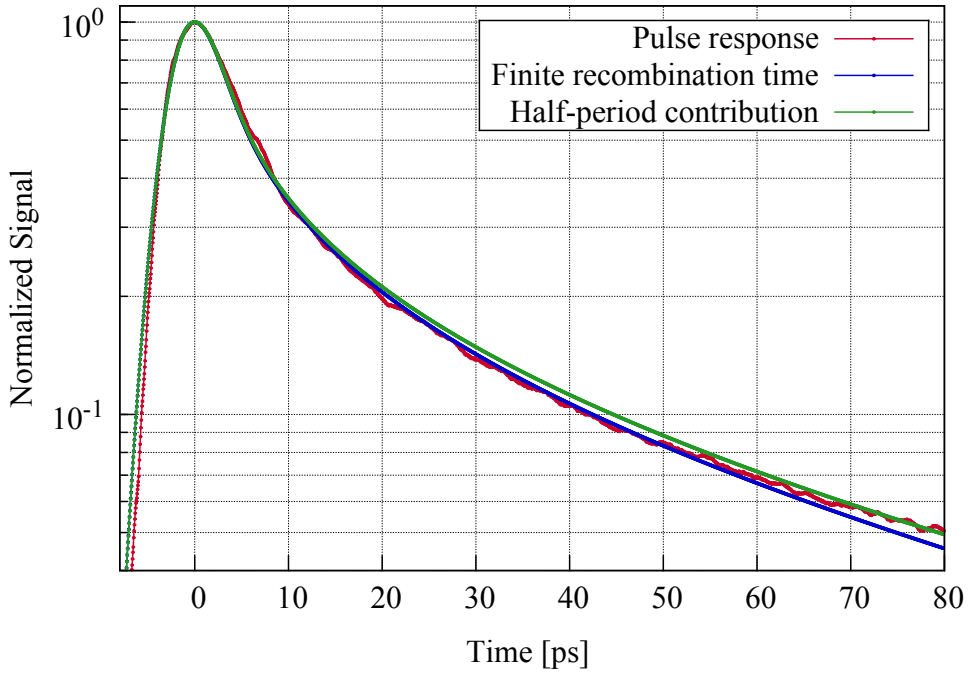

Figure 5.4: In red, pulse response of bulk GaAs at $QE = 0.37\,\%$ is shown. Blue and green curves are the result of the diffusion model fit according to equations 5.6 and 5.15. The blue curve includes the finite recombination time. The green curve is the modified solution to the diffusion model by taking into consideration both the finite recombination time and the contributions of the pulses at each half period.

decay on single-digit picosecond timescales. However, for the pulses from the bulk GaAs which decay at a time scale comparable to half the period of the deflector, ($T_{\mathrm{RF}}/2 = 204$ ps), it is not completely negligible.

By introducing a cutoff time, the observed signal can be approximated:

$$I_{\mathrm{obs}} = \sum_{n=0}^{\infty} I(t + nT_{\mathrm{RF}}/2) \approx \sum_{n=0}^{T_{\mathrm{cutoff}}} I(t + nT_{\mathrm{RF}}/2) \tag{5.16}$$

A reasonable choice for the cutoff time is $T_{\mathrm{cutoff}} = 10\,\ln(10)\,\tau_{\mathrm{rec}}$. Inserting τ_{rec} from the fit of the diffusion model, one obtains $T_{\mathrm{cutoff}} \approx 4\,\mathrm{ns}$. In addition, an exponential decay with a time constant τ_{rec} represents an upper limit for the pulse profile. Thus, this choice illustrates that the errors resulting from the periodic re-excitation with the 76 MHz laser (period of 13.1 ns) are negligible, since the signal has already decayed to less than 10^{-10} of its initial value after approximately 4 ns.

Equations 5.6 and Eq. 5.15 are a sum of exponential functions and as such are not exponential functions by themselves. In each of these equations, the number

Table 5.1: The extracted fit parameters from the diffusion model.

Parameter	**Notation**	**Value**
Recombination time	τ_{rec}	$(160.3 \pm 144.1)\,\mathrm{ps}$
Diffusion constant	D	$(13.6 \pm 9.9)\,\mathrm{cm^2\,s^{-1}}$
Absorption coefficient	α	$(20\,501 \pm 7456)\,\mathrm{cm^{-1}}$
Time resolution	σ	$(1.78 \pm 0.23)\,\mathrm{ps}$

of summands contributing to the current decreases with time. The time scale $t_{\mathrm{exp}} = d^2/D\pi^2$ is defined so that the exponent in the summation of equations 5.6 and 5.15 becomes 1 for $k = 1$. After t_{exp}, the response will be dominated by the first term only since the relative contribution of the following terms will quickly diminish and can be disregarded. This result means for $t > t_{\mathrm{exp}}$, the response is approximately exponential with a time constant t_{exp}. For the bulk GaAs, in our case, $t_{\mathrm{exp}} \approx 18\,\mu\mathrm{s}$.

One must note that for a strained superlattice, with the same diffusion constant and active layer thickness of $d = 0.1\,\mu\mathrm{m}$, t_{exp} is approximately 0.7 ps. The time required until the response becomes exponential scales with d^2. Therefore, as d increases, so does the decay of the pulse response. This relationship, in turn, leads to the undesirable long tails of the time response in the bulk GaAs, known as the longitudinal halo. Longitudinal halos cause beam loss in the accelerator. For the application of high-current electron accelerators, the longitudinal halo must be minimized. The large active layer thickness of the bulk GaAs makes these NEA cathodes rather unsuitable to produce a small longitudinal halo. Alternatively, one can use thin layer GaAs-based photocathodes such as superlattices which can easily be purchased [8]. Superlattices have a very thin active layer and therefore, can generate fast pulses with much smaller longitudinal halo.

Apart from the effect of the convolution with the time resolution of the apparatus, one would expect an exponential decay of the pulse response, as observed in [17] when using the bi-alkali-antimonide compound K_2CsSb, which is a positive electron affinity cathode. In Chapter 6 the pulse response of GaAs/GaAsP SSL and K_2CsSb are compared.

It is worth noting that the thin photocathodes such as strained superlattice, in which the mean free path ($\approx 70\,\mathrm{nm}$) is a fraction of the active layer thickness of about 100 nm, cannot be adequately described by a diffusion model. Since the condition of $\lambda \gg d$ is not met in SSL, many of the photoexcited electrons are emitted from the cathode before the necessary interactions for the diffusion take place. Therefore, in order to describe the pulse response of SSL mathematically, a superposition of interaction-free (ballistic) emission and diffusion must be used [10, 107].

To conclude this section, one must note that in Fig. 5.3, the pulse intensity at negative times is not zero. This remarkable occurrence is an experimental artifact

which merits some discussions here. The intensity at $t < 0$ results from the periodic deflection of the beam and the contribution of the charges at each half period. The pulse detection samples charge at each half period; thus, the observed signal is the sum of all these contributions. These points have suffered from the long emission time, and therefore, their contribution is much less than the points at $t = 0$. The initial intensity at $t < 0$ and each of the following intensities added at each half period is minimal. Modelling the pulse response with the diffusion model explains the observed intensities at negative times.

5.7 Investigation of the low QE

In one of the recent studies of pulse response of bulk GaAs at 800 nm conducted in the PKAT laboratory, the shape of the pulse was speculated as dependent on the *QE* [34]. The aforementioned measurement was performed at $QE \approx 0.05\,\%$. Therefore, the time response measurements of the GaAs photocathode were important in order to verify whether the *QE* has an effect on the shape of the time response, especially at very low *QE* values. For this purpose, after activating the photocathode, the *QE* and the pulse response measurements were conducted daily. In Fig. 5.5, the changes of the *QE* over the measuring period is shown.

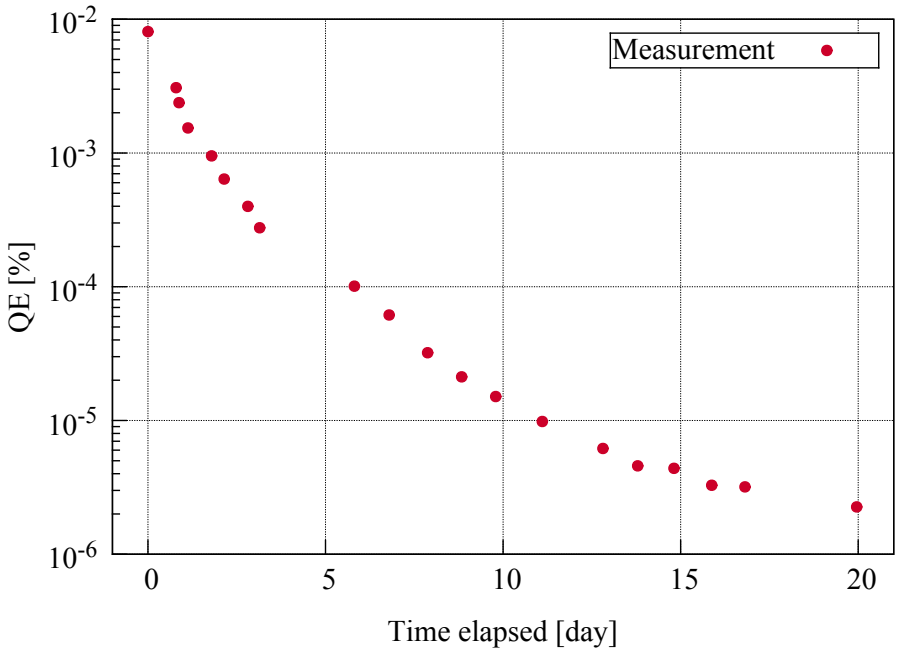

Figure 5.5: Measured *QE*s of bulk GaAs Cathode1 for the period of 20 days.

The *QE* immediately after the activation was $8.09 \times 10^{-3}\,\%$, and the investigation was terminated at a *QE* of $2.26 \times 10^{-6}\,\%$. The results of the pulse response measurements during the 20 days of measuring period are illustrated in Fig. 5.6.

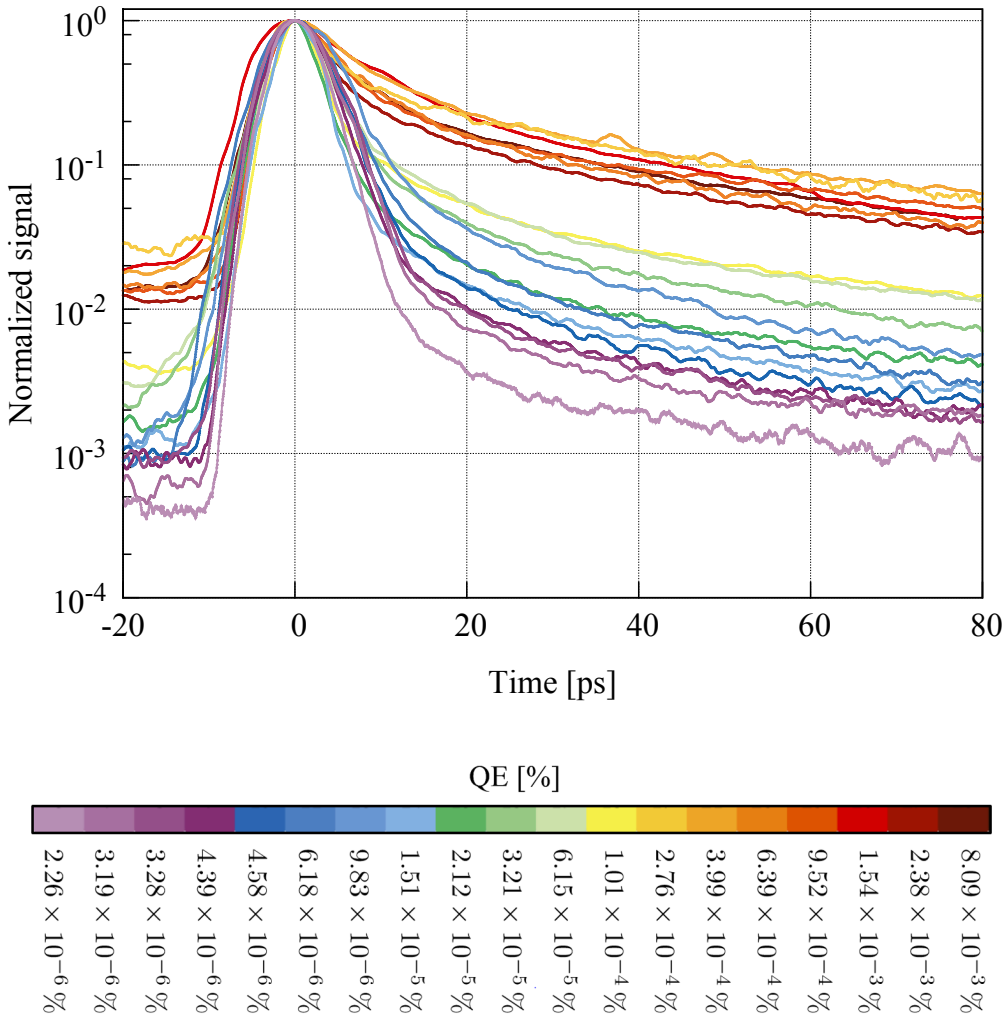

Figure 5.6: The upper graph displays pulse responses of the GaAs Cathode1 measured for a period of 20 days. The color scheme represents the decay of the *QE* in a descending order from 8.09×10^{-3} % to 2.26×10^{-6} %. The general trend in the pulse responses is such that the intensity of the halo decreases as the *QE* drops.

The pulses of higher *QE* are on the upper section of Fig. 5.6 and descend to pulses of lower *QE* in the lower section. The color code illustrates the decay of the *QE* in a descending order from right to left corresponding to *QE*s ranging from 8.09×10^{-3} % to 2.26×10^{-6} %. At each moment in time, as the *QE* decreases, the intensity of the detected signal may not necessarily decrease. These fluctuations are attributed to the experimental difficulties. However, of paramount importance is that the general trend is such that the halo intensity decreases as the *QE* drops.

These measurements were repeated with the new bulk GaAs, Cathode2 and a similar pattern was observed.

In order to explore the dependency of the intensity on quantum efficiency, the respected intensities at an arbitrary time of 60 ps as a function of *QE* are plotted in red in Fig. 5.7. Similar measurements with bulk GaAs Cathode2 after the 2nd activation were repeated. The pulse responses were obtained between a *QE* of 5.81 % and 4.94×10^{-6} % (see Fig. 5.2 for the *QE* degradation). The related intensities at 60 ps for Cathode2 are shown in blue in Fig. 5.7.

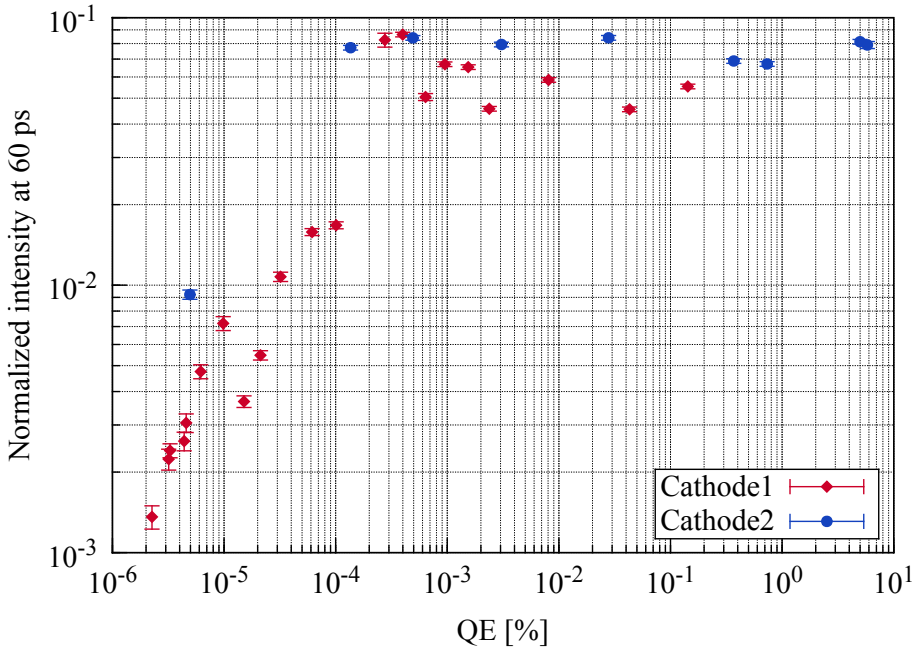

Figure 5.7: Measured normalized intensities at an arbitrary time of 60 ps as a function of *QE* for the two different bulk GaAs cathodes. The data in red and blue are the results from the old and the new GaAs photocathode, respectively.

As seen in Fig. 5.7 the normalized intensity at 60 ps is relatively constant from high *QE*s to *QE*s as low as approximately 10^{-4} %. In that range, the intensity ratio changes by only approximately 20 % and 50 % for Cathode2 and Cathode1, respectively. The dramatic change on the dependency of the normalized intensity on *QE* occurs at *QE*s below 10^{-4} %. The findings in Fig. 5.7 show that the intensity of the photoexcited electrons is strongly affected by the *QE* as the *QE* drops to very low values. For Cathode1, a drop of almost 2 orders of magnitude is observed.

Two possible explanations exist for the behavior of the halo at *QE*s in the order of 10^{-4} % and lower, *the surface charge limit* (SCL), otherwise known as *surface photovoltage effect* (SPV), and *the positive electron affinity* (PEA). Although the resultant impact of these two effects on the transport of the photoexcited elec-

trons from the bulk of the semiconductor to the surface and their diffusion into the vacuum seem similar, these two processes are profoundly different in nature. Therefore, each effect will be discussed in detail in the following sections.

5.7.1 Surface photovoltage effect

In general, a photovoltaic effect consists of an illumination-induced change in the potential distribution of the structure under study. The change in the potential can typically arise because of the transfer of some charge, a net charge redistribution, or a combination of both in the given structure. The photovoltaic effect was first reported in 1953 by *Brattain* [23]. Surface photovoltage is a specific variant of the photovoltaic effect in which the surface-potential changes as the surface is illuminated.

Some of the basic properties of semiconductor surface that lead to the SPV are important to review.. The periodic structure of an ideal crystal results in the formation of the allowed valence and conduction bands separated by the forbidden energy gap. The termination of this periodic structure, plus additional phenomena such as dangling bonds, surface reconstruction or relaxation, impurity atoms adsorbed on the surface, etc., may cause surface-localized states and/or surface dipoles to appear within the bandgap.

The appearance of the surface states, which have a net positive charge and act as trapping centers, induce charge transfer between the bulk and the surface, which results in the development of the surface space charge region, SCR. The existence of the SCR implies an electric field, and therefore, a potential drop across the region. The electric field in the SCR causes excess electrons to be deflected away from the surface. A simplified schematic diagram showing the development of surface photovoltage is illustrated in Fig. 5.8.

When an NEA cathode is illuminated with a laser pulse with energy slightly above the bandgap energy, photoexcited electrons reach the conduction band and leave the holes in the valence band, process ① in Fig. 5.8. A fraction of the electrons rapidly thermalize by electron-phonon scattering, process ②, diffuse to the surface, surmount the surface barrier, escape to the vacuum, and contribute to the measured *QE*, process ③. On their way to the surface, a portion of the photoexcited electrons recombine with the holes in the valence band, process ④.

If, however, a large number of electrons reach the photocathode surface at the same time, the electric field in the SCR sweeps away the excess of electrons from the surface, and a large buildup of electrons are trapped in the BBR, process ⑤. These trapped electrons will produce an opposing field, and therefore, suppress the emission of the electrons arriving at a later time.

This serves to reduce the density of surface-trapped electrons, which leads to the flattening of the band bending. Consequently, the work function at the cathode surface increases, leading to a reduction of NEA, which causes the development of surface photovoltage denoted as U_{SPV} in Fig. 5.8.

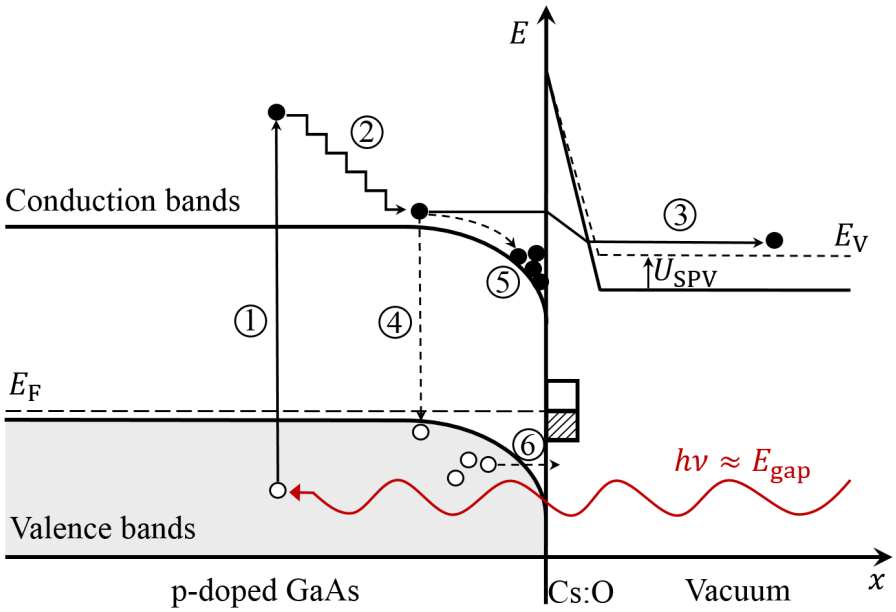

Figure 5.8: Schematic illustration of the surface photovoltage buildup. The numbers indicate different processes in development of surface photovoltage, see the description in the text. The full and empty circles represent the electrons and holes, respectively.

The effect of the SPV phenomena can be minimized in two ways. First, the effect can be reduced by tunneling of the electrons and recombination with the holes. This is referred to as tunneling current. This is realized, on one hand, with high p-doping. When the p-doping is high, the BBR is narrow enough to allow the tunneling, and consequently the trapped electrons recombine faster with the holes. One can visualize this scenario by considering the holes tunneling into the surface. Conversely, when p-doping is low, the photovoltage increases at a higher rate and to a higher degree. On the other hand, having highly occupied surface states strengthens the tunneling of the holes current, and therefore, prevents the buildup of the photovoltage and the SCL effect. The density of surface states depends on surface quality and the activation layer.

Second, the effect of SPV can be minimized by tunneling of the valence band holes against the surface barrier with thermal fluctuations. This can be realized if the width of the BBR is small. When the BBR is narrow, holes can easily overcome the barrier and recombine with the trapped electrons. This is known as thermionic current.

These two channels of holes arriving at the surface, process ⑥, help restore the current, although not to the point of neutralizing the SCL. The strength of these restoring currents determines the rate at which the vacuum level recovers its original value. For photocathodes with sufficiently high p-doping concentration levels of

greater than $10^{18}\,\mathrm{cm}^{-3}$ [53], the tunneling current is the most dominant process against the buildup of any photovoltage and the charge limit effect [124]. Operating with a high-doping-density cathode, which allows a much shorter restoring time, is indispensable in mitigating the SCL effect.

Several papers shed light on the physical description of the SCL phenomenon. The above summary is loosely based on the discussions in [53, 79, 124].

The response of a cathode depends on different parameters and mainly on the surface condition, the photoexcitation wavelength and the electric field applied [101]. Throughout our measurements, both the laser wavelength and the electric field were kept at fixed values, and therefore, the effects of their variations on the pulse response will not be discussed here.

Referring to Fig. 5.6, at first, immediately after the activation, the cathode surface is clean, NEA, and therefore, the *QE* is high. Consequently, the cathode is capable of producing a sufficient current without requiring intense optical excitation. As a result, at the start of the laser pulse, the photocathode response follows the shape of the laser pulse, rising to a peak. Then, its response will follow the behavior shown in Eq. 5.6. It must be noted that the rise in the pulse response cannot be infinitely sharp due to the limitations of the time resolution and the transit time spread.

As time elapses, the surface conditions change for the worse, and the *QE* drops. In order to produce the same amount of current, according to Eq. 2.1, more intense laser light is needed. At high illumination intensities, the photovoltage saturates faster and to a higher degree, which results in the rising of the vacuum level. The SPV causes a change of equal magnitude in the surface work function. Thus, the photoexcited electrons face a larger barrier to escape. Consequently, their escape probability and thus the photoemitted current is suppressed. This occurrence explains why in Fig. 5.6 the tail of the pulse response drops lower as the *QE* continues decreasing. In this situation, the extracted current is no longer proportional to the laser intensity due to the charge limit.

A representative example, in which the emission current dependence on the excitation laser intensity was investigated, is shown in Fig. 5.9. In the low-intensity region, as the laser pulse intensity increases, the emitted photocurrent increases almost linearly. Further increase in the laser intensity results in an increasingly nonlinear behavior, followed by a saturation of the photoemitted current. The maximum emitted current is less than the space charge limit of approximately 600 electrons/pulse. This saturation is the direct result of the surface charge limit effect.

The slope of the fits to the data points is obtained. The data points in the region $P_{\mathrm{laser}} < 100\,\mathrm{nW}$ and $I < 10\,\mathrm{pA}$ are excluded in the fit due to the large uncertainties in this extreme low intensity and current region. In addition, the last eight data points in the upward bending of the curve 12 are excluded in the fit, as the significant heating of the cathode may have affected these points. These data points are shown in red circles. In Table 5.2, the slope of the fits, together with the respected *QE* for each set of data, are presented. It must be noted that a considerable uncertainty in the value of the slopes exists, estimated in the order

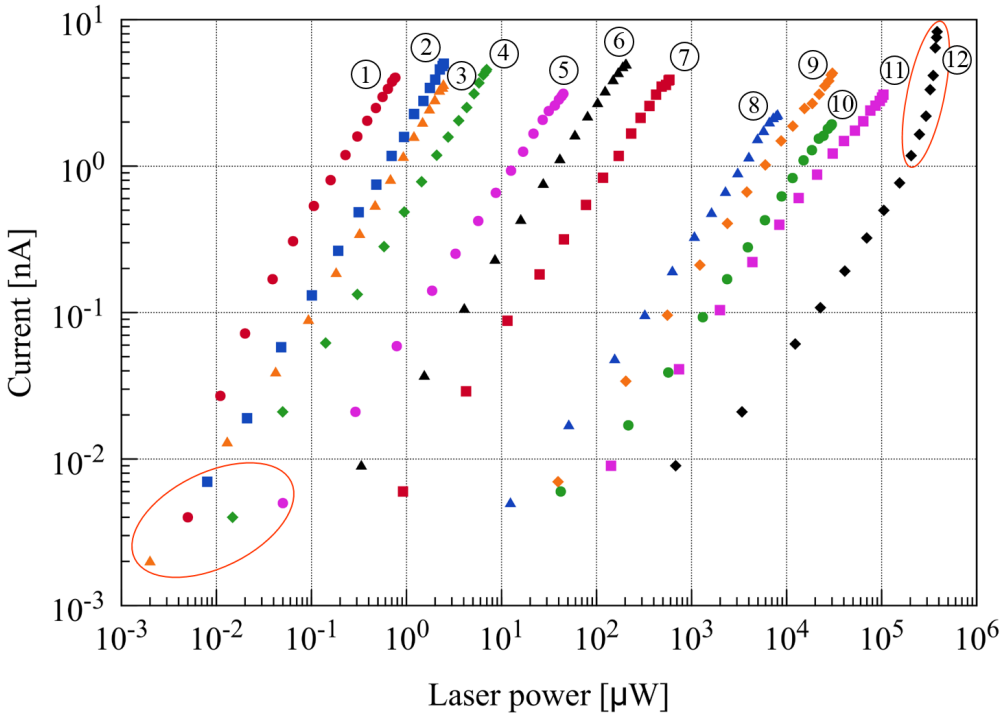

Figure 5.9: Electron emission current as a function of the DC-laser intensity at 800 nm. The data were taken in *QE* ranging from 2.44 % to 4.86×10^{-6} %. The *QE*s are in descending order from left to right. The slope of the curves are gathered in Table 5.2. The data points in the red circles are excluded in the fit, see the text for explanation.

of 10 %. For each set of measurements, the laser power has changed a few orders of magnitude. Therefore, one cannot be certain of the accuracy in determining the laser power over such a large variation. According to the fits, as the *QE* decreases, the slopes of the curves are gradually decreasing. The reduction of the slopes are attributed to the surface photovoltage which leads to the suppression of the current as the *QE* decays.

As the *QE* drops further, so does the charge limit. The effect of *QE* on charge limit for excitation wavelengths of 775 nm and 865 nm was investigated [124]. In both cases, as *QE* dropped from 1 % to 0.1 %, a decrease of almost 80 % was observed for the charge limit. This observation means that as the *QE* drops below a critical value, the maximum extracted current is dictated by the intrinsic properties of the photocathode instead of by the space charge limit. The total extracted current tends to saturate to a limit significantly lower than what the space charge limit allows according to the *Langmuir-Child* law [53, 124].

Table 5.2: Results of the fit to the measurement data illustrating the extracted current dependence on the laser intensity. Depending on the *QE*, the slope of the fit changes. The numbering is according to the curve numbers in Fig. 5.9. A 10 % uncertainty in the extracted slopes is assumed due to measuring over a large laser power variation, see the text.

Number	*QE* %	**Slope**
(1)	2.44	1.130 ± 0.022
(2)	7.54×10^{-1}	1.151 ± 0.007
(3)	5.42×10^{-1}	1.093 ± 0.011
(4)	2.16×10^{-1}	1.095 ± 0.006
(5)	3.37×10^{-2}	0.994 ± 0.006
(6)	8.36×10^{-3}	0.995 ± 0.006
(7)	2.66×10^{-3}	1.002 ± 0.006
(8)	1.00×10^{-4}	0.963 ± 0.006
(9)	6.60×10^{-5}	0.963 ± 0.008
(10)	2.47×10^{-5}	0.928 ± 0.016
(11)	1.25×10^{-5}	0.874 ± 0.010
(12)	4.86×10^{-6}	0.835 ± 0.042

The surface charge limit effect imposes a great challenge in producing highly polarized electron beams for the operation of accelerators such as SLC[1] [6] and the NLC[2] [97]. Furthermore, in experiments which require a high electron beam intensity, the SCL presents a huge difficulty [123]. The demand for obtaining the highest polarization mandates near band gap photoexcitation of an NEA cathode, which has a low absorption region. Unfortunately, while operating at these wavelengths, the buildup of the SCL does not allow high-power excitation. Therefore, the properties of NEA cathodes under intense excitation are hard to investigate [96, 98].

According to Fig. 5.7, the critical value for *QE* is estimated at approximately 10^{-4} %, and as the *QE* drops to values around 10^{-4} %, the extracted normalized current at 60 ps remains almost constant. Further decrease in *QE* results in a dramatic decrease in the extracted current due to the buildup of the surface charge limit resulting from the intense optical excitation.

Next, the presence of SPV in this experiment is investigated. The number of photons entering the semiconductor[3] required to create a photoemitted bunch with n_e electrons is

[1]Stanford Linear Collider, *Stanford, CA*
[2]Next Linear Collider, *Stanford, CA*
[3]The reflection at the surface is unimportant for this consideration.

$$n_\gamma = \frac{n_e}{QE} \tag{5.17}$$

Each photon is converted into electron in the valence band of which the majority (characterized by $0.5 < f < 1$) will reach the surface at the reference time of 60 ps. Apart from a small fraction of electrons which are photoemitted at the beginning of the pulse, the electrons will become localized in the surface states. This localization compensates for the positive charges in the band bending region at the surface, in turn, creating a surface photovoltage U_{SPV} which causes upward band bending or, equivalently, an increase of the electron affinity.

The effect is modeled by treating the process as the charging of a capacitor. The surface capacitance per unit area is estimated as

$$C_A = \frac{\epsilon_0\, \epsilon_{\mathrm{GaAs}}}{d_{\mathrm{BBR}}} \tag{5.18}$$

where ϵ_0 and ϵ_{GaAs} are the permittivity of vacuum and of GaAs, respectively, and $\epsilon_{\mathrm{GaAs}} \approx 13$. d_{BBR} is the thickness of the band bending region, which is within the range of the $d_{\mathrm{BBR}} \approx 10\,\mathrm{nm}$ for doping level in the order of $10^{19}\,\mathrm{cm}^{-3}$.

Combining equations 5.17 and 5.18 will yield the following equation for the surface photovoltage

$$U_{\mathrm{SPV}} = \frac{f e\, n_e\, d_{\mathrm{BBR}}}{QE\, \epsilon_0\, \epsilon_{\mathrm{GaAs}} \pi \sigma_L^2} \tag{5.19}$$

with e as the elementary charge and $\pi\sigma_L^2$ as the illuminated area of the cathode. The latter is a good approximation equivalent to the area where the charge is accumulated at the surface because the lateral diffusion of carriers is in the order of micrometers and is much smaller than $\sigma_L \approx 160\,\mu\mathrm{m}$ in this case.

For our experimental conditions, for a photoemitted current of $I = 1\,\mathrm{nA}$ and assuming $f = 0.5$ and $n_e = 80$, the SPV is expressed numerically as

$$U_{\mathrm{SPV}}[V] = 7.0 \times 10^{-9} \frac{1}{QE} \tag{5.20}$$

For $QE < 10^{-6}\,\%$, the energy eU_{SPV} is clearly no longer negligible against the electron affinity.

Next, an explanation is in order for the modification of the pulse shape observed in Fig. 5.6. When the laser intensity is low, the transport can be explained by considering the mean free path of the electrons. However, in the case of high intensity, the transport process goes through rapid dynamic changes in the order of a few picoseconds, which leads to self-modulation of the photoemission.

A first assumption is that the diffusion current in the bulk towards the surface is still proportional to the photoemission without SPV. This assumption would mean that after an initial charging of the surface during the first few picoseconds, the electrons which arrive later will see a modified barrier, corresponding to a *pump-probe* experiment. In a pump-probe experiment, a short and intense "pump" pulse

excites the system. After an adjustable delay time, a low intensity "probe" pulse is used to probe the effect of the first excitation. Changing the delay between the pump and the probe, and measuring the system response to the probe allow reconstructing the evolution of the excitation from the pump and investigating the ultrafast phenomena inside the system.

In our case, this process is "continuous", therefore, the pump-probe is only an approximation. However, the first 10 ps can be considered as the "pump" period in which majority of the electrons ($\approx 90\,\%$) have arrived and are contributing to the pump. Since the long range behavior (> 10 ps) is of main interest, the electrons which arrive at the surface at times $t > 10$ ps can be treated as "continuous probe". In other words, high-intensity excitation by the laser creates an enormous charge at the surface. Then, the pulse, by itself, results in the steering of the electrodynamics mechanisms for the electron transport in the crystal and their emission into the vacuum. This process is a self-modulation of the photoemitted electron bunches at the picosecond timescale.

In the pump-probe experiment, a time constant τ_{SPV} characterizes the discharge of the surface voltage after the pump process. For doping levels similar to our regime, τ_{SPV} is in the order of a few nanoseconds, according to the determination established in [79]. Since $t \ll \tau_{\mathrm{SPV}}$ in our experiment, the surface condition can be considered as static around the reference time scale of our experiment.

When comparing the low *QE*s to the initial higher *QE* values, the increased potential barrier resulting from the surface photovoltage decreases the emitted intensity —which is created by the thermalized electrons diffusing to the surface— by the Boltzmann factor. In analogy to thermionic emission, this occurrence leads to a simple prediction for the emitted intensity, R:

$$R = R_0 \cdot e^{-kU_{\mathrm{SPV}}} \tag{5.21}$$

where R_0 is the yield with no photovoltage effect and $k = e/k_{\mathrm{B}}T$, where k_{B} denotes the Boltzmann constant, and T is the temperature. In the above equation, the affinity is assumed to be close to zero for the low *QE*s relevant to our measurements. In the general case, where $\chi \neq 0$, Eq. 5.21 can be written as

$$R = R_0 \cdot e^{-k[U_{\mathrm{SPV}}+\chi]} \tag{5.22}$$

Mulhollan et al. have derived a formula [79] which takes into account finite negative values of affinity:

$$\frac{R}{R_0} = 1 + k_1 \cdot \ln\left[1 - \left(1 - e^{-U_{\mathrm{SPV}}/k_2}\right) e^{-t/\tau_{\mathrm{SPV}}}\right] \tag{5.23}$$

where k_1 and k_2 are constants which depend on the affinity, the amount of band bending, and the Schottky barrier lowering.

As mentioned, $t \ll \tau_{\mathrm{SPV}}$ in our experiment; thus, the time-dependent factor can be omitted. In this case, the expression simplifies to

$$R = R_0 \left(1 - \frac{k_1}{k_2} U_{\mathrm{SPV}}\right) \tag{5.24}$$

By fitting Equations 5.21 and 5.24 to the data in Fig. 5.7, one can obtain the corresponding values for the best fit. The results are plotted in Fig. 5.10.

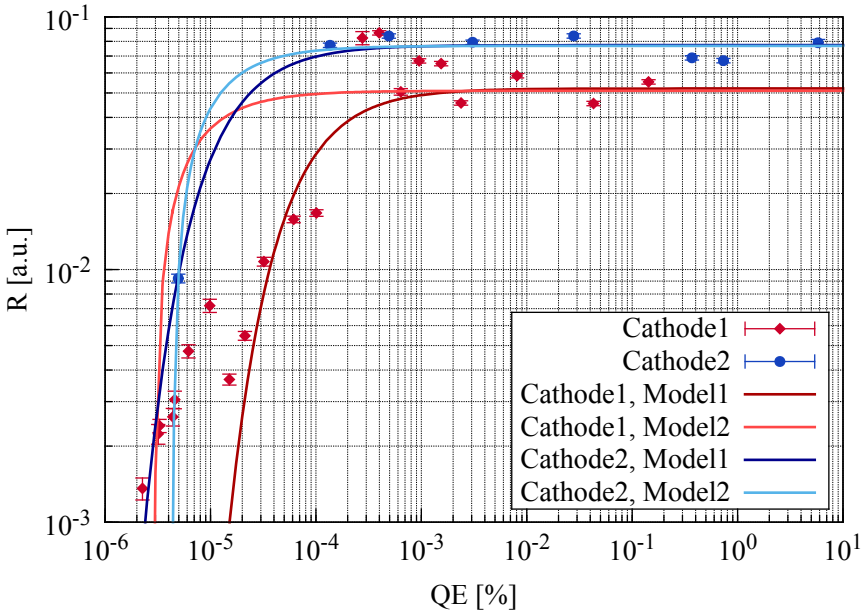

Figure 5.10: The relative intensity at 60 ps for the two different bulk GaAs along with the best fit curves according to Eq. 5.21 (Model1) and Eq. 5.24 (Model2). The related fit parameters are gathered in Table 5.3.

In Fig. 5.10, the fits according to Eq. 5.21 are shown in dark red and blue curves and are referred to as Model1. The light red and blue curves represent the fits according to Eq. 5.24 and are referred to as Model2. When obtaining the fit for Cathode1 using Model2, R_0 is kept at a fixed value of 0.05. The fit parameters are presented in Table 5.3. In the fit equations, $U_{\mathrm{SPV}} \propto 1/QE$, and in Eq. 5.24, for simplicity, the factor k_1/k_2 is replaced with k.

Table 5.3: Fit parameters according to the two models for the two bulk GaAs

		Cathode1		**Cathode2**	
Model	**Equation**	R_0	k	R_0	k
1	$R = R_0 \cdot e^{-k/QE}$	0.05	5.98×10^{-5}	0.08	1.04×10^{-5}
2	$R = R_0\,(1 - k/QE)$	0.05	2.91×10^{-6}	0.08	4.35×10^{-6}

Both predictions, Equations 5.21 and 5.24, yield a constant R_0 at large QEs, although neither prediction fits the data exactly. According to the results, both

models fit the data from the new bulk GaAs, Cathode2, reasonably well, delivering an $R_0 = 0.08$. For Cathode1, the models deliver lower values of $R_0 = 0.05$, and the models do not seem to describe the data well. This mismatch to the models is possibly a result of our data suffering from fluctuations as a result of the experimental difficulties. Nevertheless, the observed pulse responses in Fig. 5.6 demonstrate that the effect of self-modulation exists.

The discrepancies between the models and the data may be a result of the aforementioned assumptions that are only partially fulfilled. It is possible that during the experiment the affinity was changing, and thus, at the relevant *QE*s the affinity assumed a slightly positive value, see the discussion in the following section. In addition, the surface is continuously pumped, causing the conditions for a pump-probe experiment not to be completely fulfilled. Moreover, in case of the extremely low *QE*s the average power of the laser was already quite high, and a great portion of the laser power converts to heat. As a result, high laser illumination might have led to the rise of photocathode temperature, which enhances the decay of *QE* [56], see discussion in Section 2.3.2.

To complete the discussion of the SCL, an elaboration of several important comments is necessary.

One way to circumvent the SCL problem is through the use of a highly p-doped superlattice or SSL. *Togawa et al.* [130] have investigated the SCL phenomenon for three types of SL photocathodes under the same conditions of the laser and electron source operations, using a 70 keV gun. They confirmed that for both GaAs-AlGaAs superlattice and InGaAs-AlGaAs strained superlattice with the high surface doping of $4 \times 10^{19}\,\mathrm{cm}^{-3}$ the SCL phenomenon was not observed, even at the low *QE* values. However, when a medium level of p-doped GaAs-AlGaAs superlattice was used, $5 \times 10^{18}\,\mathrm{cm}^{-3}$, the SCL was observed at low *QE*s. This result is expected because as the high surface p-doping decreases, the width of the BBR increases. This increase in turn decreases the valence hole tunneling, one of the major physical mechanisms in overcoming SCL.

Another important factor influencing the SCL is the source voltage. This effect has been explored by *Tang et al.* [122]. According to [122], for the excitation wavelength of 850 nm, surface charge limit dropped from $\sim 7.6 \times 10^{10}$ electrons/pulse to $\sim 3.6 \times 10^{10}$ electrons/pulse as the source voltage was decreased from 120 kV to 60 kV. The data clearly demonstrated a strong and almost linear dependence of the SCL on the cathode bias voltage. The decrease in surface charge limit for lower source voltage is also due to the *Schottky effect*. This result is especially important in our research. Our source bias voltage was set at 45 keV and the laser wavelength at 800 nm; according to the findings in [122], the charge limit is estimated to drop by almost 60 %, had we had the source operating at its original design value of 100 keV. At 45 keV, SCL is reached much faster, and therefore, the impact of the SCL on our measurements are higher.

5.7.2 Positive electron affinity

The second possible explanation as to why the tail of the pulse response drops when the *QE* decreases is the fact that the properties of the photocathode surface changes as the *QE* decays.

Recalling that the bandgap energy for bulk GaAs is $E_{\text{gap}} = 1.42\,\text{eV}$, a photoexcitation with the 800 nm laser, $E = 1.55\,\text{eV}$, equates to an energy surplus of 0.13 eV for the electrons reaching the conduction band. As the NEA decreases, the vacuum energy level increases by the same amount. As long as the photoexcited electrons energy is above the NEA level, the electrons will exit the cathode and contribute to the *QE*.

As the GaAs photocathode degrades, the NEA decreases. Thus, the probability of the transmission due to quantum mechanical transitions reduces, and the *QE* drops. Since the shape of the pulse is governed by the properties of the cathode itself, and not by the properties of the surface, the shape of the pulse remains the same, as seen in Fig. 5.6. As the time elapses, and the cathode continues to degrade, at some stage the NEA reaches a point where $\chi = 0$, or even positive, χ_{PEA}. A schematic diagram showing the χ_{PEA} for the GaAs semiconductor is shown in Fig. 5.11.

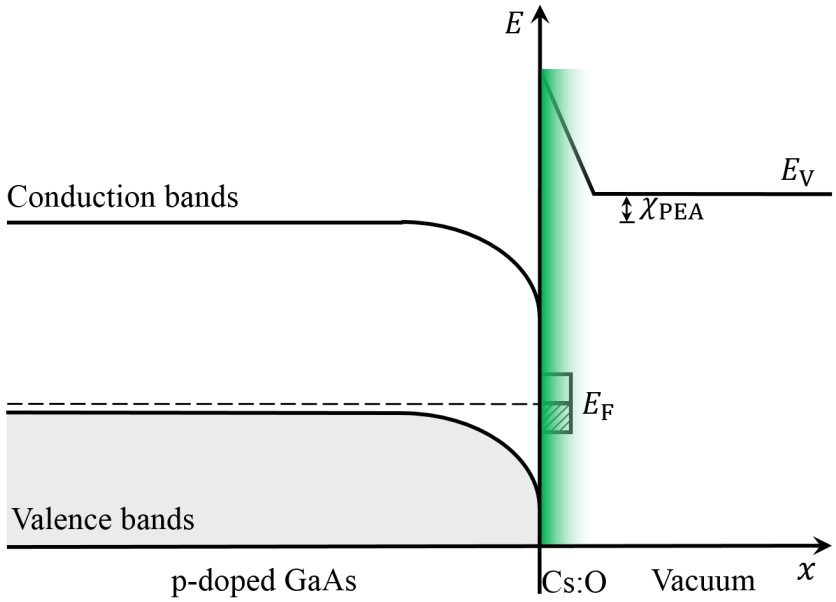

Figure 5.11: In an NEA semiconductor, as the *QE* degrades, the value of χ_{NEA} continues to decrease, and at very low *QE* values, the χ_{NEA} eventually becomes χ_{PEA}.

As long as χ_{PEA} is less than the energy surplus of 130 meV and if the electrons do not lose their energy substantially in the scattering processes, electrons can still be emitted into the vacuum. However, since these electrons thermalize, they only

exist for the first few picoseconds. In other words, in the first few picoseconds the probability of the transmission is still high, though lower than that of when the *QE* was higher.

After the first few picoseconds, more electrons thermalize. This reduces the number of electrons which have enough energy to overcome the PEA barrier and suppresses their escape probability. However, the electrons which arrive at the surface late will meet the condition described in Eq. 5.22. As the *QE* drops lower, the cathode reaches higher values of PEA, resulting in the tail of the pulse response dropping faster, as seen if Fig. 5.6.

5.8 Asymmetry measurements

Spin-polarized electrons have been essential in a wide variety of branches of physics, such as atomic and condensed matter physics [59], solid-state physics to study surface and thin-film magnetism [38, 119], and nuclear and high-energy physics to investigate the nuclear structure and high-precision determination of the electroweak mixing angle [2, 62].

The sources of polarized electron beams are vital in many high-energy accelerator facilities such as SLAC, ELSA, CLIC [4], and CEBAF [5], and they will be required for all future linear colliders, like EIC and ILC [6]. Since the efficiency of the accelerator operation is proportional to the square of the degree of the beam polarization, any photocathode optimization that leads to higher polarization can significantly increase the output of the accelerator, and therefore, is of utmost importance.

Choosing photocathode structures with higher Hh and Lh valence band splitting will result in higher initial polarization. Furthermore, having a structure which has a low p-doped active layer, suppresses the depolarization mechanism during the transport of the photoemitted electrons in the conduction band [76]. The SSL GaAs/GaAsP will be the subject of the next chapter, where its polarization and other physical characteristics are investigated and discussed further. In the following section, the asymmetry measurements of the bulk GaAs and the time-resolved spin polarization measurements are presented and explained.

At 45 keV, the effective analyzing power of the Mott polarimeter is at least three times less than at 100 keV. Recalling $A = S_{\text{eff}}P$, the respective measured asymmetry at 45 keV is smaller by at least a factor of three. Thus, the measuring time is 10 times longer for the same relative statistical error. As expected, longer measuring times worsen the time resolution severely. As a result, a low-energy electron beam is particularly troublesome for any polarization measurements.

For completeness, one must note that even though the asymmetry and the time resolution have suffered greatly due to the low-energy beam, in principle no difference in the physics of the results has occurred. Even in this more difficult case,

[4] Compact Linear Collider, *CERN*
[5] Continuous Electron Beam Accelerator Facility, *Virginia, USA*
[6] International Linear Collider, *CERN*

the extracted asymmetries are still expected to approximate the true distribution reasonably well.

5.8.1 Gold target thickness

The Mott polarimeter in PKAT is equipped with a set of gold foils with different thicknesses. During the early preliminary studies with the Mott polarimeter, the reproducibility of the asymmetry measurements for each of the three gold targets was investigated. The specifications of the targets are listed in Table 4.2. The GaAs photocathode is excited by circularly polarized laser light at $\lambda = 800\,\text{nm}$, and the electrons are guided into the spin-rotator Wien filter in order to rotate their polarization vector before reaching the Mott polarimeter. The helicity of the laser light is reversed at a frequent interval. The asymmetry values for the targets were obtained in sequence under similar conditions of beam quality and position. The results are presented in Fig. 5.12.

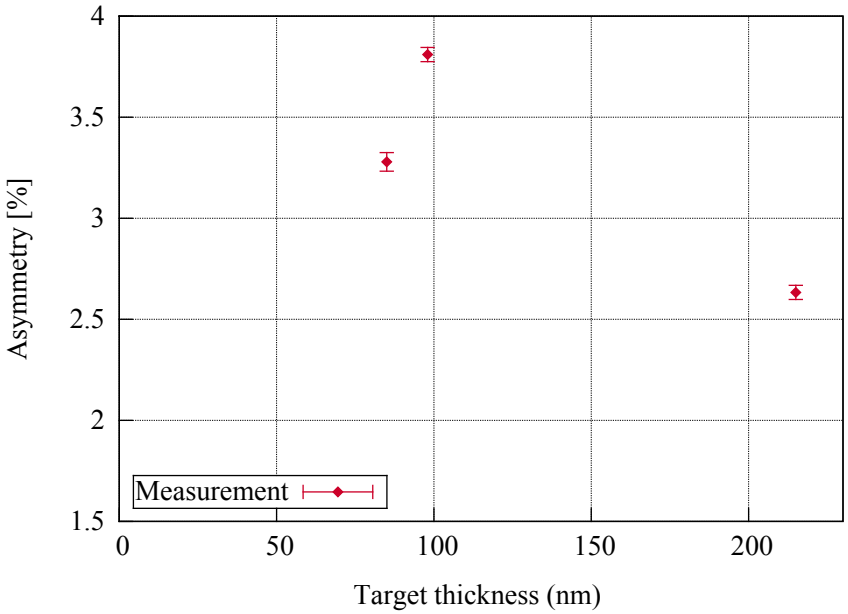

Figure 5.12: Asymmetry measurements for the three gold targets with different thicknesses.

One expects to achieve higher asymmetry values as the target thickness is reduced. As the thickness of the target increases, the probability of multiple scattering for the electrons substantially increases, which in turn reduces the asymmetry. However, the asymmetry for Target3, the thinnest gold foil (85 nm), was measured less than of the Target2 (98 nm). Since Target3 has carbon backing, one can speculate that the scattering from the carbon foil may have contributed, and therefore, has reduced the asymmetry. However, if the carbon foil has the proper thickness,

the foil will contribute to the count rate an insignificant amount (only a few percent).

Notably, the Mott polarimeter with the present gold foils was assembled a few years prior to this project. During the reconstruction of the PKAT, the decision was made not to open the Mott polarimeter. The risk of damage was too high to dismantle the Mott polarimeter and thoroughly examine the conditions of each of the gold foils. The detectors count rate for each of the targets were examined. Although Target1 is three times thicker than Target3, almost identical counts for these two gold foils were observed.

According to our findings for Target1 and Target3, an assumption was made that perhaps these two gold foils were defective. Since the values for these two targets were not reliable, all the asymmetry measurements in this project were taken using Target2.

5.8.2 Effect of the slit

In the investigations with the Mott polarimeter, the asymmetry was measured both with and without inserting the slit while the deflector cavity was switched off. The measurements were conducted under the same conditions of beam position and beam quality. The obtained asymmetry measurements were:

$$\begin{aligned} A &= (3.868 \pm 0.046)\,\% \quad \text{with slit} \\ A &= (3.903 \pm 0.046)\,\% \quad \text{without slit} \end{aligned} \tag{5.25}$$

These values show no significant difference and are within the margin of error. These findings indicate that the beam was focused well, and that the size of the beam was small enough so that removing the slit did not cause any major differences in the outcome.

5.8.3 Laser mode of operation

Finally, the influence of the mode of the laser operation on the asymmetry values was investigated to observe whether changing the laser from DC to pulsing has any effect on the asymmetry for a fixed wavelength. The wavelength was kept at the fixed value of 800 nm. The asymmetry measurements yielded:

$$\begin{aligned} A &= (3.651 \pm 0.032)\,\% \quad \text{DC laser} \\ A &= (3.607 \pm 0.037)\,\% \quad \text{Pulsed laser} \end{aligned} \tag{5.26}$$

A comparison between the measured asymmetries of the DC and the pulsed laser reveals that as long as the wavelength is kept constant, the asymmetry does not change by changing the laser mode of operation.

5.8.4 Effect of quantum efficiency

Another part of this research investigated the dependency of the asymmetry on the *QE*. The objective was to observe whether the asymmetry changes as the *QE* of the photocathode decays, especially at very low *QE*. The asymmetries of the bulk GaAs for *QE*s ranging from 3.14 % to 1.69×10^{-6} % has been measured. Fig. 5.13 illustrates the results of the investigation.

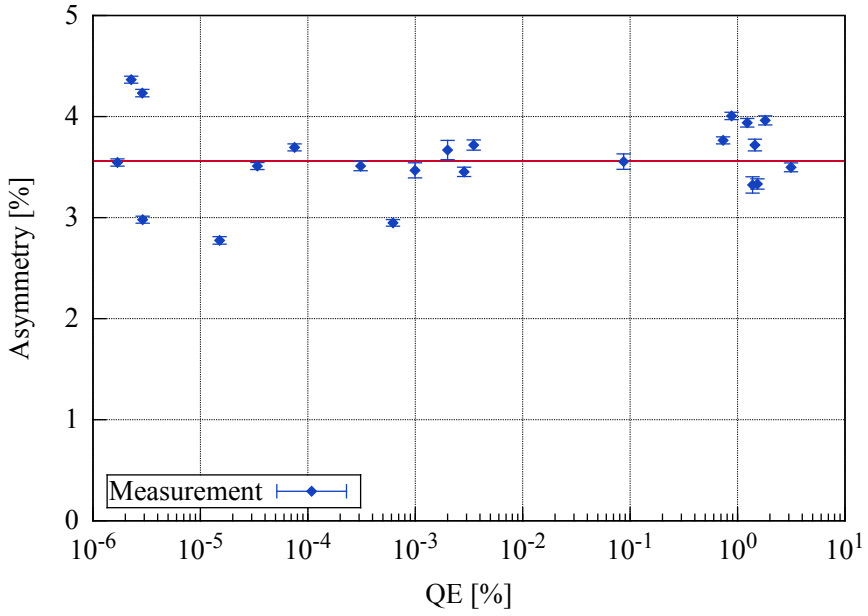

Figure 5.13: Asymmetry as a function of *QE* for bulk GaAs Cathode1. The red line drawn at $A = 3.65\,\%$ is to guide the eye.

In Fig. 5.13, the errors are the statistical errors and the line drawn at $A = 3.65\,\%$ is to guide the eye. Figure 5.13 clearly illustrates that the asymmetry for the most part remains unchanged as the *QE* of the cathode decays, even at very low *QE*s in the order of 10^{-6} %. While the *QE* decayed by seven orders of magnitude, the asymmetry changed by approximately 20 % relative to the average asymmetries. The observed fluctuations are assumed to be the consequence of the reproducibility issues stemming from the low electron beam energy.

The asymmetry should remain constant under similar measurement conditions. During our measurements, the conditions, though not ideal, remained the same. The limitations of the low beam energy in tandem with the limitations due to the old age of the apparatus are distinct disadvantages in measuring the asymmetry. Thus, the observed fluctuations in the asymmetry while *QE* is decaying are assigned to the reproducibility issues due to the aforementioned limitations.

The fact that measured asymmetries have the same order of magnitude even at very low *QE*s is very significant and plays an important role in explaining the

behavior of the cathode and the obtained photoemission at very low *QE*s. One could argue that since great numbers of Cs atoms are deposited on the surface of the bulk GaAs, the measured electron yield at very low *QE*s can be derived from the infrared laser illuminating the Cs atoms and thereby producing photoexcited electrons. However, this statement is erroneous. According to [59], photoemission from Cs atoms is not polarized. As seen in Fig. 5.13, the polarization even at very low *QE*s has not changed substantially. Therefore, the measured *QE* cannot be from Cs atoms on the surface and must be from the GaAs, thus ruling out this argument.

Moreover, the possibility of the photoemission resulting from the Pockels cell creating the frequency doubling must be ruled out since ultraviolet does not produce asymmetry [59].

5.9 Time-resolved polarization measurements

The last investigation with the bulk GaAs crystal was the time-resolved polarization measurements. These measurements were possible with the help of the cavity, the slit, and the phase shifter, as described in Section 4.8.

First, the electron beam is passed through the slit, and the phase that gives the best focused beam on the Mott screen is recorded. Next, the phase is shifted from the point of maximum intensity in small increments, allowing different sections of the beam to go through the slit. For each phase shift, the asymmetry is measured. In order to reduce the error in the measurement, the phase is increased or decreased randomly in various increments.

A temporal profile of the asymmetry for the bulk GaAs measured at 800 nm with a *QE* of 1.81 % is illustrated in Fig. 5.14.

In regards to these measurements, a few comments are worth making. First, the errors shown in Fig. 5.14 are the statistical errors. In this particular measurement, the errors were approximately 0.25 %. The time to collect a typical data point ranged from 3 minutes to 50 minutes depending on the phase shift. For the higher values of the phase shift, yielding the lower values of asymmetry, the measurement times were extended accordingly in order to obtain fairly similar statistical errors. As mentioned previously, the longer asymmetry measurement times are mainly due to the low beam energy.

Second, the step-wise pattern in Fig. 5.14 is assumed to be connected to a temperature drift which counteracts or intensifies the shifting of the phase for a certain period. This period depends on whether the air conditioning is on or off. The correlation between the room temperature fluctuations and the phase drift was investigated in [35], and an influence of approximately 2 ps was estimated. Therefore, the influence of the temperature variations on pulse response measurements can be extremely important, and the time of measurement in relation to the air conditioning control cycle must be considered.

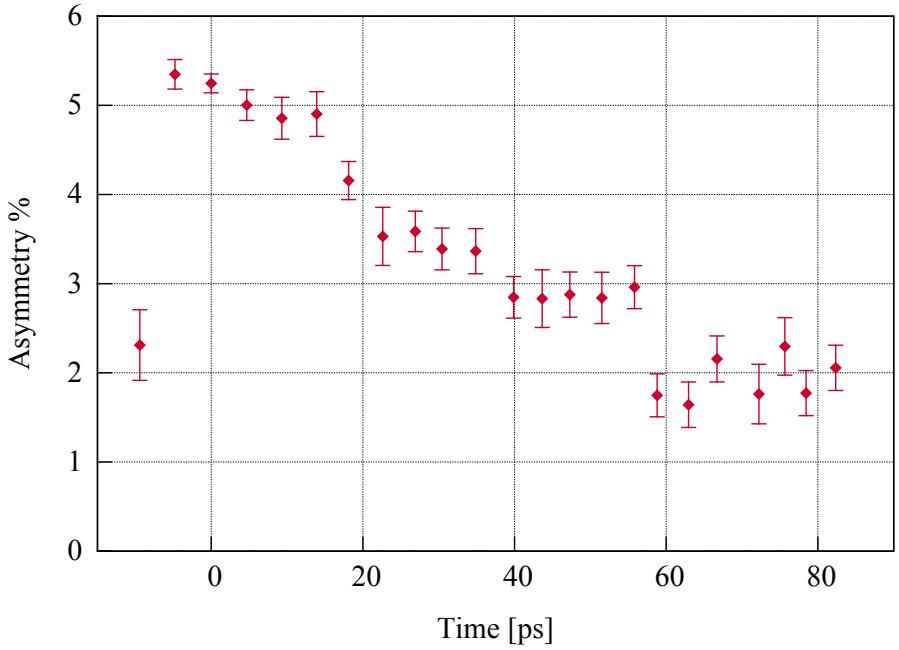

Figure 5.14: Time-resolved polarization measurement for the bulk GaAs Cathode1 at 800 nm and at a *QE* of 1.81 %.

The asymmetry and the polarization at any given time are related via the relationship

$$A\,(t) = S_{\text{eff}} \cdot P(t) = S_{\text{eff}}\, P_0\, e^{-t/\tau_{\text{relax}}} \tag{5.27}$$

where S_{eff} is the Mott analyzing power, P_0 denotes the polarization at $t = 0$, and τ_{relax} is defined as the polarization relaxation time or depolarization time. In relation to semiconductor, these two parameters are interesting. By excluding the points below $t = 0\,\text{ps}$, and with an adequate exponential fit to the remaining points in the plot of the Fig. 5.14, the depolarization time for this specific measurement can be found. The data points which fall below $t = 0\,\text{ps}$ will be explained later. The exponential fit will result in

$$\tau_{\text{relax}} = 70.28\,\text{ps} \tag{5.28}$$

This result means the polarized electrons in the GaAs remain polarized, on average, for only about 70 ps. Although this time period is not very long, the time period is reasonable for this specific photocathode, as discussed in detail in the following.

The particular GaAs photocathode under study is highly doped with Zn atoms with the concentration of $(1.1-1.3)\times 10^{19}\,\text{cm}^{-3}$. The spin-polarized electrons which come to the surface of the semiconductor and escape immediately have maximum polarization. The electrons which are emitted at later times are exposed to many

processes that can flip their spins. The depolarization can be attributed to the BAP process, (see Section 2.6.3), and fluctuations of the impurities in the crystal. The process of the spin-polarized electron transport was investigated by *Gerchikov et al.* [45] with AlInGaAs/AlGaAs strained superlattice. The weakening of the electron transport was attributed to the presence of partial electron localization within the cathode. According to [45], increasing the density of electronic traps leads to higher localization level, which in turn increases the photoelectron losses and lowers the polarization.

We now turn our attention to exploring the behavior of the data points in the region of $t < 0$ ps. The RF system in the PKAT laboratory is based on the MAMI deflecting cavity operating at 2.499 GHz, which yields a period of about $T_{\mathrm{RF}} \approx 408$ ps. During each period of the RF, the electron pulse passes the slit twice.

At each point in time, besides the initial intensity that passes through the slit at that time, a contribution of all the intensities passing the slit at each half period occurs. For each of these points in time, a corresponding polarization can be measured with the Mott detectors.

At $t < 0$, the initial intensity and each of the subsequent intensities, which pass through the slit at each half period, are much less than those of at $t = 0$, and therefore, their contribution to the intensity is minimal, see the discussion in Section 5.6. Moreover, the electrons which are detected at time $t < 0$ have stayed in the crystal for a relatively significant amount of time, and as a result, have suffered a high amount of depolarization. Therefore, in a time-resolved polarization measurement for the bulk GaAs, the points at $t < 0$ are dominated by the longer emission times. These emission times will result in the polarization falling significantly below the true polarization.

This effect is observable so long as the cathode emission time is long with respect to the period of the RF. The polarization suppression effect tends to decrease with decreasing the emission time. This effect is a unique feature of the bulk photocathode and is not apparent in a strained superlattice structure, due to the distinct difference between the bulk and the superlattice. In the bulk, as is demonstrated in Fig. 5.3, the time response is long, and the intensity drops to 5 % relative to the peak intensity after 50 ps for Cathode1. However, in the superlattice, the response is very short, and the intensity drops much faster. For the strained GaAs/GaAsP superlattice, the emission dies out in less than half of the RF period. The results of the pulse response and polarization measurements from GaAs/GaAsP superlattice photocathode will be discussed where appropriate in Chapter 6.

6 Strained GaAs/GaAsP superlattice

For successful operation of any accelerator using RF, the bunch length of the beam during acceleration is extremely important. In the case of the accelerator MESA, which is expected to be in operation in 2023, the maximum accepted bunch length is FWHM = 200 ps. Therefore, all electrons which are emitted at a later time from the photocathode will be cut off and contribute to the longitudinal halo.

The longitudinal halos reduce the photocathode lifetime and damage the accelerator with induced radiation in the accelerator components. In order to function within the longitudinal acceptance of the accelerator, these unwanted electrons must be removed by a chopper, and the resulting bunch compressed by a buncher system. For finite halo, losses will occur in an uncontrolled manner in the accelerator system. Therefore, the chopper is needed for precision measurements. Otherwise, the measurements suffer severely from small losses at high energies, especially if they are varying in time. The chopper is an effective approach to concentrate the losses at low energy where the losses cannot create damage or significant radiation.

In the case of MESA accelerator, a buncher allows transport of rather long pulses (FWHM $\sim$ 200 ps) from the source and "focuses" them longitudinally to approximately FWHM $\sim$ 4 ps at a position where the injector accelerator starts. This "focus" reduces space charge forces at the source and during the transport of the beam to the buncher. A rapid acceleration process sets in immediately after the focus which results in reducing space charge forces considerably while the bunch length remains short. The latter is needed in order to keep the beam energy distribution small. While these systems are well established and function properly in practice, their use results in some undesirable effects. The chopper causes beam loss, while the buncher increases the energy spread of the electrons, which in turn reduces the beam brightness. In order to reduce these effects, short electron pulses are desirable.

After the construction of MESA is completed, the accelerator will deliver a highly brilliant electron beam with a current of up to 10 mA to search for the dark photon. Alternatively, the P2 experiment in MESA demands highly spin-polarized electron beams to study the electroweak mixing angle.

In general, photocathodes which exhibit fast transport are desirable. A typical recombination time is in the order of 1 ns. When electrons remain in the crystal longer, the possibility of the electrons recombining with the valence band holes is greater. As a result, the loss of polarization and any information regarding the transport properties of the cathode are higher. Fast responses reduce the amount of electron recombination and depolarization.

As described in Chapter 2, the electron spin polarization in bulk GaAs cannot exceed 50 % due to the Hh and Lh degeneracy. Single-layer strained photocathodes can provide higher polarization up to 80 %. However, they are unable to deliver a beam of sufficient *QE*. The unique heterostructure of strained superlattice can overcome these limitations. Strained superlattices are capable of producing high-polarization beams since they maintain the required induced strain and can produce high-*QE* beams because the active layer has sufficient thickness.

To achieve the necessary beam brightness at low emittance while delivering high spin polarization, the strained GaAs/GaAsP superlattice photocathode was investigated. In this chapter, after describing the structure of GaAs/GaAsP SSL, the pulse response and polarization measurements are presented.

6.1 GaAs/GaAsP structure

The strained superlattice has a complex structure compared to bulk GaAs; therefore, the transport process of electrons in an SSL crystal is different from the transport in the bulk. In the bulk, photoexcited electrons in the conduction band interact with the lattice atoms through inelastic collisions until they are thermalized. Their energy distribution can be described by a Maxwell-Boltzmann distribution. The absorption coefficient of GaAs is approximately $1.41\,\mu m^{-1}$ at an excitation wavelength of 800 nm. Since the mean free path of the electrons, $30 - 55$ nm, is much smaller than the absorption length, the transport of electrons from the bulk into vacuum can be described by the diffusion model, see Section 2.5.2.

The thickness of the active layer in the strained GaAs/GaAsP is only 92 nm therefore, only 11 % of the light is absorbed in the crystal. In a superlattice, the pulse responses are much shorter than in the bulk. The mean free path and the layer thickness are in the same order of magnitude. The average number of interactions[1] are very few. For the strained GaAs/GaAsP superlattice studied in this work, the number of interactions can amount to 1 - 2 interactions. The transport of the electrons is certainly neither diffusive nor ballistic[2]. Therefore, one cannot assume that the electrons are completely thermalized during the transport. Thus, the energy of electrons cannot be described by a Boltzmann distribution.

The Strained GaAs/GaAsP superlattice was developed at SVT Associates[3] with the specification of B-702 according to the manufacturer. The SSL was grown by molecular beam epitaxy (MEB). The SSL consists of alternating thin layers of GaAs wells and GaAsP barriers. A schematic structure of the strained $GaAs/GaAsP_{0.36}$ superlattice is shown in Fig. 2.12. The SSL fabrication is as follows.

After growth of 2 µm-thick Be-doped ($2 \times 10^{18}\,cm^{-3}$) GaAs buffer layer on a p-doped GaAs substrate, a 5 µm-thick Be-doped graded $GaAsP_x$ layer was grown

[1]The average number of interactions can be defined approximately as the layer thickness divided by the mean free path.
[2]Ballistic transport is defined when no interaction between the electrons and the lattice exists.
[3]SVT Associates, Inc., Eden Prairie, USA, www.svta.com

with the P composition increasing from $x = 0$ to 0.35. This graded layer, and all other layers following thereafter, were Be-doped at $5 \times 10^{18}\,\mathrm{cm}^{-3}$. Then, in order to produce a strain-relaxed $GaAs_{0.65}P_{0.35}$ layer compatible with the superlattice active layer, a 2 µm-thick $GaAs_{0.65}P_{0.35}$ layer was subsequently grown. This step was followed by the growth of 14 pairs of GaAs (3.8 nm)/GaAsP (2.8 nm) strained superlattice layers. The layers were capped with a 5 nm-thick heavily-doped GaAs layer that produced the band bending.

The chemical composition and thickness of the strained GaAs quantum well and GaAsP barrier layers determine the SSL energy band structure and subsequently, determine the obtained quantum efficiency and polarization from the cathode. The P-fraction in GaAsP has a strong effect on the width of the bandgap, which determines the photon energy corresponding to maximum polarization. The Hh-Lh energy band splitting for $GaAs/GaAsP_{0.36}$ SSL is 89 meV [73], thus capable of delivering high polarization.

6.2 QE and lifetime measurement

Throughout our investigations with the strained GaAs/GaAsP superlattice, the cathode was activated five times as the *QE* dropped to lower values and needed reactivation. The process of reactivation is described in 5.1. Fig. 6.1 represents the effect of subsequent activations.

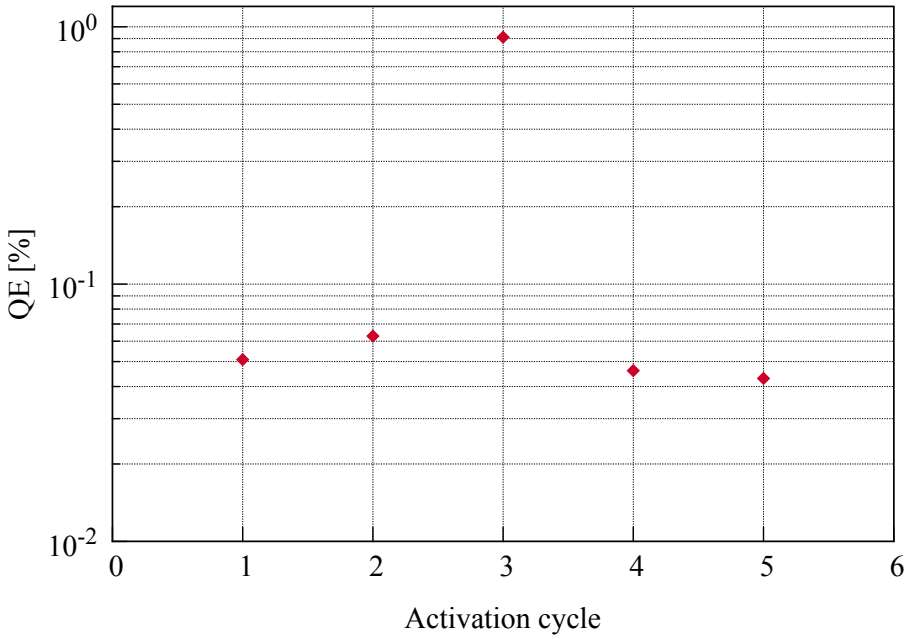

Figure 6.1: The achieved *QE* against the activation cycle for the strained GaAs/GaAsP superlattice.

The *QE* values range from 0.91 % to 5.08×10^{-2} %. The third activation delivered the highest *QE*, similar to the bulk GaAs investigated earlier, see Fig. 5.1. The explanation for the *QE* increase from the second to the third activation is assumed to be similar to the description in Section 5.3.

The lifetime of the SSL photocathode was studied after the first activation, and the *QE* values were collected during a 12 day period. The results are shown in Fig. 6.2. The *QE* ranged from 5.08×10^{-2} % to 3.18×10^{-5} %. The main contributing factors to the decay of *QE* during operation are ion back bombardment and the desorbed gas, see Section 2.3.2 for further discussion. The rise in cathode temperature resulting from high laser power illumination is not important to this study since the average power used during the measurements did not exceed 5.2 mW.

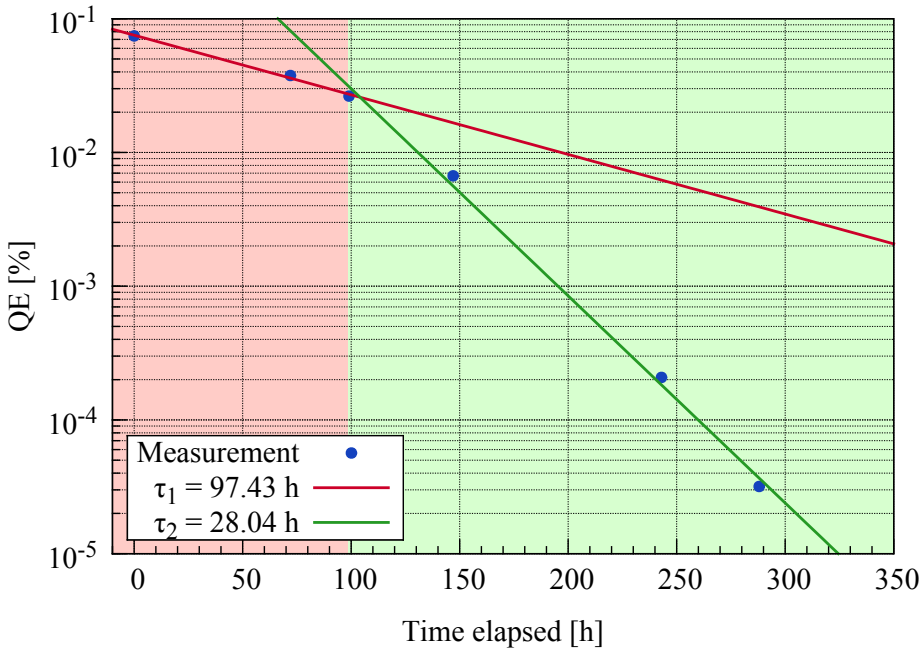

Figure 6.2: Degradation of the *QE* for the GaAs/GaAsP superlattice during a 12-day period. The decay cannot be described with a single time constant.

The decay is characterized by a continuous change of slope and cannot be described with one single lifetime. The lifetime is larger at the beginning $\tau_1 \approx 97$ h, and it becomes shorter with $\tau_2 \approx 28$ h for the interval $t > 99$ h. The drastic change of slope could be a result of a sudden change in the surface conditions or the electron affinity, but these causes are purely speculative. The *QE* decay of GaAs/GaAsP is similar to that of the bulk GaAs; it is exponential only at short intervals of a few days, see Fig. 5.2. This decay similitude is not surprising because the conditions are fundamentally very similar with only small differences which depend on the activation procedure on the nature of the surfaces. For instance, the bulk GaAs

photocathode is simply polished, whereas the SSL is atomically grown on a clean surface, see Section 2.6.2. Thus, differences may exist in the reaction of the crystal towards the contamination. However, these differences do not affect the shape of the *QE* degradation significantly.

6.3 Pulse response

The temporal response measurement of the strained GaAs/GaAsP superlattice was conducted after its first activation. The electron pulses were obtained with near-bandgap laser pulses and with a *QE* of 6.1×10^{-2} %. The setup and the measuring principle was as discussed before. Fig. 6.3 depicts an example of the pulse response of the SSL photocathode along with the transverse beam diameter at the location of the slit.

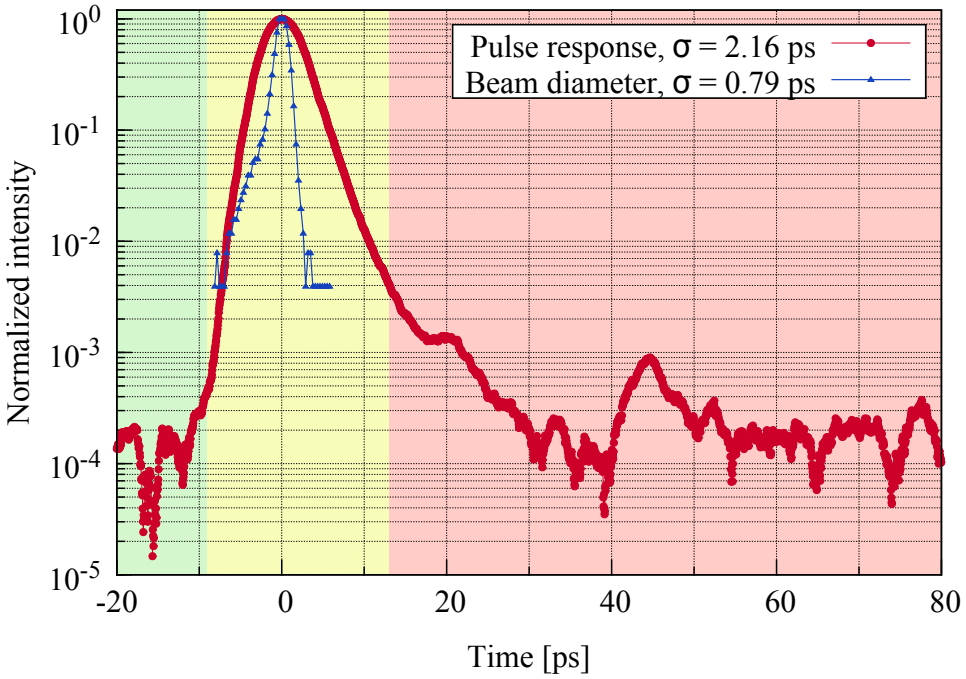

Figure 6.3: Temporal response of a strained GaAs/GaAsP superlattice photocathode. The blue curve represents the transverse beam diameter at the location of the slit.

The result shows an asymmetrical curve with a steep rise and then decay with a fast time constant. The observed σ is (2.16 ± 0.50) ps and still limited by the experimental resolution. The pulse response has a longitudinal halo at a level of 10^{-4} compared to the peak intensity. Regarding the observed pulse response, a few comments are in order:

t < −9 ps region: A possible explanation for the pre-pulse signal could be artifacts of the laser pulse and/or the double reflection of the laser from the optics. The effect of the double reflection is further explained when discussing the $t >$ 13 ps region. Notably, similar pre-pulse signals have been observed in the pulse response measurements with the strained GaAs/GaAsP superlattice and bulk GaAs conducted in the course of this project, as well as with other cathodes such as K_2CsSb [18] and bulk GaAs [35].

-9 < t < 13 ps region: This region is the main section of the pulse response indicating the time that the majority of the photoexcited electrons generated in the crystal are thermalized and then transported into the vacuum. As Fig. 6.3 indicates, the shape of the pulse in this section is asymmetric with a steep rise with a σ of (2.16 ± 0.50) ps.

One must note that the obtained $\sigma = (2.16 \pm 0.50)$ ps for the superlattice indicates that the superlattice is fast and still limited by the experimental resolution. The jitter of the RF field, the jitter of the position of the beam, and the transverse beam diameter have the most severe impact on the experimental resolution, see the discussion in Section 3.5. Therefore, the GaAs/GaAsP would present a faster response if the experimental conditions were better.

The best possible time resolution obtained at energy of 100 keV and excitation wavelength of 400 nm is $\sigma = 1.10$ ps [17]. Our measurements suffered from a stronger influence of AC fields and longer integration times due to the slower phase shifting. Therefore, although one expects faster pulse responses from the strained GaAs/GaAsP superlattice, the time resolution increased by factor of approximately 2 and resulted in longer pulse response. However, the increase of the time resolution has no real influence on the interpretation of the results which are presented.

The left shoulder defines the time resolution. In an ideal case, the emission of electrons should start almost immediately after excitation, and all of the electrons have the same energy at the surface. In this case, one will observe an infinitely steep curve on the left. However, due to the time resolution of the apparatus and the transit time spread caused by the initial energy distribution, one observes an asymmetric peak which is not infinitely steep on the left.

The right shoulder of the peak is associated with the response function of the cathode and decays exponentially. This decay is consistent with the thermalization time of the electrons in the material. With an exponential fit to the right shoulder, the decay time can be calculated. Within this time the photoexcited electrons come to equilibrium with the lattice and have enough energy to transport to the surface and into the vacuum. Fig. 6.4 shows the exponential decay to the left shoulder between $t = 0$ and $t = 13$ ps with the function

$$I(t) = I_0 e^{-t/\tau} \tag{6.1}$$

where I_0 is the intensity at $t = 0$ and τ is the decay time constant. According to Eq. 6.1, the decay time constant in this case is $\tau = (2.38 \pm 0.30)$ ps.

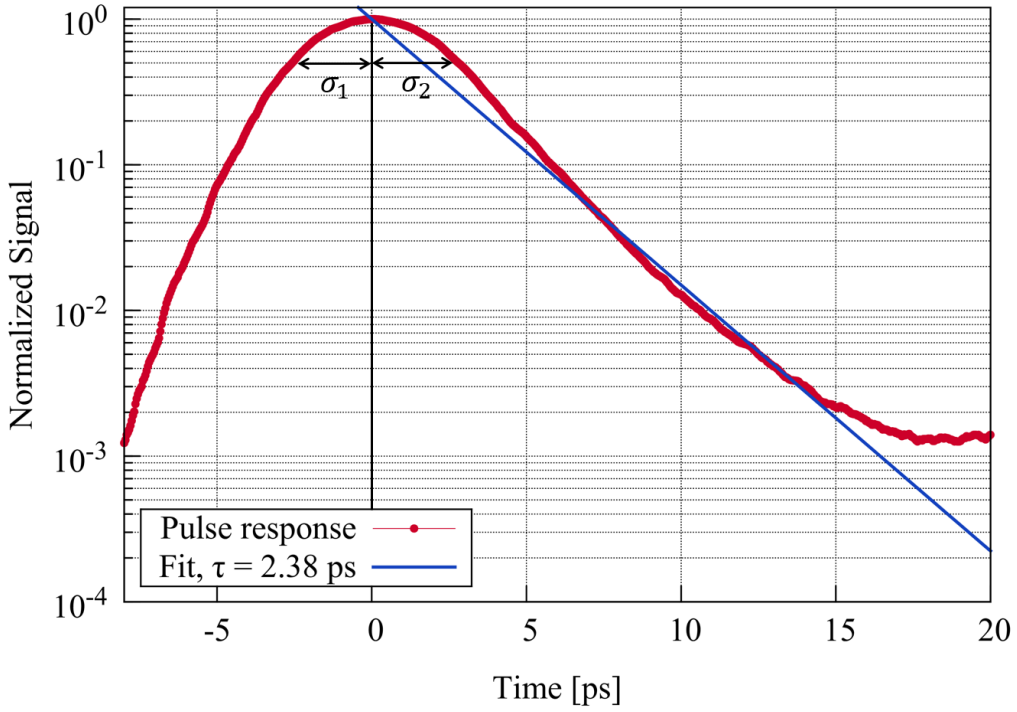

Figure 6.4: Magnified picture of the pulse response of GaAs/GaAsP superlattice from Fig. 6.3. An exponential decay to the right shoulder of the pulse response for the time interval $0 < t < 13$ ps results in a time constant of (2.38 ± 0.30) ps. σ_1 refers to the resolution which is the $\sigma_1 = 2.16$ ps of the Gaussian, and mostly affected by the apparatus resolution. $\sigma_2 = 2.36$ ps is the time constant of the exponential decay and is limited by the thermalization time and is convoluted by the resolution. This limitation explains the increase in the time constant σ_2 compared with σ_1. Since τ is obtained for the time interval which is longer than the σ_1, τ is not distorted by the finite resolution of the apparatus. The pulse response around the 20 ps does not follow the exponential decay which is attributed to the presence of the double reflections of the laser, see further explanation in the text.

t > 13 ps region: This section of the pulse response is in the order of about 3×10^{-4} relative to the maximum intensity at $t = 0$. The observed signal in this region may be the result of the double reflection of the laser from the optics on the path of the laser. As the laser beam passes through the interface of two media with different refractive indices, a fraction of the incident laser intensity is reflected. Assuming that the light is incident at a normal angle, the fraction of reflected intensity is given by the *Fresnel* equation

$$R = \frac{(n_1 - n_2)^2}{(n_1 + n_2)^2} \tag{6.2}$$

where n_1 and n_2 are the refractive indices of the two media. This equation accounts for the fact that each time the optical medium changes, a fraction of the laser is reflected, and the rest will be transmitted.

After the laser is produced, it travels through a polarizer, the Pockels cell, a telescope, and a window before reaching the cathode. This process is illustrated in Fig. 6.5.

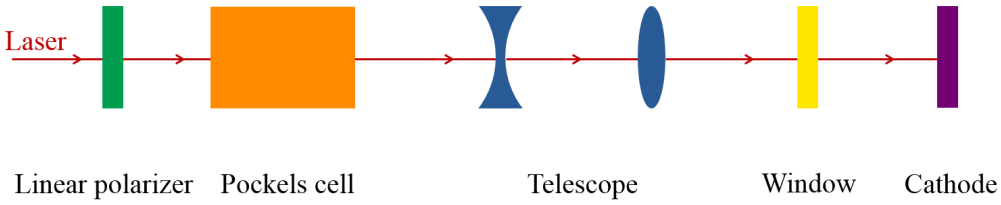

Figure 6.5: Optical elements which the laser passes through before reaching the photocathode. These elements contribute to the double reflection of the laser. Double reflections between the elements are superimposed over each other and arrive at the cathode at later times depending on the distance they travel.

One can assume that the anti-reflection coating sets an upper limit to Fresnel reflection of laser-optic at 0.5 % of the initial intensity. Therefore, one cannot apply Eq. 6.2 because of the special treatment of the optical surfaces, for example the glass with the anti-reflective coating. The two surfaces which have the highest reflection coefficients are the window and the cathode. For instance, the entrance window to the vacuum system has at least one surface which does not have an anti-reflective coating. Assuming $n = 1.4$ for the window, each time the laser passes through the window 3 % of the laser is reflected at the interface.

The largest contribution to the reflected light comes from the GaAs/GaAsP crystal itself. With a refractive index of $n \approx 3.0$ at 800 nm, the crystal reflects more than 20 % of the laser light. A double reflection between the window and the cathode, therefore, will create a pulse with a relative intensity of $I = 6 \times 10^{-3} I_0$, where I_0 is the initial pulse intensity from the undeflected laser. Similarly a double reflection of approximately 1.5×10^{-4} and 2.5×10^{-5} can be expected for double reflections between window–optics and between optics–optics, respectively. These reflected intensities will create "parasite" pulses which illuminate the cathode at different times than the main laser pulse. The arrival times are given by $2d/c$, where d is the distance between the two surfaces and c is the speed of light.

For the cathode–window reflection, one can assume that the laser spot at the cathode is larger and has an offset from the original laser spot since the surfaces of cathode and window are not exactly perpendicular to the beam. Furthermore, the distance between the two surfaces is very large (≈ 1.0 m). These factors reduce the contribution of the "parasite" pulse considerably. Therefore, in Fig. 6.3 the observed

peak at around 40 - 50 ps with the intensity of approximately 10^{-3} is possibly the result of double reflection. The appearance and absence of such peaks is possible due to small changes in the angles of the laser beam which leads to different positions (offsets) of the double reflections on the photocathode.

In Fig. 6.3 many small random peaks are observed. Since the background is in the order of 10^{-3}, these signals are not attributed to the crystal behavior. The observed signals in the $t > 13$ ps region are speculatively, the upper limit of the contributions from the photocathode plus the double reflection. The presence or absence of these extraneous double reflections may be ascertained by removing each of the mediums from the optical path and monitoring any changes. Eliminating the possible effects of the double reflection was outside the scope of this project, and hence, no attempt was made to investigate the effect. Further plausible interpretations of the observed signals at $t > 0$ could be the result of electrons being reflected from the walls of the beamline and entering the channeltron independent of the phase.

In an investigation with InAlGaAs/GaAs superlattice [45], similar signals in the order of 10^{-2} compared to peak intensity were observed. However, in that case, the observed signals were attributed to the photocathode. For GaAs/GaAsP, approximately 3×10^{-4} is the upper limit. Therefore, the strained GaAs/GaAsP superlattice is a better photocathode since it offers a smaller halo.

The true time response of the strained GaAs/GaAsP superlattice is faster than the observed resolution of $\sigma_{\text{obs}} = (2.38 \pm 0.30)$ ps since the apparative resolution and the transit time dispersion superimpose the true response of the cathode. The true response can be obtained by

$$\sigma_{\text{cathode}} = \sqrt{\sigma_{\text{obs}}^2 - \sigma_{\text{res}}^2}. \tag{6.3}$$

Recalling $\sigma_{\text{res}} = (2.16 \pm 0.50)$ ps from Fig. 6.3, this computation will lead to $\sigma_{\text{cathode}} = (0.99 \pm 1.20)$ ps for the true response of the strained GaAsP/GaAs superlattice, which is compatible with zero.

Worthy of note is that the pulse response measurements of the GaAs/GaAsP superlattice were repeated at different QEs of 5.08×10^{-2} % and 7.44×10^{-2} %. The results of these measurements are illustrated in Fig. 6.6.

In Fig. 6.6, comparing the pulse responses a few remarks are fitting. First, all pulse responses show a series of Gaussian-like humps in the $t > 13$ ps region. Regardless of the QE, the hump between $40 - 50$ ps is present, although with different intensities. These responses further strengthen the likelihood of the humps resulting from double reflection.

Furthermore, the observed longitudinal halo of the pulses in blue and green is higher than the halo shown in red, but the results are limited to a detection of 3×10^{-4} compared to the peak intensity. In addition, in the measurement with the lowest $QE = 7.44 \times 10^{-2}$ % (the green curve), the signals after the main peak look different when compared to the other curves. One could speculate that the green curve suffered from an electronic background condition, e.g. X-rays impinging on the channeltron. This is supported by the background, in particular at $t < 0$,

where the cathode clearly cannot have such high halo. This high halo measurement indicates that problems occurred with the measurements and ultimately limited the sensitivity of the method. The blue and red curves contain the effects of double reflections, as discussed previously. Other noise factors which are not completely reproducible may have also affected the results.

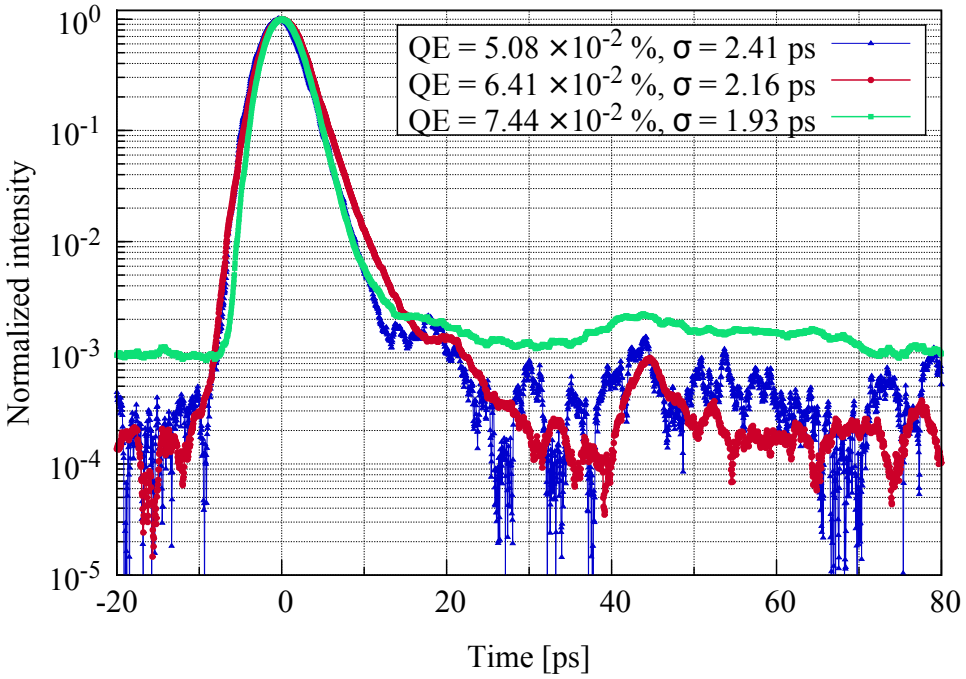

Figure 6.6: The pulse responses of strained GaAsP/GaAs superlattice conducted at different *QE*s.

Moreover, comparing the σ and the background levels of the pulses, the differences can be attributed to operating at the low beam energy of 45 keV; at such low energy any fluctuations will impact the observed intensity severely, for instance, the increased jitter as a result of the air conditioning in the lab operating in a different state, see the discussion in Section 3.5.

6.4 Comparison of GaAs/GaAsP with K_2CsSb and GaAs

Pulse response measurement of K_2CsSb (potassium cesium-antimonide) photocathode at an excitation wavelength of 400 nm was conducted [18]. The measurement was carried out in the PKAT laboratory and with a 100 keV electron source, prior to experiencing field emission and breaking down the source. The measurement setup and the principle of the measurement was similar to what was used during this project. Fig. 6.7 illustrates the comparison of the impulse response measure-

ments between GaAs/GaAsP superlattice, K_2CsSb, and the bulk GaAs (Cathode2) photocathodes, taken at *QE* of 6.1×10^{-2} %, 1 %, and 5.8 %, respectively.

Unlike GaAs cathodes, which are purchased commercially, K_2CsSb cathodes are usually fabricated in the lab. Thus, the elementary parameters may vary from one cathode to another according to the specific synthesis recipe concentration, preparation, vacuum conditions, etc. In the literature, a bandgap in the range of $1 - 1.2$ eV [46, 83], effective electron affinity, χ_{eff}, between 0.4 eV to 1.1 eV [83, 84], and a work function of 1.6 eV have been reported.

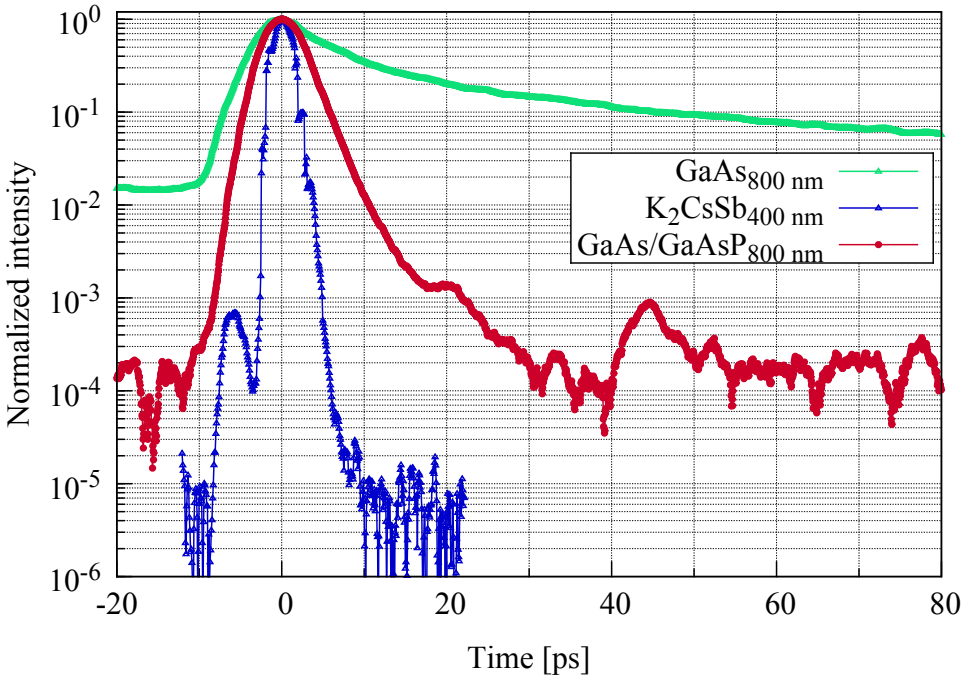

Figure 6.7: The comparison of temporal response measurements of strained GaAs/GaAsP superlattice with K_2CsSb and bulk GaAs photocathodes. The pulse responses of GaAs/GaAsP and bulk GaAs are obtained at a beam energy of 45 keV and an excitation wavelength of 800 nm, whereas K_2CsSb is measured with a 100 keV beam and at 400 nm excitation.

K_2CsSb cathodes belong to the positive electron affinity (PEA) group, and as such, the vacuum level is above the conduction band minimum. Therefore, the photon exciting energy must be greater than $E_{\text{gap}} + \chi_{\text{eff}}$, and only electrons with energy above the vacuum level can be emitted into the vacuum.

The results indicate the bulk GaAs pulse response has a σ of approximately (3.21 ± 0.50) ps and a longitudinal halo around 10^{-1} compared to the intensity maximum. GaAs/GaAsP SSL has a longitudinal halo more than 2.5 orders of magnitude smaller than bulk GaAs. This difference clearly illustrates the improvement that one achieves using strained GaAs/GaAsP superlattice rather than the

bulk in producing short pulses. In bulk, the active layer is the entire thickness of crystal (510 − 517 µm), where photoexcited electrons can, in principle, be generated. However, SSL has an active layer thickness of ≈ 92 nm. The electrons are generated close to the surface and can be emitted much faster into the vacuum. K_2CsSb has a response of approximately $\sigma \approx 1.10$ ps and a longitudinal halo at a level of about 6×10^{-5} compared to the intensity maximum [18]. This indicates the clear advantage of the PEA K_2CsSb cathodes over the NEA cathodes for high brightness electron beam applications. The main characteristic parameters of these investigated photocathodes are summarized in Table 6.1.

Table 6.1: Comparison of the main characteristic parameters of the pulse response between GaAs/GaAsP, bulk GaAs, and K_2CsSb [18] photocathodes.

Parameter	**GaAs/GaAsP**	**GaAs**	**K_2CsSb**
Energy	45 keV	45 keV	100 keV
Excitation wavelength	800 nm	800 nm	400 nm
Pulse response (σ)	2.16 ps	3.21 ps	1.10 ps
Longitudinal halo	3×10^{-4}	1×10^{-1}	6×10^{-5}
Experimental resolution (σ)	1.37 ps	1.37 ps	1.03 ps
Beam diameter (σ)	0.79 ps	0.79 ps	0.37 ps

To complete the comparison between the temporal response of these photocathodes, a few points merit some discussion. In K_2CsSb pulse response, many small signals are observed after the main peak. Although the intensity of these humps is not the same, they are present with different strengths and at different times. These signals are attributed to the double reflection of the laser light. The contribution of the double reflection in measurements with the SSL is speculated to be more than in the case of K_2CsSb because in the latter measurement the polarizer and the Pockels cell were not in the optical path of the laser. Assuming equal contributions from each optical element, the total reflected intensity in the case of the GaAs/GaAsP SSL is estimated to be twice that of the K_2CsSb.

The K_2CsSb response measurement was conducted at 400 nm. In general, the photoexcited electrons are not deep inside the crystal when excited with lower wavelengths. This placement allows faster emission time compared to higher wavelengths. In addition, the response of K_2CsSb has been conducted at 100 keV compared to the 45 keV for the SSL. The lack of high-energy beam has contributed immensely to poorer experimental resolutions, see Table 6.1 and the discussion in Section 3.5. Fig. 6.7 reveals the striking influence of the experimental resolution on the temporal response of the strained superlattice. Moreover, in the investigation with K_2CsSb, other pulses with higher longitudinal halo in the order of 2×10^{-4} have been observed [18]. The K_2CsSb temporal response shown in Fig. 6.7 is an example of minimum longitudinal halo. For an equitable comparison,

one must compare the pulse response of the strained GaAs/GaAsP superlattice at 400 nm with a beam energy of 100 keV.

The distinguishing characteristic of the strained GaAs/GaAsP superlattice compared to the K_2CsSb and the bulk GaAs is its ability to produce high spin-polarized electrons. As previously discussed, producing beams of highly polarized electrons requires the degeneracy of valence bands to be broken. Neither K_2CsSb nor bulk-GaAs crystal structures allow the generation of highly spin-polarized electron beams.

6.5 Excitation wavelength dependency

The MIRA laser in PKAT is equipped with a tunable-wavelength light source between 755 nm and 890 nm. The dependency of the quantum efficiency and asymmetry on the excitation wavelength for the SSL photocathode was investigated. For this purpose, the laser was operated in DC mode, and the wavelength was changed in the range of 768 − 871 nm, corresponding to exciting energies between 1.61 − 1.42 eV, respectively. Due to some technical problems, the exploration of wavelengths below 768 nm was not possible. The *QE* and asymmetry spectrums as a function of illumination energy are presented in Fig. 6.8.

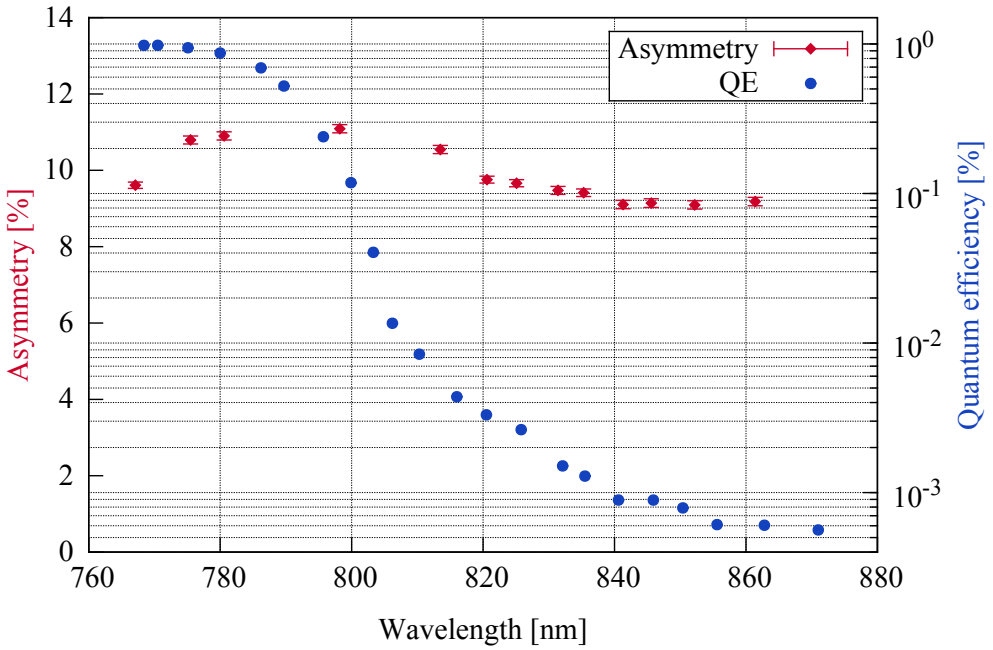

Figure 6.8: Asymmetry and quantum efficiency as a function of the exciting wavelength for the strained GaAs/GaAsP superlattice.

The results indicate a strong correlation between *QE* and the laser energy. The quantum yield increases with energy (decreasing wavelength) to an optimum value

and then remains almost constant. As the wavelength increases, the *QE* decreases, ranging from 0.98 % to 5.02×10^{-4} %. These results are in agreement with the findings of other groups who used similar SSL structure [67, 73]. The laser wavelength of $\lambda = 770.5$ nm yielded the maximum $QE = 0.98$ %.

According to Fig. 6.8, the band edge for the strained GaAs/GaAsP superlattice is approximately at 800 nm. At energies higher than the band edge, electrons will be emitted both from the valence band and the intermediate states in the forbidden zone. Under these circumstances, thermal or other excitations can bridge the gap and be emitted into the conduction band, increasing the quantum yield. For practical purposes, excitation of a photocathode at a wavelength above the band edge is not desirable due to the decrease in *QE*, as is seen in Fig. 6.8.

From a quantum mechanics perspective, the quantum efficiency can be described according to the contributions of the transition rates [114]. The quantum yield of electrons excited by energy γ within the thickness interval $\mathrm{d}x$ can be written as

$$QE \propto P_\alpha(\gamma, x, \mathrm{d}x)\, P_T(\gamma, x)\, P_E(\gamma) \tag{6.4}$$

P_α describes the probability of electrons to be excited above vacuum level. P_T represents the probability of photoexcited electrons reaching the surface and having sufficient energy to escape the vacuum, and P_E is the probability of the electrons reaching the surface to be emitted into the vacuum.

Another factor contributing to the quantum yield is the density of states, which expresses the number of available states within a region. Recalling the discussion in Section 2.4, the density of states in an energy interval $\mathrm{d}E$ for a 3D semiconductor is proportional to $\sqrt{(E - E_c)}$.

As the photocathode is illuminated with the light, the density of states depends on the exciting energy, and therefore the wavelength. If the electrons are excited at exactly the bandgap, in principle, only one state exists. As the energy increases (lower wavelength), the number of states occupied in the energy interval $\mathrm{d}E$ increases, which in turn enhances the quantum yield. This occurrence explains the behavior of *QE* as the wavelength increases in Fig. 6.8. It must be noted that in the case of a superlattice, the density of states changes in the form of a step function compared to the $\sqrt{(E - E_c)}$ dependency in the bulk (see Section 2.4).

In an investigation by *Maruyama et al.* [73], electron polarization and quantum efficiency from GaAs/$\mathrm{GaAsP_x}$ with systematic changes of P-concentration were studied. For a phosphorous concentration of $x = 0.36$ (similar to the SSL used in our project), in the exciting energy range of 1.5 - 1.9 eV, two distinct steps were visibly seen in the *QE* spectrum, as expected from the density of states. The two steps are associated with distinct excitation transitions of electrons from Hh and Lh minibands to the conduction band. In [73], a peak polarization of approximately 86 % and a *QE* of 1.2 % was achieved for GaAs/$\mathrm{GaAsP_{0.36}}$.

In our investigation, the *QE* spectrum extends up to only 768 nm, which is equivalent to 1.61 eV. Up to this energy level, our *QE* curve is similar to what is presented in [73] and includes the first step at energy of 1.60 eV, associated with the Hh. Due

to the limited tunability of the MIRA laser, the second step at 1.67 eV ($\lambda \approx 740$ nm) was not observable. In addition, sudden changes of slope in the *QE* spectrum can be seen, for example at 855 nm, 840 nm, and 805 nm. Such changes may indicate the presence of bands, but band presence is not a certainty.

According to Fig. 6.8, the peak asymmetry is approximately 11.09 % at the exciting wavelength of $\lambda = 798$ nm, and the measured *QE* at the peak asymmetry is approximately 0.12 %. The measured asymmetries ranged from 9.09 % to 11.09 %. Asymmetries greater than 9.1 % are obtained in a wide range of laser wavelengths, 820 − 861 nm. The asymmetry at its maximum value varies with the wavelength within the limits of 18 %. The highest quantum efficiency of 0.98 % was reached at $\lambda = 770$ nm with an asymmetry of approximately 10.20 % [66].

6.6 Time-resolved spin polarization

The spin polarization of the strained GaAs/GaAsP superlattice was measured in a time-resolved manner. The setup and the principle of measurement are as described previously. The measurements were collected at a wavelength of $\lambda = 800$ nm and at a *QE* of 0.91 %. Fig. 6.9 represents the measured time-resolved spin polarization for the strained GaAs/GaAsP superlattice.

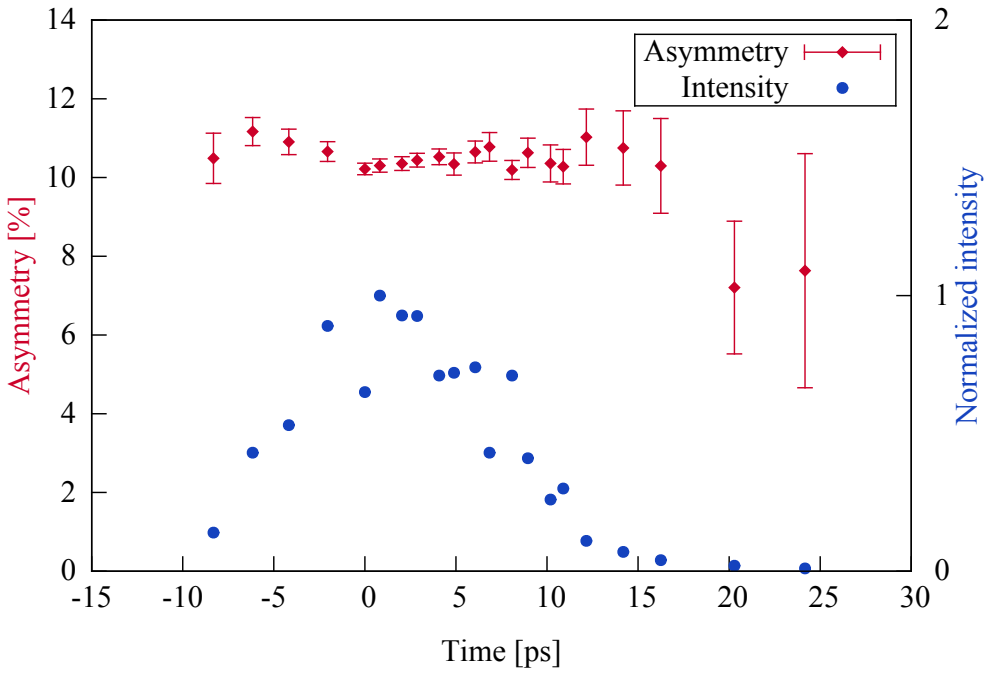

Figure 6.9: Time-resolved spin polarization of strained GaAs/GaAsP superlattice obtained at excitation wavelength of 800 nm and at a *QE* of 0.91 %. The related normalized intensities are shown in blue.

The time-resolved measurement indicates that, although the temporal response is dominated by the experimental resolution, the measured asymmetries fluctuate by a small amount. According to Fig. 6.9, during a period of 24 ps, the time between −8 ps to approximately 16 ps, a relative decrease of 12 % in the asymmetry is observed. At very low *QE* values, however, stronger depolarizations were observed and attributed to experimental difficulties at this timescale.

A possible explanation for the polarization loss during transport is the transit-time dispersion of the photoexcited electrons. The transit-time dispersion imposes different arrival times of electrons to the surface, resulting in a distribution of the kinetic energy as the electrons are emitted into vacuum. Electrons that arrive early tend to have higher kinetic energy and a higher polarization. Electrons with lower kinetic energy are involved in more inelastic processes during the transport and thus have lower polarization.

Another explanation is the possibility that electrons are being trapped in the BBR. These electrons can remain in the surface below the conduction band for some time before exiting the cathode [10]. The energy distributions of the emitted electrons for a strained-layer photocathode [71] and a superlattice structure [70] were measured. According to the measurements, all electrons which escape from the photocathode have gone through some energy loss. Furthermore, as the starting kinetic energy lowers, the polarization decreases.

The time-resolved polarization measurements with a strained-layer GaAsP photocathode with an active layer of 150 nm and a doping of $7 \times 10^{17}\,\mathrm{cm}^{-3}$ were performed. The measurements were obtained with a 100 keV electron source [107]. A relative decrease of spin polarization of 4.5 % during 2.5 ps was observed. Comparing these results with those from [107] indicates that our results have been dominated by the experimental resolution.

The fluctuations in the asymmetry measurements are partly attributed to the drifts in the machine. Recalling that the estimated drift throughout our measurements was in the order of a few picoseconds [35], and considering that the time to take each asymmetry point was 2 to 5 minutes, an assumption can be made that the fluctuations are due to the phase drift.

To complete the analysis of the asymmetry measurements with the strained GaAs/GaAsP superlattice, one must note that the asymmetry values have suffered severely due to the low beam energy of 45 keV. The low beam energy resulted in the instability of the beam during the measurements and required longer measuring times, see the discussion in Section 3.5.

7 Conclusions and outlook

Photoemission sources are essential for successful operation of high-power accelerators. They are capable of offering low-emittance beams with high brilliance. In addition, the pulse response of the photocathode must be within the longitudinal acceptance of the accelerator. Therefore, the losses associated with longitudinal halo must be strictly minimized. The unwanted beam losses result, not only in degradation of the photocathode lifetime, but also in increased radioactivity throughout the accelerator. In addition, the losses associated with the longitudinal halo can create background which masks the physics processes in the detectors. This is particularly problematic for the RF photoinjectors in which the electron pulses are accelerated without a chopper/buncher system.

Furthermore, many accelerator systems require spin-polarized beams. As with MESA, beams of high spin-polarization are required for precision measurements of the electroweak mixing angle (P2) experiment. Presently, the GaAs-based semiconductors are unrivaled as sources of highly spin-polarized electrons.

With an excitation energy near the bandgap, bulk-GaAs cathodes can deliver a maximum polarization of 50 % due to the degeneracy in the valence band. However, strained superlattice photocathodes induce strain in a periodic active layer design. Therefore, they break the degeneracy of the valence band to a higher degree, overcoming the limitations of the bulk and the single strained photocathodes, allowing polarization above 85 %.

In order to conduct the polarization measurements in the context of this work, a Wien filter spin-rotator was built and commissioned to rotate the spin of the electrons before entering the Mott polarimeter.

Within the scope of this dissertation, with respect to the bulk GaAs, one of the goals of this work was to investigate the dependence of the pulse responses on the decay of quantum efficiency. Two bulk photocathodes have been investigated for this purpose. The pulse responses were obtained at *QE* values between 5.81 % and 4.94×10^{-6} %. In both cases, the dependency of the pulse shape on *QE* over many orders of magnitude were clearly observed. The results showed that as the *QE* values dropped, the general trend was such that the intensity of the halo decreased.

In addition, at very low *QE*s, a saturation effect developed. As the *QE* decayed, a more intense laser was needed for the same amount of current. The high-intensity illumination at low *QE*s creates a large buildup of electrons trapped in the BBR, which increases the potential barrier at the surface. The potential increase results in a decrease of electron escape probability and suppression of the latter portion of the pulse response. This tail suppression was attributed to the surface photovoltage.

For the first time, the surface photovoltage was observed at the picosecond timescale in photoemission.

This behavior can be approximated with a continuous pump-probe. In a pump-probe technique, a pump pulse excites a sample, and a second and weaker probe is used for probing the sample after an adjustable time delay. This technique enables measuring ultrafast phenomena, such as the movement of electrons, inside the cathode. In the pulse response, assuming the first 10 ps as the pump period, a very large fraction of electrons (approximately 90 %) arrive at the surface within the 10 ps time frame and contribute to the pump. The remainder of the electrons arriving at the surface at $t > 10$ ps can be considered a continuous probe.

This process exhibits self-modulation for electron pulses at picosecond timescale. The ability to alter the electron pulse properties at the picosecond timescales through a short intense laser pulse is an exciting physical phenomenon and can possibly be applied in electronic devices. Increasing our understanding of the surface photovoltage effect in NEA GaAs crystals through further investigations may potentially lead to overcoming this effect in high-intensity accelerator applications, such as the MAGIX experiment in MESA.

The pulse response and polarization of GaAs/GaAsP strained superlattice at an excitation wavelength of 800 nm was investigated. These measurements can reveal information about the transport mechanisms inside the photocathode and the quality of the cathode material and construction. For the first time, the impulse response of the cathode was measured with high resolution in the tail region. Our investigation delivered a pulse with a $\sigma = (2.16 \pm 0.50)$ ps and a longitudinal halo in the order of 3×10^{-4} compared to the peak intensity.

Our results indicated GaAs/GaAsP SSL has a longitudinal halo more than 2.5 orders of magnitude smaller compared to bulk GaAs. This result illustrates the superiority of the strained GaAs/GaAsP superlattice over the bulk in producing short pulses. Furthermore, comparing the longitudinal halo of GaAs/GaAsP with that of InAlGaAs/GaAs superlattice (conducted at 100 keV) [45], the halo of GaAs/GaAsP was demonstrated to be lower by a factor of almost 2. The pulse response of a cathode is limited by the time resolution of the experiment. Due to the low beam energy, the time resolution increased substantially by a factor of 2.5, compared to the optimum conditions [17]. Therefore, the time-resolved measurements of the GaAs/GaAsP strained superlattice did not show the expected fast response. However, despite the poor time resolution, compared to other superlattices, GaAs/GaAsP can be regarded a better choice of cathode for investigations in accelerator systems, in particular for spin-dependent measurements.

The pulse responses of GaAs/GaAsP superlattice and PEA cathode K_2CsSb, conducted at 100 keV and at an excitation wavelength of 400 nm [18], were compared. The comparison indicated a faster time response, as well as a smaller longitudinal halo for the K_2CsSb cathode. According to these results, K_2CsSb cathodes are more suitable in the high-current accelerator applications.

However, in order to have an equitable comparison between the pulse responses of these two types of cathodes, the strained GaAs/GaAsP superlattice should be

investigated at 400 nm excitation wavelength and at an extraction energy of 100 keV. Although K_2CsSb photocathodes are suitable for generating short pulses with small halos, the emission of spin-polarized electrons from these PEA cathodes is not possible.

With respect to the asymmetry measurements of strained GaAs/GaAsP superlattice, our measurements yielded a peak asymmetry of approximately 11.09 % at an exciting wavelength of $\lambda = 798$ nm, and a *QE* of about 0.12 % at the peak asymmetry. In view of the lower beam energy, the time resolution in the asymmetry measurements suffered additionally due to the longer measuring time, particularly for the data points at higher phase shift values. Consequently, the asymmetry values were tarnished.

Improving the apparatus, using a 100 keV electron beam, and carefully determining the background effects, such as double reflections and channeltron background, a much better time resolution can be achieved. Therefore, smaller halo and higher asymmetry values can be obtained from the strained GaAs/GaAsP superlattice photocathode, making this type of superlattice a good candidate for the electron accelerator applications such as the P2 experiment in MESA.

Bibliography

[1] K. Abe et al. “High-precision measurement of the left-right Z boson cross-section asymmetry”. In: *Physical review letters* 84.26 (2000), p. 5945.

[2] K. Abe et al. “Improved direct measurement of leptonic coupling asymmetries with polarized Z bosons”. In: *Physical review letters* 86.7 (2001), p. 1162.

[3] D. Abraham and H. Hopster. “Spin-polarized electron-energy-loss spectroscopy on Ni”. In: *Physical review letters* 62.10 (1989), p. 1157.

[4] W. a. Ackermann et al. “Operation of a free-electron laser from the extreme ultraviolet to the water window”. In: *Nature photonics* 1.6 (2007), pp. 336–342.

[5] I. C. Alexander. “Experimental investigation of the beam dynamics of the MESA photoinjector”. PhD thesis. Johannes Gutenberg University Mainz, 2018.

[6] R. Alley et al. “The Stanford linear accelerator polarized electron source”. In: *Nuclear Instruments and Methods in Physics Research Section A: Accelerators, Spectrometers, Detectors and Associated Equipment* 365.1 (1995), pp. 1–27.

[7] A. Aronov, G. Pikus, and A. Titkov. “Spin relaxation of conduction electrons in p-type Ill-V compounds”. In: *Sov. Phys. JETP* 57 (1983), p. 680.

[8] K. Aulenbacher et al. “Pulse response of thin III/V semiconductor photocathodes”. In: *Journal of applied physics* 92.12 (2002), pp. 7536–7543.

[9] K. Aulenbacher. “Eine Quelle longitudinalpolarisierter Elektronen für das MAMI-Beschleunigersystem”. PhD thesis. Johannes Gutenberg University Mainz, 1993.

[10] K. Aulenbacher. *Generation of intense, highly polarized electron beams with high symmetry under helicity change*. Shaker, 2007.

[11] K. Aulenbacher et al. “The MAMI source of polarized electrons”. In: *Nuclear Instruments and Methods in Physics Research Section A: Accelerators, Spectrometers, Detectors and Associated Equipment* 391.3 (1997), pp. 498–506.

[12] T. Balasubramanian, J. Cao, and Y. Gao. “X-ray photoemission spectroscopy studies of cesium and oxygen on GaAs (100)”. In: *Journal of Vacuum Science & Technology A: Vacuum, Surfaces, and Films* 10.5 (1992), pp. 3158–3165.

[13] V. Bargmann, L. Michel, and V. Telegdi. “Precession of the polarization of particles moving in a homogeneous electromagnetic field”. In: *Physical Review Letters* 2.10 (1959), p. 435.

[14] G. Baum et al. “Polarized electron-impact ionization of metastable helium”. In: *Physical Review A* 40.11 (1989), p. 6734.

[15] I. V. Bazarov, B. M. Dunham, and C. K. Sinclair. “Maximum achievable beam brightness from photoinjectors”. In: *Physical review letters* 102.10 (2009), p. 104801.

[16] I. V. Bazarov et al. “Thermal emittance and response time measurements of negative electron affinity photocathodes”. In: *Journal of Applied Physics* 103.5 (2008), p. 054901.

[17] V. Bechthold et al. “Investigation of K2CsSb Photocathodes”. In: *Proc. 59th ICFA Advanced Beam Dynamics Workshop (ERL’17), Geneva, Switzerland, June 18-23*. 2017, pp. 4–8.

[18] V. Bechthold. “Investigation of multi-alkali compounds with regard to their suitability for generating highly brilliant electron pulses”. PhD thesis. Johannes Gutenberg University Mainz, 2019.

[19] D. Becker et al. “The P2 experiment”. In: *The European Physical Journal A* 54.11 (2018), pp. 1–61.

[20] I. Ben-Zvi et al. “R&D towards cooling of the RHIC collider”. In: *Nuclear Instruments and Methods in Physics Research Section A: Accelerators, Spectrometers, Detectors and Associated Equipment* 532.1-2 (2004), pp. 177–183.

[21] G. Bir, A. Aronov, and G. Pikus. “Spin relaxation of electrons due to scattering by holes”. In: *Soviet Journal of Experimental and Theoretical Physics* 42 (1976), p. 705.

[22] J. Blakemore. “Semiconducting and other major properties of gallium arsenide”. In: *Journal of Applied Physics* 53.10 (1982), R123–R181.

[23] W. Brattain. *Bardeen J.: Bell System Tech.* 1953.

[24] H. Braun, H. Herminghous, and A. Streun. “The gun/chopper system for the Mainz microtron”. In: *European particle accelerator conference*. 1988.

[25] H. C. Casey and M. B. Panish. *Heterostructure lasers*. Vol. 1. Academic press, 1978.

[26] H. Casey Jr and F. Stern. “Concentration-dependent absorption and spontaneous emission of heavily doped GaAs”. In: *Journal of Applied Physics* 47.2 (1976), pp. 631–643.

[27] N. Chanlek et al. “The degradation of quantum efficiency in negative electron affinity GaAs photocathodes under gas exposure”. In: *Journal of Physics D: Applied Physics* 47.5 (2014), p. 055110.

[28] N. Chanlek. "Quantum efficiency lifetime studies using the photocathode preparation experimental facility developed for the ALICE accelerator". PhD thesis. University of Manchester, 2011.

[29] Coherent. *Operator's manuel: The coherent Mira Optima 900-F laser*. https : / / www . coherent . com. Coherent Inc. 5100 Patrick Henry Drive, Santa Clara, CA 95054, Aug. 2004.

[30] A. collaboration et al. "Precision Electroweak Measurements and Constraints on the Standard Model". In: *arXiv preprint arXiv:0811.4682* (2008).

[31] Crytur. *Technical Parameters Ce:YAG*. https : / / www . crytur . cz / materials/yagce/.

[32] H. Davoudiasl, H.-S. Lee, and W. J. Marciano. ""Dark" Z implications for parity violation, rare meson decays, and Higgs physics". In: *Physical Review D* 85.11 (2012), p. 115019.

[33] H. Davoudiasl, H.-S. Lee, and W. J. Marciano. "Muon g- 2, rare kaon decays, and parity violation from dark bosons". In: *Physical Review D* 89.9 (2014), p. 095006.

[34] M. Dehn et al. "Reducing the contribution of the photoemission process to the unwanted beam in photoelectron sources at accelerators". In: *Applied Physics Letters* 111.13 (2017), p. 132105.

[35] M. Dehn. "Transport processes in photocathodes and their contribution to the longitudinal halo of electron accelerators". PhD thesis. Johannes Gutenberg University Mainz, 2018.

[36] L. Doria et al. "Search for light dark matter with the MESA accelerator". In: *arXiv preprint arXiv:1809.07168* (2018).

[37] H.-J. Drouhin, C. Hermann, and G. Lampel. "Photoemission from activated gallium arsenide. I. Very-high-resolution energy distribution curves". In: *Physical Review B* 31.6 (1985), p. 3859.

[38] H.-J. Drouhin et al. "Spin-dependent transmission of free electrons through ultrathin cobalt layers". In: *Journal of applied physics* 79.8 (1996), pp. 4734–4739.

[39] B. Dunham et al. "Record high-average current from a high-brightness photoinjector". In: *Applied Physics Letters* 102.3 (2013), p. 034105.

[40] A. Einstein. "On a heuristic point of view concerning the generation and transformation of light". In: *annals of physics* 4 (1905).

[41] G. Fishman and G. Lampel. "Spin relaxation of photoelectrons in p-type gallium arsenide". In: *Physical Review B* 16.2 (1977), p. 820.

[42] S. Friederich, K. Aulenbacher, and C. Matejcek. "Vacuum lifetime and surface charge limit investigations concerning high intensity spin-polarized photoinjectors". In: *Journal of Physics: Conference Series*. Vol. 1350. 1. IOP Publishing. 2019, p. 012045.

[43] T. J. Gay and F. Dunning. “Mott electron polarimetry”. In: *Review of scientific instruments* 63.2 (1992), pp. 1635–1651.

[44] T. J. Gay et al. “Extrapolation procedures in Mott electron polarimetry”. In: *Review of scientific instruments* 63.1 (1992), pp. 114–130.

[45] L. Gerchikov et al. “Spin polarized electron transport and partial localization of photoelectrons in highly doped photocathodes”. In: *Journal of Physics: Conference Series*. Vol. 298. 1. IOP Publishing. 2011, p. 012013.

[46] C. Ghosh and B. Varma. “Preparation and study of properties of a few alkali antimonide photocathodes”. In: *Journal of Applied Physics* 49.8 (1978), pp. 4549–4553.

[47] J. Grames et al. “Ion back-bombardment of GaAs photocathodes inside dc high voltage electron guns”. In: *Proceedings of the 2005 Particle Accelerator Conference*. IEEE. 2005, pp. 2875–2877.

[48] S. M. Gruner et al. “Energy recovery linacs as synchrotron radiation sources”. In: *Review of Scientific Instruments* 73.3 (2002), pp. 1402–1406.

[49] J. Haimson. *Optimization criteria for standing wave transverse magnetic deflection cavities*. Tech. rep. Haimson Research Corp., Santa Clara, CA (United States), 1995.

[50] P. Hartmann. *Aufbau einer gepulsten Quelle polarisierter Elektronen*. Shaker, 1998.

[51] P. Hartmann et al. “A diffusion model for picosecond electron bunches from negative electron affinity GaAs photocathodes”. In: *Journal of applied physics* 86.4 (1999), pp. 2245–2249.

[52] W. Herr and B. Muratori. “Concept of luminosity”. In: (2006).

[53] A. Herrera-Gómez, G. Vergara, and W. Spicer. “Physics of high-intensity nanosecond electron source: Charge limit phenomenon in GaAs photocathodes”. In: *Journal of applied physics* 79.9 (1996), pp. 7318–7323.

[54] R. J. Holt and M. A. Miller. “Polarized Gas Targets and Polarized Beams: Seventh International Workshop. Proceedings”. In: (1998).

[55] F. Hug et al. “MESA-an ERL project for particle physics experiments”. In: *Proc. LINAC’16* 28 (2016), pp. 313–315.

[56] H. Iijima et al. “A study of lifetime of NEA-GaAs photocathode at various temperatures”. In: *measurements* 2 (2010), p. 3.

[57] K. L. Jensen. “Electron emission physics”. In: *Advances in Imaging and Electron Physics* 149 (2007), pp. 147–279.

[58] Keithley. *Keithley Model 6485 Picoammeter Instruction Manuel*. http : / / www . keithley . com. Keithley Instruments Inc. 28775 Aurora Road Cleveland, Ohio 44139, 2001.

[59] J. Kessler. *Polarized electrons*. Vol. 1. Springer Science & Business Media, 2013.

[60] E. Kirsch. "Measurements of the pulse response times of gallium arsenide and potassium-Cesium-antimonide". In: *Johannes Gutenberg University Mainz, Diploma Thesis* (2014).

[61] C. Kittel, P. McEuen, and P. McEuen. *Introduction to solid state physics*. Vol. 8. Wiley New York, 1996.

[62] F. Klein, H. Schmieden, et al. "Electromagnetic nucleon form factors in the spacelike region". In: *Nuclear Physics A* 623.1-2 (1997), pp. 323–332.

[63] K. Koike et al. "Spin-polarized scanning electron microscope for analysis of complicated magnetic domain structures". In: *Japanese journal of applied physics* 25.9A (1986), p. L758.

[64] S.-Y. Lee. *Spin dynamics and snakes in synchrotrons*. World Scientific Publishing Company, 1997.

[65] W. Liu et al. "Effects of ion bombardment on bulk GaAs photocathodes with different surface-cleavage planes". In: *Physical Review Accelerators and Beams* 19.10 (2016), p. 103402.

[66] W. Liu et al. "Evaluation of GaAsSb/AlGaAs strained superlattice photocathodes". In: *AIP Advances* 8.7 (2018), p. 075308.

[67] W. Liu et al. "Record-level quantum efficiency from a high polarization strained GaAs/GaAsP superlattice photocathode with distributed Bragg reflector". In: *Applied Physics Letters* 109.25 (2016), p. 252104.

[68] F. Maas et al. "Measurement of Strange-Quark Contributions to the Nucleon's Form Factors at $Q^2 = 0.230(GeV/c)^2$". In: *Physical review letters* 93.2 (2004), p. 022002.

[69] F. Maas et al. "Measurement of the transverse beam spin asymmetry in elastic electron-proton scattering and the inelastic contribution to the imaginary part of the two-photon exchange amplitude". In: *Physical review letters* 94.8 (2005), p. 082001.

[70] Y. Mamaev et al. "Kinetics of highly spin-polarized electron photoemission from an InGaAlAs strained layer by energy and spin-resolved measurements". In: *Journal of applied physics* 93.12 (2003), pp. 9620–9624.

[71] Y. A. Mamaev et al. "Energy resolved spin-polarised electron photoemission from strained GaAs/GaAsP heterostructure". In: *Solid State Communications* 114.7 (2000), pp. 401–405.

[72] T. Maruyama et al. "Observation of strain-enhanced electron-spin polarization in photoemission from InGaAs". In: *Physical review letters* 66.18 (1991), p. 2376.

[73] T. Maruyama et al. “Systematic study of polarized electron emission from strained GaAs/GaAsP superlattice photocathodes”. In: *Applied physics letters* 85.13 (2004), pp. 2640–2642.

[74] C. Matejcek. “Schnelle Helizitätswechsel für das P2-Projekt an MESA”. In: *Johannes Gutenberg-Universität Mainz, Diplom* (2013).

[75] J. Maxson et al. “Fundamental photoemission brightness limit from disorder induced heating”. In: *New Journal of Physics* 15.10 (2013), p. 103024.

[76] F. Meier and B. P. Zakharchenya. *Optical orientation*. Elsevier, 2012.

[77] H. Merkel. “Internal Target Experiments at the MESA accelerator”. In: *54th International Winter Meeting on Nuclear Physics*. 2016, p. 37.

[78] E. J. Montgomery. “Characterization of quantum efficiency and robustness of cesium-based photocathodes”. PhD thesis. 2010.

[79] G. Mulhollan et al. “Photovoltage effects in photoemission from thin GaAs layers”. In: *Physics Letters A* 282.4-5 (2001), pp. 309–318.

[80] C. Nachtigall. “Development of a highly polarized electron beam for MAMI using the photoelectron emission of uniaxially deformed III - V semiconductors”. PhD thesis. Dissertation, Institute for Physics at Johannes Gutenberg University Mainz, 1996.

[81] T. Nakanishi et al. “Highly polarized electrons from superlattice photocathodes”. In: *AIP Conference Proceedings*. Vol. 421. 1. American Institute of Physics. 1998, pp. 300–310.

[82] T. Nakanishi et al. “Large enhancement of spin polarization observed by photoelectrons from a strained GaAs layer”. In: *Physics Letters A* 158.6-7 (1991), pp. 345–349.

[83] R. Nathan and C. Mee. “Photoelectric and Related Properties of the Potassium—Antimony—Caesium Photocathode”. In: *International Journal of Electronics* 23.4 (1967), pp. 349–354.

[84] R. Nathan and C. Mee. “The energy distribution of photoelectrons from the K2CsSb photocathode”. In: *physica status solidi (a)* 2.1 (1970), pp. 67–72.

[85] N. Nishimori et al. “Development of an electron gun for the ERL light source in Japan”. In: *Proc. of the ERL07, to be published* (2007).

[86] D. Orlov et al. “Energy distributions of electrons emitted from GaAs (Cs, O)”. In: *Applied Physics Letters* 78.18 (2001), pp. 2721–2723.

[87] D. A. Orlov et al. “Long term operation of high quantum efficiency GaAs (Cs, O) photocathodes using multiple recleaning by atomic hydrogen”. In: *Journal of Applied Physics* 106.5 (2009), p. 054907.

[88] J. I. Pankove. *Optical processes in semiconductors*. Courier Corporation, 1975.

[89] S. Penner. "Calculations of properties of magnetic deflection systems". In: *Review of Scientific Instruments* 32.2 (1961), pp. 150–160.

[90] Y. Peter and M. Cardona. *Fundamentals of semiconductors: physics and materials properties*. Springer Science & Business Media, 2010.

[91] D. T. Pierce and F. Meier. "Photoemission of spin-polarized electrons from GaAs". In: *Physical Review B* 13.12 (1976), p. 5484.

[92] D. T. Pierce et al. "The GaAs spin polarized electron source". In: *Review of Scientific Instruments* 51.4 (1980), pp. 478–499.

[93] G. Pikus and A. Titkov. "Spin relaxation under optical orientation in semiconductors". In: *Optical Orientation* 8 (1984), pp. 73–131.

[94] M. Prairie and R. Kolbas. "A general derivation of the density of states function for quantum wells and superlattices". In: *Superlattices and microstructures* 7.4 (1990), pp. 269–277.

[95] C. Y. Prescott et al. "Parity non-conservation in inelastic electron scattering". In: *Physics Letters B* 77.3 (1978), pp. 347–352.

[96] *Proceedings, Workshop on Photocathodes for Polarized Electron Sources for Accelerators: September 8-10, 1993*. Apr. 1994.

[97] T. Raubenheimer et al. "Zeroth order design report for the next linear collider". In: *SLAC-Report-474* (1996).

[98] B. Reznikov and A. Subashiev. "Transient processes in photocathodes at high laser intensities". In: *Semiconductors* 32.12 (1998), pp. 1309–1317.

[99] E. J. Riehn. "Phase stabilization of a radio frequency synchronized pulsed electron source". Master's thesis, Johannes Gutenberg University Mainz, 2006.

[100] E. J. Riehn. "Photocathodes with internal DBR reflector as sources of high-intensity spin-polarized electron beams". PhD thesis. Johannes Gutenberg University Mainz, 2011.

[101] P. Saez et al. "Measurement of charge limit in a strained lattice GaAs photocathode". In: *Photodetectors and Power Meters*. Vol. 2022. International Society for Optics and Photonics. 1993, pp. 45–50.

[102] M. Salomaa and H. Enge. "Velocity selector for heavy-ion separation". In: *Nuclear Instruments and Methods* 145.2 (1977), pp. 279–282.

[103] N. Scahill. "Investigating electron optical properties of large aperture quadrupoles for MESA". Master thesis, Institute for Nuclear Physics, Johannes Gutenberg University Mainz, 2015.

[104] J. Scheer and J. Van Laar. "Fermi level stabilization at cesiated semiconductor surfaces". In: *Solid State Communications* 5.4 (1967), pp. 303–306.

[105] J. Scheer and J. Van Laar. "GaAs-Cs: A new type of photoemitter". In: *Solid State Communications* 3.8 (1965), pp. 189–193.

[106] B. Schlimme et al. “Operation and characterization of a windowless gas jet target in high-intensity electron beams”. In: *arXiv preprint arXiv:2104.13503* (2021).

[107] J. Schuler. “Ultrafast spectroscopy in photoemission from III-V semiconductors”. PhD thesis. Dissertation, Institute for Nuclear Physics, Johannes Gutenberg University Mainz, 2004.

[108] J. Schuler. “Optimierung der Strahlführung der Quelle polarisierter Elektronen an MAMI.” Diploma thesis, Institute for Nuclear Physics, Johannes Gutenberg University Mainz, 1997.

[109] V. Shvedunov et al. “Design of a prebuncher for increased longitudinal capture efficiency of MAMI”. In: *Proc. EPAC96, Barcelona* (1996), p. 1556.

[110] C. K. Sinclair. “Electron beam polarimetry”. In: *AIP Conference Proceedings CONF-980573*. Vol. 451. 1. American Institute of Physics. 1998, pp. 23–39.

[111] C. Sinclair et al. “Development of a high average current polarized electron source with long cathode operational lifetime”. In: *Physical Review Special Topics-Accelerators and Beams* 10.2 (2007), p. 023501.

[112] J. Singh. *Electronic and optoelectronic properties of semiconductor structures*. Cambridge University Press, 2007.

[113] W. Spicer. “Negative affinity 3–5 photocathodes: Their physics and technology”. In: *Applied physics* 12.2 (1977), pp. 115–130.

[114] W. E. Spicer and A. Herrera-Gomez. “Modern theory and applications of photocathodes”. In: *Photodetectors and Power Meters*. Vol. 2022. International Society for Optics and Photonics. 1993, pp. 18–35.

[115] W. E. Spicer. “Photoemissive, photoconductive, and optical absorption studies of alkali-antimony compounds”. In: *Physical review* 112.1 (1958), p. 114.

[116] K.-H. Steffens et al. “A Spin rotator for producing a longitudinally polarized electron beam with MAMI”. In: *Nuclear Instruments and Methods in Physics Research Section A: Accelerators, Spectrometers, Detectors and Associated Equipment* 325.3 (1993), pp. 378–383.

[117] K.-H. Steffens. “Design and optimization of a 100 keV injection system for generating a longitudinally polarized electron beam at MAMI”. PhD thesis. 1993.

[118] B. Steiner et al. “Wien filter as a spin rotator at low energy”. In: *2007 IEEE Particle Accelerator Conference (PAC)*. IEEE. 2007, pp. 170–172.

[119] A. Subashiev et al. “Spin-polarized electrons: generation and applications”. In: *Physics of Low-Dimensional Structures (PLDS)* 1999.1-2 (1999), pp. 1–36.

[120] K. Sueoka et al. “Mott Spin Polarimeter with Spherical Acceleration Electrodes”. In: *Memoirs of the Faculty of Engineering, Hokkaido University* 19.1 (1994), pp. 1–8.

[121] S. M. Sze, Y. Li, and K. K. Ng. *Physics of semiconductor devices*. John wiley & sons, 2021, pp. 17–20.

[122] H. Tang et al. "Study of nonlinear photoemission effects in III-V semiconductors". In: *Proceedings of International Conference on Particle Accelerators*. IEEE. 1993, pp. 3036–3038.

[123] H. Tang et al. "Experimental studies of the charge limit phenomenon in NEA GaAs photocathodes". In: *Conf. Proc. C* 940627 (1994), pp. 46–48.

[124] H. Tang et al. *Experimental studies of the charge limit phenomenon in GaAs photocathodes*. Tech. rep. Stanford Linear Accelerator Center, Menlo Park, CA (United States), 1993.

[125] F. Technology. http : / / www . lasermatrics . com, http :/ / www . fastpulse . co. FastPulse Technology Inc. 220 Midland Avenue Saddle Brook, NJ 07663.

[126] L. H. Thomas. "I. The kinematics of an electron with an axis". In: *The London, Edinburgh, and Dublin Philosophical Magazine and Journal of Science* 3.13 (1927), pp. 1–22.

[127] M. Thompson. *Noise intuitive analog circuit design*. 2014.

[128] V. Tioukine and K. Aulenbacher. "Operation of the MAMI accelerator with a Wien filter based spin rotation system". In: *Nuclear Instruments and Methods in Physics Research Section A: Accelerators, Spectrometers, Detectors and Associated Equipment* 568.2 (2006), pp. 537–542.

[129] V. Tioukine et al. "Spin Manipulation at MAMI C". In: *EPAC*. Vol. 2. Citeseer. 2002, p. 1816.

[130] K. Togawa et al. "Surface charge limit in NEA superlattice photocathodes of polarized electron source". In: *Nuclear Instruments and Methods in Physics Research Section A: Accelerators, Spectrometers, Detectors and Associated Equipment* 414.2-3 (1998), pp. 431–445.

[131] M. Uhrig et al. "Calibration of a Mott detector using circularly polarized impact radiation from helium". In: *Review of scientific instruments* 60.5 (1989), pp. 872–878.

[132] U. Weigel. "Cold intense electron beams from gallium arsenide photocathodes". PhD thesis. 2003.

[133] T. Weilbach. "Minimally invasive beam diagnosis for high-intensity electron beams". PhD thesis. Johannes Gutenberg University Mainz, 2019.

[134] M. Weis. "Analysis and improvement of the time resolution of the test source of polarized electrons at MAMI". Diploma thesis, Institute for Nuclear Physics, Johannes Gutenberg University Mainz, 2004.

[135] R. K. Willardson and A. C. Beer. *Semiconductors and semimetals*. Academic press, 1977.

[136] K. Wille. *The physics of particle accelerators: an introduction*. Clarendon Press, 2000.

[137] M. Woods et al. "Observation of a charge limit for semiconductor photocathodes". In: *Journal of applied physics* 73.12 (1993), pp. 8531–8535.

[138] N. Yamamoto et al. "Thermal emittance measurements for electron beams produced from bulk and superlattice negative electron affinity photocathodes". In: *Journal of Applied Physics* 102.2 (2007), p. 024904.

[139] K. Zerrouati et al. "Spin-lattice relaxation in p-type gallium arsenide single crystals". In: *Physical Review B* 37.3 (1988), p. 1334.

[140] S. Zhang, S. Benson, and C. H-Garcia. "Observation and measurement of temperature rise and distribution on GaAs photo-cathode wafer with a 532 nm drive laser and a thermal imaging camera". In: *Nuclear Instruments and Methods in Physics Research Section A: Accelerators, Spectrometers, Detectors and Associated Equipment* 631.1 (2011), pp. 22–25.